PHYSIK-DEPARTMENT

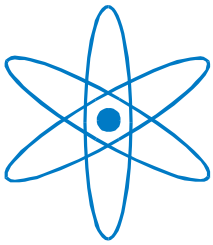

INVESTIGATIVE METHODS ADAPTED TO ASSESS THE BIOLOGICAL PROPERTIES OF LASER-DRIVEN PROTONS

Dissertation
von

NICOLE HUMBLE

– October 2013 –

TECHNISCHE UNIVERSITÄT
MÜNCHEN

TECHNISCHE UNIVERSITÄT MÜNCHEN

Advanced Technologies in Radiation Therapy

INVESTIGATIVE METHODS ADAPTED TO ASSESS THE BIOLOGICAL PROPERTIES OF LASER-DRIVEN PROTONS

Nicole Humble

Vollständiger Abdruck der von der Fakultät für Physik der Technischen Universität München zur Erlangung des akademischen Grades eines

Doktors der Naturwissenschaften (Dr. rer. nat.)

genehmigten Dissertation.

Vorsitzender:	Univ. Prof. Dr. Martin Zacharias
Prüfer der Dissertation:	1. Univ. Prof. Dr. Jan J. Wilkens
	2. Univ. Prof. Dr. Franz Pfeiffer

Die Dissertation wurde am ..... 15.10.2013 ..... bei der Technischen Universität München eingereicht und durch die Fakulät für Physik am ..... 07.01.2014 ..... angenommen.

ABSTRACT

Laser-driven technology utilising high-intensity table top lasers offers the promise of a more affordable and compact source of protons for radiotherapy. Due to the pulsed nature of the laser, laser-driven protons will be delivered in nanosecond bunches. Therefore, prior to clinical implementation, the biological properties of laser-driven protons must be investigated to determine whether such protons differ biologically to those produced by established acceleration means.

This was investigated via cell irradiations with human tumour (HeLa) cells. Experiments using the ATLAS laser at the Max Planck Institute of Quantum Optics currently show the protons to be accelerated out of the rear target foil in a process called Target Normal Sheath Acceleration (TNSA). This results in an exponential energy distribution with a maximum at 7 MeV and is far below the therapeutic requirements of 250 MeV for deep-seated tumours. Such a low energy therefore presents an upper limit in penetrable depth. Since a broad energy distribution results in the loss of a clean Bragg peak, which is responsible for the precise dose localisation typically achieved in conventional proton radiotherapy, the experiment presented here, utilises mini-quadrupole magnets to create a quasi-monoenergetic spectrum centred on 5.2 ± 0.15 MeV where 50% of the protons is contained within this energy band. Under these conditions, a line focus is created 6 mm long and 0.5 mm wide to produce an inhomogeneous dose distribution. Utilising this feature, a complete biological dose response can be gathered within a single shot of the laser, delivered over the order of nanoseconds; this being several orders of magnitude less than for conventionally produced protons.

This thesis presents methods adapted to assess the biological properties of laser-driven pulsed protons with cell experiments and compares these directly to continuous protons. Biologically, this was conducted with an automated γH2AX analysis in 3D and applied to individual cells so that processing time is over the order of hours rather than days as in manual assessment. The parameters necessary for automation are a minimum volume and range of pixel intensities in the focal spots representing cellular damage. These parameters are deduced objectively from the characteristics of the images themselves thereby eliminating subjectivity associated with manual counting. Concerning the dosimetry, radiochromic EBT2 film was employed utilising a proton low energy (3 MeV) dose calibration measured here. This was necessary due to the LET dependence EBT2 is known to exhibit and is compared to a higher energy calibration (11 MeV) where no LET dependence exists. Since the film was found to under-respond by 26% at low energies, doses were necessarily corrected for using the newly established calibration curve. Dose is localised on the cellular scale via several registrations and coordinate system transformations to recover high precision spatial dose information. In order to deliver pulses on an even shorter time scale, simulations have been performed to determine the setup requirements for a picosecond cell irradiation. Since the pulse duration comes primarily from the broad energy spectrum, some different setups are presented which aim to reduce the pulse length, which is limited by this broad energy spectrum whilst maintaining a dose adequate for cell irradiation and dose detection.

CONTENTS

LIST OF FIGURES

LIST OF TABLES

ACRONYMS

API Application Programming Interface

BGR Box to Grid Registration

CE Coulomb Explosion

CPA Chirped Pulse Amplification

CRT Cell to Reference coordinate system Transformation

CSDA Continuous Slowing Down Approximation

DLC Diamond Like Carbon

DLLPA Direct Laser-Light Pressure Acceleration

DNA Deoxyribonucleic Acid

DSB Double Strand Break

EBRT External Beam Radiotherapy

FOV Field of View

GFR Grid to Film Registration

GFP Green Fluorescent Protein

GUI Graphical User Interface

HTA High Throughput Analysis

IMRT Intensity Modulated Radiation Therapy

LET Linear Energy Transfer

MGR Mark to Grid Registration

MVA Magnetic Vortex Acceleration

NA Numerical Aperture

PIC Particle In Cell

PSF Point Spread Function

RBE Relative Biological Efficiency

RGT Reference coordinate system to Grid Transformation

ROI Region of Interest

RPA Radiation Pressure Acceleration

SNAKE Supraleitendes Nanoskop für Angewandte Kernphysikalische Experimente/superconducting nanoprobe for applied nuclear physics experiments

SOBP Spread Out Bragg Peak

SSB Single Strand Break

TNSA Target Normal Sheath Acceleration

VMAT Volumetric Arc Therapy

Part I

INTRODUCTION

1 RATIONALE

The global burden of cancer is set to increase even beyond the figures we experience today, which, according to the current World Health Organisation (WHO) estimates, means the mortality of cancer will increase by 45% from 2007 to 2030 [80]. Therefore the search for successful types of treatment is of increasing interest. Although cancer may be successfully treated with a range of therapies with the mainstays including surgery, chemotherapy, radiotherapy and more recently targeted therapies, they are rarely used on their own (e. g. types of leukaemia are successfully treated through chemotherapy alone [85]) since studies show a combination of modalities indicates the best outcome [83]. Though to what extent each therapy should be involved, depending on the cancer type varies across institutions. Guidelines regarding the optimal radiotherapy use for cancer treatment ranges from 20-50% of the total treatment depending on the country [32]. To further complicate matters, an 'optimal' radiation type remains clinically debated and again differs according to cancer type as well as patient case. The main radiation modalities in use at present use photons and protons whereby traditional paradigms for radiation-induced cell damage cite tumour cell kill as the result of irreparable damage to the DNA[1]. Furthermore, electrons are often also prescribed though generally as a boost treatment e. g. breast cancer or for superficial tumours. Other notable mentions include neutron therapy and carbon therapy though are far less common; the discussion here will be limited to photon and proton therapy.

Several drawbacks concerning proton therapy exist and are still up for discussion today: on the practical side, the costs and size of the devices associated with accelerating protons to high enough energies for treatment are so much greater than photons that their use in the clinic is but a fraction of what it perhaps should be; on the clinical side the accuracy in treatment delivery becomes much more critical especially for moving targets. Since the benefits of protons are still severely hindered by the immense costs [33], there have been and are a number of clinical trials attempting to prove their efficacy for a given tumour type. Whether the efficacy of protons can or should be clinically proven is not discussed here [121][45], rather this thesis addresses the former of these two sides of the drawbacks associated with proton therapy, i. e. the size and costs, by examining an alternative proton source, which may serve to improve proton therapy efficacy in the future.

This introductory section develops an argument concerning the use of protons in cancer therapy and the interest involved in seeking alternative proton sources. As such it should highlight the stark contrasts between our current understanding and experience with protons and those produced by high intensity lasers so that it becomes clear to the reader that we first need to ascertain the characteristics of such protons via novel methods that exist outside of traditional approaches before the end goal of treatment can be reached. Implementation regarding the therapeutic side of protons such as beam delivery techniques or treatment planning as well as the fundamentals of radiotherapy will not be discussed here, instead the unfamiliar reader is referred to texts [96][48] respectively for an understanding of these concepts. Furthermore, only a very brief introduction to the relevant physical and biological concepts will be presented here; for a detailed account of radiological physics and dosimetry the reader

1 In recent times this paradigm is being challenged by the bystander effect (amongst others) as playing an important role in cell kill.

may also consult [8]. This introductory part presented here is to get the reader acquainted with the general feel for the topic of the thesis, however since the thesis is comprised of parts which are mostly independent from each other, a more detailed introduction will be provided of the particulars for each part.

1.1 THE CONCEPT OF RADIOTHERAPY

Radiotherapy utilises ionising radiation to control malignant disease. Its origins arose shortly after Wilhelm Röntgen discovered xrays in 1895 in the form of Röntgenology, the earliest form of External Beam Radiotherapy (EBRT) and following the breakthrough developments made by Bequerel, Pierre Curie and Marie Curie with radium (an early form of brachytherapy[2]) it was noted that although both produced the desired damage required for therapy, slightly different side effects could be observed, which concluded in radium being generally preferred because it could be applied locally and thus was more specific in damage than Röntgenotherapy [19]. Since then, EBRT has dramatically changed and is now applied with linear accelerators and sophisticated beam shaping techniques in the forms of conformal radiation therapy, Intensity Modulated Radiation Therapy (IMRT) and Volumetric Arc Therapy (VMAT). However the general principle remains the same as previously noted in 1935: certain radiation treatments might be preferred over others due to localisation of damage. This concept is illustrated in the Figure 1 where the therapeutic gain depends on our ability to maximise damage to the tumour and minimise damage to the surrounding normal tissue.

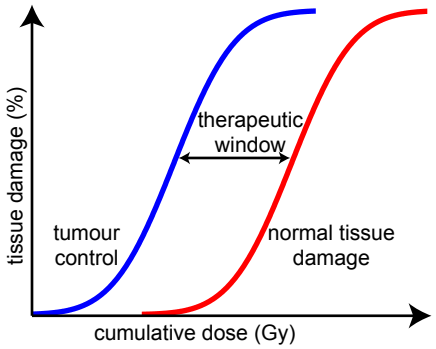

Figure 1: The trade-off between tumour and normal tissue damage.

1.2 A COMPARISON OF PHOTON AND PROTON THERAPY

Shortly after some significant conceptual advances in radiation therapy (such as fractionation), protons were proposed by Wilson in 1946 [136], whose physical properties make them a favourable therapeutic choice. These properties refer specifically to the finite range arising from a culmination of interactions between the incoming protons and the irradiated material. These interactions can be grouped according to stopping, scattering (elastic scattering off the nucleus also known as multiple Coulomb scattering and well approximated by the Highland formula) and nuclear interactions the latter of which being to a lesser degree (~20% for 120 MeV protons).

2 Brachytherapy (short distance) is also a mainstay of radiation therapy especially for urogenital cancers, but EBRT is used in general more often because it can be fractionated and shaped with more precision.

We focus the discussion now on stopping i. e. energy loss, since it is the most relevant parameter in the context of this thesis. Protons being charged particles are a direct form of ionising radiation since most of their energy is lost through a large number of Coulomb-force interactions in soft and hard collisions with outer electrons depending upon the length of impact parameter to the atomic radius. This means that the energy transfer per interaction is relatively small and so charged particles undergo a large number of interactions when passing through matter with an estimated range in a homogeneous material given by the Continuous Slowing Down Approximation (CSDA) [g/cm^2]. These mechanisms result in a large energy deposition at the end of the range because a greater amount of energy is transferred as the particle slows down, before eventually stopping. Here S, the stopping power is introduced, which describes the mean rate of energy loss per unit path, well approximated by the Bethe-Bloch equation with units [J/cm] or [MeV/cm]. Now the rapid energy loss at the end of the range can be understood by considering the $1/\beta^2$ dependence where $\beta = v/c$. The total stopping power is the sum of the collisional stopping power and the radiative stopping power. Since S is dependent upon the properties of the material with which the particle interacts, it is much more common to use the *mass* stopping power, by dividing by the density ρ:

$$\frac{S(E)}{\rho} = \frac{1}{\rho} \cdot \frac{dE}{dx}, \tag{1}$$

where the units here are usually given as [$MeVcm^2/g$]. A related concept, is the Linear Energy Transfer (LET), which has the same units as S and can be defined a number of ways [133]. Throughout this thesis, the definition of $LET =< S >$ is used. Broadly speaking, protons and photons are said to be low LET radiations whereas alpha particles and heavy ions are considered high LET.

In contrast, charge-neutral photons are indirectly ionising meaning that ionisation is a two-step process whereby photons first lose the majority of their energy to atomic electrons, (as energetic beta particles) which in turn go on to produce further ionisations via numerous Coulomb-force interactions as with directly ionising radiation. The initial interactions between photons and matter are, in comparison to charged particles, relatively few and occur via the photoelectric effect, Compton effect and pair production with each effect dominating over low, intermediate and high energy ranges respectively[3]. As such, the number of primary interactions between photon and electron are few and more critical in energy loss. Thus the total energy loss is dependent upon the relative energy loss contributions designated by the mass-energy absorption coefficient μ_{en}/ρ [cm^2/g]. Analogous equations can also be derived for photon energy loss in matter as well as dose, however, since they are not relevant to this thesis, are not detailed here. A thorough description is provided in [8].

A vital quantity to radiotherapy is dose D, given by the mean energy per mass deposited over a given volume. Quantitatively for protons this is given by the product of S with the fluence, $\phi = \frac{dN}{dA}$ [p/cm^2] so that for a given volume:

$$D = \int_0^{E_{max}} \frac{d\phi(E)}{dE} \frac{S(E)}{\rho} dE, \tag{2}$$

where units are given in [J/kg], also known as Gray [Gy]. Since particles will lose their energy via collisions at a rate inversely proportional to their velocity, as the particles slow down, larger

3 Photoeffect is also very dependent on the atomic number, Z of the material and has important implications for diagnostic purposes.

amounts of energy are deposited at the end of the range thus giving rise to the well-known Bragg peak in the depth dose curve. Whereas photons will exponentially decay in intensity with depth and since the range of the secondary charged particles is finite, this will result in a small build-up region in the depth dose curve to reach a maximum that gradually tapers off. In IMRT, a typical energy spectrum has a maximum of 6 MeV so that the predominant mode of interaction is via the Compton effect. Consequently a strong argument for charged particle use in radiotherapy can be found when comparing the respective depth dose curves to that of photons. Though many other features and flaws associated with proton therapy can be discussed here, this is the predominant argument cited when discussing the potential of protons in the clinic, which can be demonstrated in practice by comparing dose distribution such as the one in Figure 2. These results are particularly relevant to childhood cancers where the importance of reducing dose in order to minimise secondary cancer risk or even damage to growth plates due to the primary treatment is especially critical.

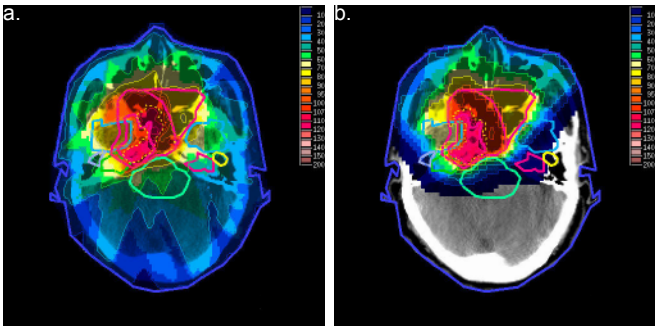

Figure 2: Comparison of an IMRT plan (a) with a proton plan (b) taken directly from [122] shows the high dose conformality so that normal tissue (especially important structures such as the brain stem) irradiation can be minimised.

Until now only the physical properties of protons have been considered, however in therapy it is critical to understand the biological effects associated with the ensuing damage. Ionising radiation produces damage either through direct or indirect *action of* ionising radiation. If we consider the main target to be the Deoxyribonucleic Acid (DNA), then direct action is said to occur when radiation ionises an atom so that the electron will produce damage to the DNA. Whereas for indirect action the electron from the ionised atom first interacts with something other than the DNA such as water (since our bodies are comprised mainly of water), to produce free radicals as a result of water radiolysis. These highly reactive free radicals are then the largest contributors to DNA damage rather than the ionised electron from the initial reaction [54]. Damage to the DNA takes many forms but here we are mostly concerned with Single Strand Breaks (SSBs) and Double Strand Breaks (DSBs), which refer to breaks in the backbone of the DNA. SSBs are said to be sublethal damage and can easily be repaired whereas repair of DSBs can be more error-prone and so is most relevant when considering cell death.

Radiations interacting primarily through direct damage are considered to be high LET, whereas primarily indirect damaging ionising radiations including xrays and protons, are low LET. Direct damage is the more critical of the two types and often yields a more potent biological effect that is therefore not especially dependent upon oxygen levels, which are said to be involved in damage fixation and thus critical in treating hypoxic tumours. The time scale over which all this damage occurs varies according to each process which can be divided into the components of: ionisation (10^{-15} s), free radical lifetime ($10^{-9} - 10^{-10}$ s), DNA damage (10^{-6} s) and finally a detectable biological effect (hours-years). This time scale of DNA damage

may or may not hold relevance in the context of laser-driven protons, which can be produced in pulses of 10^{-12} s.

Finally, we need a means of objectively quantifying the biological potency. In radiotherapy this is commonly measured using the Relative Biological Efficiency (RBE) where, for a given biological endpoint such as (37%) cell kill, the dose is determined for two different radiation types, one of which being the reference radiation, D_{ref}, such as photons and the other is that which we are testing, D_{test}.

$$RBE = \frac{D_{ref}}{D_{test}}\bigg|_{effect} \tag{3}$$

For clinically relevant protons (250 MeV) this is generally acceded to be 1.1.

What the above concepts translate into clinically is that protons are argued to provide a superior dose delivery to the primary target so that normal tissues can be spared. They are of comparable biological effectiveness and much hype has surrounded protons in recent years concerning their application to cancer therapy. Since photons have a more gradual dose gradient, they often have a less conformal dose distribution[4] or at least one which is more difficult to obtain. The corollary is they are perhaps more suitable to a number of (moving) targets precisely because of this gradual dose fall off since poor placement of the Bragg peak can be critical as for example, in the heart. A final caveat to the use of protons in the clinic should be compared directly with their means of acceleration, since photons are well supplied with linear accelerators and sophisticated, well-established beam shaping techniques, with which protons may not be able to compete. Therefore their acceleration is discussed below.

1.3 CURRENT PROTON ACCELERATORS

Traditionally, sources of protons for therapy have been derived from cyclotrons [93] or synchrotrons [51]. Cyclotrons in general tend to be smaller in size (~4 m diameter and ~2 m height) and operate based on the principle of electrostatic gains in energy sandwiched between two magnetic fields (the Dees), which allow the protons to make multiple trips across the electric gradient with an expanding radius. The final energy of the particles is thus predefined by the size of the machine. In this way, protons can be produced with a predefined energy continuous in time (Continuous wave, CW) with energy spread <1% [90]. Synchrotrons on the other hand produce pulsed particle beams and are capable of accelerating particles to even higher energies as at CERN and are larger in size (~6-10 m in diameter). The principle mechanism of operation is based on accelerating already pre-accelerated protons from a device such as a linear accelerator, around a ring with a series of bending and focusing magnets after which they are slowly extracted. The energy spread is several orders of magnitude less than those of cyclotrons.

Though not in general clinical use, but still capable of proton acceleration are tandem accelerators. These are based on a source seeding the accelerator system comprised of two electrostatic chambers in opposing polarities so that the extraction energy will be twice the voltage applied between the poles. Since the accelerator is linear, the particles are unable to make repeats of their path and so the final energy is limited dependent upon the ion type. For the accelerator used in Part IV, this is gained via two sets of 14 MV potential differences to give a maximum proton energy of 26 MeV, with the stable range being ~2-24 MeV. This energy is

4 Although IMRT and VMAT plans are also capable of producing high quality plans with adequate tissue sparing however this topic will not discussed here.

obviously well below the requirements for radiotherapy of deep seated tumours[5], however for a cell irradiation in a single layer this is not an issue.

Needless to say, these treatment devices are of such size, that the capital costs of construction have been estimated to be 2.4 times higher than IMRT [46]. Thus despite the physical dose conformality discussed previously, in order for protons to be a competitive treatment modality, significant advances need to be made on the technological side. These types of developments include the Dielectric Wall accelerator, linear accelerators, compact cyclotron systems, the synchrocyclotron, and what will be discussed in the following section, high intensity lasers. For further details on these emerging technologies readers can consult [112].

1.4 THE NEED FOR PRECLINICAL STUDIES

As a final comment before launching into a description of laser-driven proton acceleration, it is worthwhile summing up the discussion presented here with regards to the aims of this thesis and the motivations behind it. Firstly, that protons are desirable in radiotherapy because of their physical properties, which in principle should be able to deliver a superior treatment (for specific cancer types) because of the reduction in side effects due to sparing normal tissue (see Figure 2). Secondly, the biological evaluation of current therapeutic protons in the form of RBE is comparable to photons and so produces expected biological effects developed within the scope of photon therapy. And thirdly, that despite the aforementioned points, owing to the immense construction costs, proton use in the clinic is still very much limited to a handful of centres around the world with the majority located in the US. If we assume that protons are as efficient as claimed, then we must look at reducing these costs, where one such proposed method is with high intensity lasers. But as with all therapies be it radiotherapy or even a new drug for another disease, treatments are tested first *in vitro* (i. e. in cell culture), followed by *in vivo* tests (i. e. mice studies[6]) before testing on humans.

As many experimentalists will acknowledge, beam time is precious and not always so easy to come by. Thus in the lead up to the cell experiment outlined in Part 3, a number of experiments were previously conducted with nanosecond bunch protons produced by a tandem accelerator. These were tested for a number of biological endpoints *in vitro* [146][115][114] as well as *in vivo* [49][147] based on the premise that a temporal effect is relevant when considering the biological damage however results showed no significantly different RBE.

However these artificially bunched protons are not the same as the bunched protons produced from the laser. Thus while these experiments are useful in comparing temporal effects, they do not exactly mimic the spatial clustering associated with laser-driven protons and one needs to nevertheless test the actual laser-driven proton system as outlined here. Therefore at present we are very much still in the initial stages of testing laser-driven protons since this thesis primarily deals with the *in vitro* stage, to explore whether the biological effect of laser-driven protons is the same as for conventionally produced protons.

5 Since range scales approximately with energy squared, 250 MeV is a typical requirement for radiotherapy, however eye treatments can be used with energies as low as 60 MeV.

6 Mice are most often used in radiotherapy research for cost reasons however other animals such as rabbits, pigs and dogs are also known to be used.

2

LASER-ACCELERATED PROTON PRODUCTION

Since the advent of laser-wakefield acceleration first proposed in 1979 [123] and the development of Chirped Pulse Amplification (CPA) [120], a series of rapid advancements in the field of laser-driven proton technologies has meant the availability of high intensity table top lasers to function as a compact and potentially cheaper source of protons for radiotherapy. The standalone topics of high intensity laser generation and laser-ion acceleration regimes are growing fields with exciting developments. For a very general background so as to understand the characteristics of the resulting protons, a brief account is related in this section; for a better understanding readers may also consult [55].

2.1 HIGH-INTENSITY LASER GENERATION

The success in achieving high intensity laser pulses critical to proton acceleration relies upon generating adequately short laser pulses, which are amplified at a later stage. In the initial years of laser development, this was achieved first with nanosecond pulses followed by a picosecond-femtosecond pulse range, however, such short pulses produced strong non-linear effects because of the resulting high intensity. As a result this time is associated with a plateau in laser intensity gain as a function of time as seen in Figure 3a; it was not until CPA was developed and refined that laser intensities increased once again. The essential problem lies in maintaining a high enough fluence for the necessary output intensity without having this intensity damaging the amplifiers and optical components due to non-linearities in the process. The CPA process achieves this by stretching the pulse in time (i. e. chirped) so that fluence is maintained whilst intensity is reduced to a low enough level that small optics may be used throughout the amplification system. All that remains is to recompress the pulse to its initial state [55].

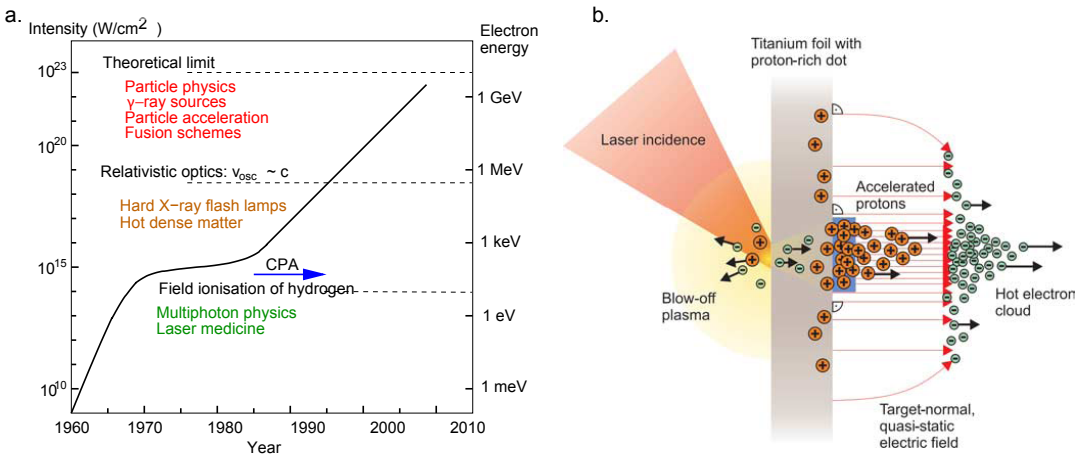

Figure 3: a. The development of the laser taken from [44]. At present, maximum intensities are ~10^{22} W/cm^2. **b.** Schematic of TNSA process where protons are accelerated out of the rear foil of the target.

A comprehensive review of relativistic optics can be found in [84], from which much of the information here was taken.

2.2 ION ACCELERATION SCHEMES

The basic acceleration mechanisms include (Target Normal Sheath Acceleration (TNSA)), Coulomb Explosion (CE), (Radiation Pressure Acceleration (RPA)), Magnetic Vortex Acceleration (MVA) [23] and most recently the so-called Direct Laser-Light Pressure Acceleration (DLLPA) [70], which holds the world record in highest produced proton energy [42]. The two most discussed regimes are briefly considered below.

TNSA is the most studied mechanism and therefore best understood, especially since most experiments have been conducted in this regime. It is characterised by a laser intensity $10^{18} < I_0 < 10^{20}$ W/cm^2 with ultra short pulse duration (fs) resulting in a maximum proton energy, $E \propto \sqrt{I_0}$ and spectrum following a broad exponential distribution. Since the laser itself is delivered over ultra short pulses, the resulting protons will also be pulsed, with durations strongly dependent upon the energy width of the spectrum and the distance between detection and source. Protons are produced when the laser strikes the target, and due to expansion of the electron cloud generated in the plasma, protons are accelerated normal to the target rear wall as shown in Figure 3b. The accelerated protons are either due to introduced target impurities or the ever present contaminants on the target. The process of converting laser energy to proton energy is relatively inefficient (only a few percent [41]) and depends on many factors including laser energy, focus size, pulse duration and target thickness to name a few [22]. The influence of target thickness has special implications for the experiment described in this thesis (see Part III, Chapter 1) since we assume that we are in an *enhanced* TNSA regime [56] through the use of a nanometre thick target as opposed to the originally proposed micrometre thick targets [134]. Other target properties such as impurity concentration, nanostructures on the rear target wall or the use of gas targets (to access the MVA regime) have important implications on the resulting energy spectrum. This holds special relevance in a clinical context because it complicates the treatment planning process, especially when considering the loss of a clean Bragg peak and consequential variations in dose. Since treatment nevertheless often requires a Spread Out Bragg Peak (SOBP) for adequate tumour coverage, this characteristic of TNSA may be exploited as a feature [111].

RPA (also known as the 'laser-piston', 'light sail' or relativistic regime) [38] on the other hand was proposed for very high intensity lasers $I_0 > 10^{21}$ W/cm^2 when combined with a sufficiently thin foil such that the efficiency has been found to be up to 8% [118]. Other features of this regime include a narrower energy distribution (5%) and a higher maximum particle energy (theoretically unlimited) [24] and short pulse proton duration (ps). Up until recently, most results and theories concerning the RPA regime came from Particle In Cell (PIC) simulations however a recent publication [68] claims to have produced results in this regime owing to the superior properties of the ensuing particles. In general however, up to this point our access to this regime is limited by technological advances, specifically relating to the laser intensity and energy.

3 THESIS STRUCTURE

Through the previously developed argument it should be apparent to the reader that due to fundamental differences in the way protons are produced here (via high intensity lasers) and normal approaches (cyclotrons/synchrotrons), we firstly cannot be sure what to expect biologically, specifically the RBE of the protons due to proton bunching. Secondly due to the inhomogeneous dose distribution as a result of the messy acceleration mechanisms (TNSA), higher demands in precision were made on our experiments so that new methods of analysis needed to be developed. Thus the proceeding parts will outline novel methods tailored specifically to the requirements for the biological analysis of laser-driven protons.

Part II develops a key method used throughout this thesis to objectively analyse DSB repair proteins namely γH2AX and 53BP1 foci, which are a proportional measure of the radiation dose and thus radiation quality. Included in this section is a table of current literature, reviewing methods that have been developed so far. Since the final method developed here is used in Parts III, IV and possibly the experiment corresponding to Part V, an entire part has been devoted to this method. Furthermore this section serves as a reference for the methods that were attempted but yielded unsatisfactory results, which may be useful to future developments in the field of automated foci counting.

Part III presents the methods and results from a cell experiment with laser-driven protons delivered in a single shot. This especially refers to the recovery of the spatial dose information via image registration. Moreover, a comparison is made between the method established in Part II and the technique published in [16]. Here, however, the main goal was to judge the biological efficiency of protons (RBE) produced by high intensity lasers with a low energy and ns pulse duration.

Part IV is a direct comparison between low energy protons produced from a tandem accelerator to the laser-driven protons protons discussed in Part III. We call these tandem accelerator protons continuous ($\Delta t = 10^{-3}$ s) whereas those from the laser are pulsed ($\Delta t = 10^{-9}$ s); this terminology will be used throughout this thesis. Therefore, the duration of exposure is some orders of magnitude greater than the protons produced from the laser and so it is questionable whether these two radiations correlate to the same effect. This section also contains an explicitly measured low energy dependence of the radiochromic film used in Part III, whose calibration at the appropriate energy, we did not yet have. The key findings have been published in [100].

Part V is a Monte Carlo simulation for an experiment that is designed specifically to optimise our chances of observing an enhanced biological effect with a ps proton bunch. Since the pulse duration of laser-driven protons may further be reduced when detected not far from the source, the expected spatial and temporal clustering is hypothesized to have an enhanced biological effect. Though the results of Part III indicate otherwise, the possibility remains that the spatial and temporal conditions still did not met the requirements necessary to see a difference in RBE. Thus this section investigates the setup requirements concerning the temporal aspect from the laser-driven proton spectrum for an ultra-pulsed proton bunch delivered to cells.

Finally the last part summarises and links together the ideas and key findings of the methods developed here and the future prospects for laser-driven protons.

Part II

DEVELOPING A ROBUST METHOD OF AUTOMATED FOCI COUNTING

1

PRINCIPLES OF FLUORESCENCE MICROSCOPY

As mentioned in the introduction, this section presents a systematic investigation of methods that can be used to objectively determine the number of DSBs per cell. Here, the γH2AX Assay is used as a measure of radiation-induced DSBs. The assay is based upon the H2AX mammalian histone variant, a basic subunit of chromatin, which upon DSB induction, is phosphorylated on the amino acid Serine-139 into γH2AX [106]. Since antibodies are specific, they can be raised against a certain process such as for the phosphorylation of H2AX to γH2AX. Large amounts of γH2AX concentrate at the site of the DSB i. e. a focus, so that by coupling a fluorescent marker to the specific antibody, DSBs can be observed. Since many proteins are recruited to the site of the break, other antibodies can also be labelled with a different coloured fluorescent marker to be imaged under the microscope. Therefore it is common to not only image the γH2AX but other repair proteins such as 53BP1 [78]. A more detailed overview concerning the assay and its use in a cancer context can be found in [21].

For the cell line used and the radiation quality expected, there should be a one to one ratio of focus induction per DSB. A general rule of thumb is given as 23 foci per Gy per cell[1]. To scale the problem in an actual experiment, we have approximately 23 foci/Gy cell, and at least 100 cells per dose point (provided the dose levels are discrete from 0-2 Gy at 0.5 Gy intervals). This number is then doubled because two repair proteins are detected so that there are two channels of foci to count, thereby bringing the total number of cells to be assessed to 1000. Such a number demonstrates the interest in automating the process of foci counting as much as possible.

The technicalities concerning the assay will not be discussed here, rather this section is concerned with the automated analysis of foci induction, which appear as bright spots in the irradiated cell. This section therefore attempts to answer the question of whether it is possible to determine a way to objectively and accurately quantify radiation-induced DSBs and how we can best achieve this. Thus the first two chapters in this part are written so as to provide an adequate background as to how these images are produced. Since the endpoint tested is highly dependent upon the early processes in the chain of image formation, some time will be spent on introducing the basic principles using the fluorescent microscope and its corresponding dependencies, after which an introduction to the theory of foci counting (i. e. Chapter 2) and a table of the current literature is presented.

There are many different types of microscopes in use today, not necessarily based on the same physical principles of image formation. The first compound microscope - a series of two convex lenses, was developed in the 1600s, from work by the Italian Galileo and the Dutch Janssen brothers. Today though, microscopes have evolved into a range of types spanning from light microscopes to xray phase contrast imaging [94]. Each of these branches of microscopy has opened up even more sub-branches within their respective fields. For example, within light microscopy the following sub-branches exist: phase-contrast, dark field, polarisation, differential interference contrast, confocal laser-scanning and fluorescence microscopy; just to name a few. Therefore due to the shear scope of this field only the relevant mode, fluorescence microscopy is considered in this thesis.

1 Applicable to HeLa cells; lymphocytes would be 40 foci/Gy cell.

These categories can be further broken down when considering the various types of fluorescence microscopy. Microscopy techniques used for imaging fluorescent structures include: confocal, spinning disk confocal, multiphoton and widefield fluorescence. The best types of images in fluorescence microscopy are produced by the confocal microscope because these microscopes can restrict out-of-focus light in the imaging plane and isolate light mainly from the focus. The trade-off in reduced blurring, however, is a necessary increase in excitation intensity so that the samples are more subject to photobleaching. This pitfall, common to all types of fluorescence microscopy will be discussed in further detail in section 1.5. The focus here will be on image formation using widefield microscopy since, despite generally producing images of lesser quality compared to confocal microscopy, their ready availability and low cost means that widefield microscopy is in common use. The general idea behind fluorescence microscopy is to irradiate the whole sample with the appropriate wavelength and separate the emitted light from the excitation light so that only the excited light is detected. The main problem with widefield microscopy has already been alluded to - due to non-restricted excitation, light from out-of-focus regions enters the objective contributing to blur. To some extent, one can reduce this out of focus light using deconvolution methods, which mimic the quality of the confocal microscope. This will be discussed in further detail in Section 1.4.

1.1 FLUORESCENCE

The phenomenon of fluorescence dates back to 1852 when Stokes observed that the emission light was changed in colour after irradiating fluorspar[2]. However its usefulness remained unexploited until significant advances in genetic engineering were made in the mid-twentieth century in the jellyfish *Aequorea victoria* with Green Fluorescent Protein (GFP). At first, other sources of colours were formed by introducing genetic variants into the GFP gene, however later, coral reefs and sea aenemones were also found to be in possession of similar proteins, further increasing the number of available colours [140]. Molecules that can specifically target a biological identity and are capable of fluorescence are termed *fluorophores*. This is a subdivision of the definition *fluorochrome*, which is the general term used for fluorescing molecules [107]. A rigorous treatment of fluorescence will not be presented here, rather, the intention is to give a general illustration of some of the physical concepts relating to fluorescence and the effects they have on the results.

For an incoming photon of adequate energy, an atomic electron may be excited to a higher electronic state either in the singlet or triplet form. The excited states are defined by the electron spin ($-\frac{1}{2}$, $\frac{1}{2}$) so that the electron may be in either a singlet (S) or triplet (T) state, with the singlet state being preferred by nearly all molecules except for oxygen. In the singlet state paired electrons exist within a single orbital so that their magnetic moments cancel each other out and the total spin angular momentum s = 0. Whereas in the triplet state, electrons are unpaired and the total spin angular quantum number s = 1. Ideally, at some time later the electron spontaneously transitions back to the ground state via emission of some less energetic photon $h\nu'$, so that there is a difference between the energy of the excitation photon and emission photon. This difference is known as the *Stokes Shift* and the time delay between excitation and emission defines whether the process is considered fluorescent or phosphorescent. Fluorescence is the less delayed of the two and occurs $10^{-9} - 10^{-12}$ s after excitation, whereas phosphorescence may be of the order of seconds to days. An electron may return to the ground state by: internal conversion (transitions between electronic states) and/or vibra-

2 Mineral also known as Fluorite.

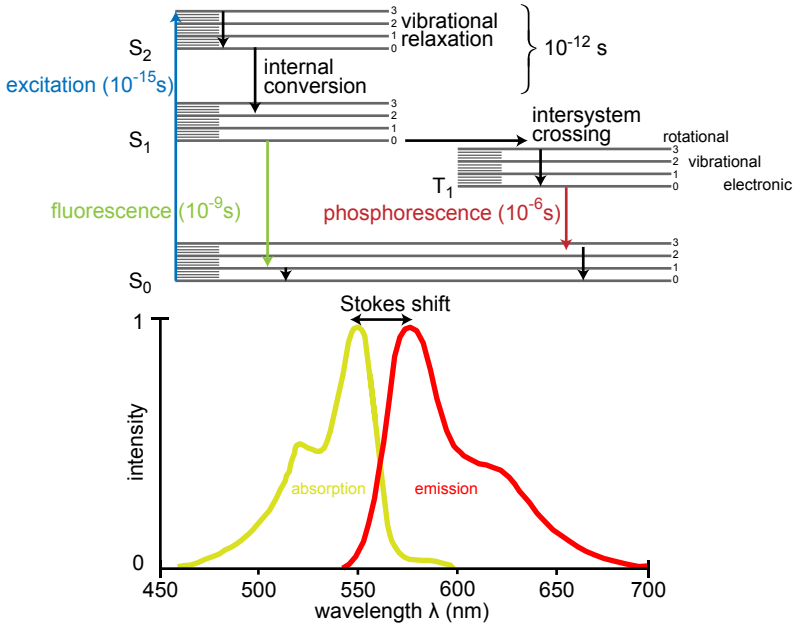

Figure 4: The process of fluorescence demonstrated with a Jablonsky diagram and the corresponding Stokes shift. The electronic excited states are the singlet S1 and S2 state (preferred) and the triplet state T1. Many possible modes of de-excitation are possible whereby radiation may be emitted - as in fluorescence and phosphorescence or in radiationless transitions - internal conversion, intersystem crossing or vibrational relaxation. The most common transitions for a fluorophore however are fluorescence emission and vibrational relaxation. The emission profile shown here corresponds to the Alexa Fluor 555 dye.

tional relaxation (energy transfer to neighbouring molecules such as water), which will bring the electron to the electronic S1 state after which fluorescence occurs. However since the triplet state and lower singlet state overlap energetically, there is a chance the electron will switch from a singlet to triple state. Since phosphorescence takes much longer (due to the transition of a forbidden process), another possibility is that another photon comes in and excites the electron into a higher triplet state. This is detrimental for several reasons: firstly because the emission is weakened by not transitioning through the phosphorescent stage; secondly because the fluorophore molecule has been removed from the excited state ground state cycling, responsible for fluorescence emission; and thirdly the triplet state opens up the strong possibility for photobleaching. These processes are illustrated with a Jablonsky diagram shown in Figure 4.

1.2 FLUORESCENT PROBES

When considering the appropriate fluorescent probe for fluorescence microscopy it is useful to consider the probe's photostability (how durable it is to the effects of bleaching and quenching), localisation, and chemical structure (most importantly the quantum efficiency Φ, denoting the fraction of energy loss via fluorescence), which affects the ease of detection [128]. Fluorescence decays exponentially with time over the order of nanoseconds, a factor, which can change according to whether it is bound or unbound to a biological molecule. The fluorescent probes discussed below are examples of immunofluorescence except for DAPI, which directly binds without the aid of an antibody.

Immunofluorescence utilises covalently bonded fluorophores to an antibody. Detection involves a primary antibody which is raised against some antigen in a host of different species e. g. mouse-anti-γH2AX: raised against γH2AX (antigen) in a mouse. The secondary antibody then needs to be *raised against* the same species as the primary antibody but *raised in* a different host species e. g. sheep-anti-mouse-Cy3: raised against mouse antigen in a sheep and conjugated with the fluorophore. Note the fluorophore is on the secondary rather than the primary antibody, which is known as an indirect method of immonofluorescence. The fluorophore can

of course be tagged to the primary antibody (direct immunofluorescence), however an indirect approach leads to higher signal because the secondary antibody will have more sites to which it can bind [103]. A schematic of indirect immunofluorescence is shown in Figure 5a. Though fluorescence markers are numerous, for brevity only those that were used in this thesis are discussed in the following.

DAPI (4′,6-DIAMIDINO-2-PHENYLINDOLE) was first synthesized in Erlangen in 1971 with therapeutic intentions [30], however some years later, was found to be a nucleic acid stain that is now a standard in fluorescence microscopy. Being a nucleic acid stain, the molecule binds to both double strand-DNA (ds-DNA) and single strand-Ribonucleic acid (ss-RNA), however its affinity for RNA binding is not only much less, but involves a different mechanism [1]. DAPI shows a high affinity for A-T bonds in the DNA, which are associated with the minor grove - see Figure 5b. The A-T is thought to be preferred because the minor grove is narrower and has a more negative electrostatic potential so that the DAPI molecule binds well [67]. In its pure form, DAPI exhibits significantly less fluorescence (20x less) than when bound to ds-DNA. Thus this molecule has found application in staining cell nuclei for widefield fluorescence microscopy (among other uses). It is excited in the ultraviolet spectrum at 358 nm with either Hg or Ne arc lamps or UV lasers. The emission is blue at a wavelength of 460 nm and offers very good contrast when used with multiple staining agents.

CY3 comes from the family of cyanine dyes specifically sulfoindocyanine, which means the molecular configuration has a site available for biological attachment [29]. Furthermore the presence of the sulfonate group makes them highly soluble in water thereby reducing fluorescence quenching that may be the result of dye-dye interactions [2]. The sulfoindocyanine molecules typically fluoresce at longer wavelengths, thereby making them useful in differentiating between unavoidable levels of autofluorescence, which tend to be of shorter wavelengths. Cy3 is excited at a wavelength of 550 nm and emits light at 570 nm (orange). Although its quantum yield is relatively low, this can be increased by limiting the degrees of freedom in the molecule and thus energy loss in a process called rigidising, to drastically increase the quantum efficiency from 0.14 to 0.9 [29]. In the data presented here, Cy3 is used for γH2AX foci.

ALEXA 488 belongs to the family of Alexa Fluors, which are a relatively new form of fluorophore [91]. The numbers in their names approximately correlate to their excitation wavelength, which span a wide range of colours. Thus for Alexa 488, the absorption max is at 495 nm and the emission max at 519 nm (green) [1]. It has a quantum yield of 0.92 [1] and was used in our study to image 53BP1 foci.

1.3 ASPECTS OF THE FLUORESCENCE MICROSCOPE

The biggest obstacle in fluorescence microscopy is the appropriate separation of the (relatively) high intensity excitation light from the weak emission light. Initial versions of the fluorescent microscope were used in transmission mode where the sample is uniformly excited by a light source that first passes through some transmission filters. The emitted light from the sample (along with a significant portion of the excitation light) passes through the objective. Since production of fluorescent light is a very inefficient process (3-6 orders of magnitude less than excitation intensity), the specimen is poorly illuminated with respect to the background, resulting in images with poor resolution and contrast. Today though, most fluorescence microscopy is

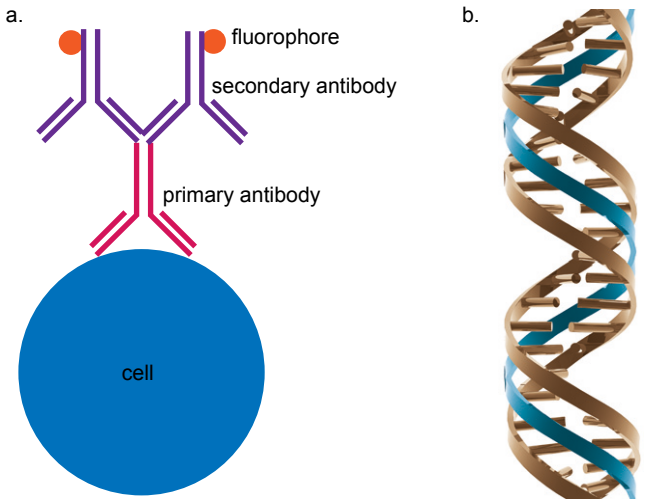

Figure 5: a. Indirect immunofluorescence utlises two antibodies, where only the secondary antibody has the fluorophore attached. By using a tagged secondary antibody, the signal is amplified because the epitope of the primary antibody allows for multiple binding. **b.** A DNA strand with the blue band running through the minor grove to which DAPI binds. Taken from [126].

performed in reflective mode (also known as epi-illumination) and as such is the main point of discussion. The optical light paths are compared between transmission and reflective mode in Figure 6. Microscopes in reflective mode can offer high resolution and well-contrasted images through the use of a dichroic beam splitter. Thus longer wavelengths ($h\nu'$) are transmitted while the short wavelengths ($h\nu$) are reflected. This configuration means that the objective also acts as a condensor, which is responsible of directing the cone of light onto the sample because it is perfectly positioned such that excitation light that is scattered/reflected will more likely be scattered away from the objective thereby reducing the amount detected to only a few percent [3]. Finally the appropriate combination between excitation and emission light for different types of fluorophores can be managed using a filter cube that readily switches the filter depending on the colour required for an arc lamp source.

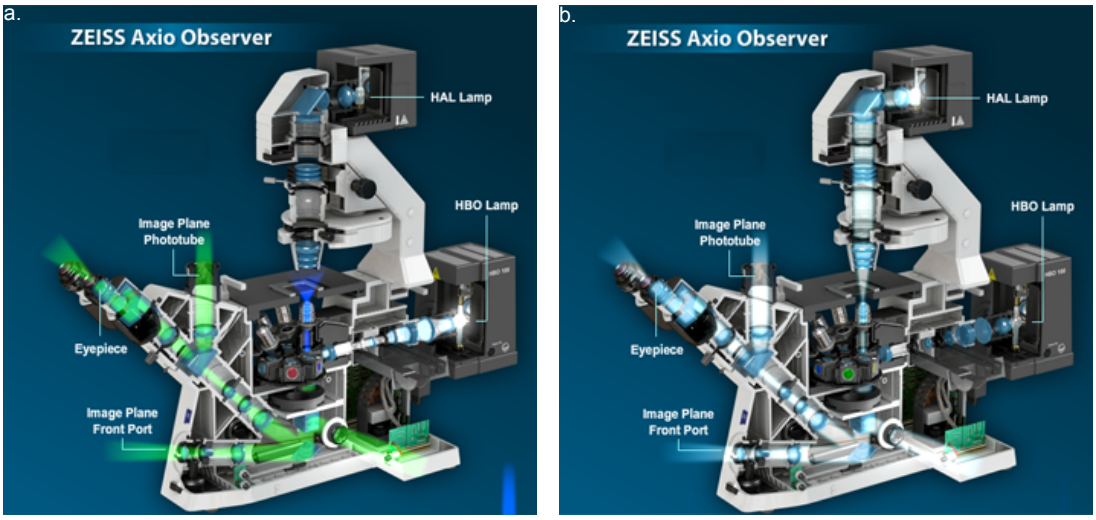

Figure 6: Schematic of a Zeiss inverted fluorescent microscope with the corresponding optical path. **a.** Epi-fluorescence mode modified from [107]. The optical train in reflected mode is shown originating from the Mercury arc lamp (HBO), where, after passing through the filter blue light, excites the sample so that green light emission is reflected back to the eyepiece appropriately separated from the blue excitation light. **b.** The optical train of transmission mode originates from the tungsten halogen lamp (HAL), illuminating the sample, whereby a significant portion of the excitation light remains with the emission light. Note the absence of the filter cube in the transmission mode.

1.4 IMAGE FORMATION

In general because of imperfections in imaging systems, an image is formed by the convolution of the object with a function that includes all the optical properties of the system, the Point Spread Function (PSF). The problem can be simplified by considering an object (say a small bead) with dimensions less than the incident wavelength so that, when viewing under the microscope, rather than seeing the pure bead as one would expect, a degree of blurring is introduced as a halo of disks as shown in Figure 7. This can be understood in terms of patterns of constructive and destructive interference owing to disturbances in the wavefront of the incoming light, which is now considered as a wave. The PSF is the intensity profile produced when viewing such an object, which therefore describes the properties of the system and as such is considered the fundamental unit in microscopy. If it were not for imperfections in the system, the ideal PSF would be a delta function. In practice though, according to how good the system is, the intensity profile follows a Bessel function of the form $\sin^2 x/x^2$, and if the system is capable of high resolutions, the width of the primary peak will be reduced. This principle can now be extended to larger objects so that the regions of constructive and destructive interference correspond to the image we see through the microscope.

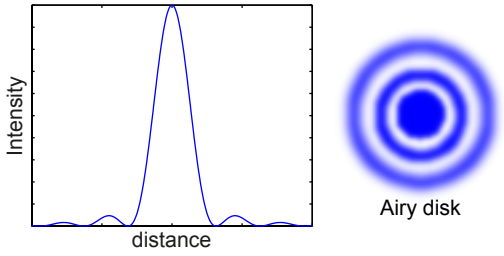

Figure 7: The fundamental microscopy unit - the PSF (left), and how it would be viewed under the microscope as an Airy disk (right). The Airy disk drawn here is rather exaggerated and in reality the rings would not be so pronounced, since ~84% of the light intensity is already captured in the zeroth order (i. e. the inner most circle) [86].

A description of *what* is viewed under the microscope has been presented, now a description concerning *how* the image is collected is given. Details concerning image digitisation are not given here, however readers are referred to [47] for further details. Up until the technique of optical sectioning [5], microscopy was limited to 2D images, where the only method to gain information concerning the inner portion of the sample, was to physically section through the sample (as in histological samples) and then image. Unfortunately this destroys the samples and exposes them to new dangers that were not present beforehand, however *optical sectioning* provides a way around this. In fluorescence microscopy, optical sectioning can be performed by recording an image at various depths along z, the optical axis rather than physically slicing through all the layers of the sample so that in effect a 3D image is formed. The process is demonstrated in Figure 8 where the resulting 3D image is also known as an image stack containing (in this example) four images beginning at z_{start} and finishing at z_{stop}. z_{start} is selected at the upper level of foci that are in-focus and z_{stop} is the lower boundary of in-focus lower foci. The image at a finite depth of say z_{start} will be made up of the highest foci, which will be in-focus as well as the out-of-focus foci at lower depths. The recorded image $g(x, y)$ is then the union of all the slices of the object of interest $f(x, y, z)$ between these two points. The-out-of focus information (i. e. blurring) is represented by the PSF $h(x, y, z)$, completely describing the properties of the image system. The image is therefore given by:

$$g(x, y, z) = f(x, y, z) \otimes h(x, y, z) \qquad x, y, z \in \mathbb{R} \tag{4}$$

Thus in order to recover the object, deconvolution techniques can be applied provided the blurring function (PSF) is known or can be estimated.

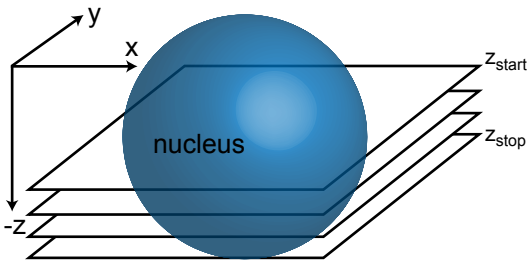

Figure 8: A 3D image is produced by optically sectioning the specimen at an appropriate Δz. If z is not sampled at a high enough frequency, information will be lacking, whereas oversampling is likely to contribute to photobleaching and not produce any further gains in image quality. In practice, around 20 images should be recorded in an image stack.

1.5 FACTORS AFFECTING IMAGE QUALITY

RESOLUTION Resolution here is the minimum distance required in order to fully distinguish two separate point objects such as that described in Section 1.4. The most important factors affecting the resolution are the wavelength λ, the angular aperture of the light cone captured by the objective α and the refractive index η. Thus it is given by:

$$R = \frac{\lambda}{2\eta \sin \alpha} \tag{5}$$

The denominator can be simplified now by defining the quantity, numerical aperture. This is one of the most important aspects of image quality as it defines the amount of light that can be captured by the objective as well as having an important effect on the magnification.

$$NA = \eta \sin \alpha \tag{6}$$

As always, there are limits to which we may increase or decrease these parameters in Equation 5. For one, wavelength can only be utilised within the visible spectrum (300-700 nm). However from Equation 6, we can see that Numerical Aperture (NA) may be increased either through the effective aperture (geometrically reducing distance between objective and specimen) or increasing the index of refraction. Since the maximum, that the angle α can have is 90°[3], the index of refraction is the limiting factor in this equation. Thus the NA can be increased by using a small oil drop over the top of the coverslip as shown in Figure 9, which not only increases the NA but also serves to reduce reflection/refraction owing to the coverslip, thus improving the collection efficiency.

Returning to the problem of magnification, there is a limit beyond which increasing magnification will no longer be useful if the system is diffraction-limited. Diffraction limited systems refer to those that are limited by the inherent properties of light as a wave i.e. seen when viewing an Airy disk. Since diffraction effects are most pronounced when the object to be imaged is of a comparable order to that of the object being viewed, then in order to increase the resolving capacity of the system such as what would be necessary for some biological processes, shorter wavelengths need to be produced. This typically means utilising wavelengths out of the visible range, which need to be produced by high energy accelerators.

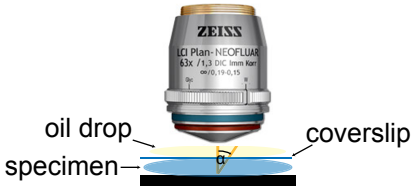

Figure 9: Physical representation of the numerical aperture, which relates to the amount of light that can be captured by the objective. Increasing the half angle α and the index of refraction η between the objective and the coverslip will serve to maximise NA. Note in the inverted configuration as used in our own experiments, the objective sits below the sample (coverslip faced downwards).

3 Practically this is more like 72° [4].

CONTRAST Contrast relates to the ability to produce bright, well-defined structures with respect to the background. In other words, maximise the emitted signal and minimise the excitation signal as well as background. Separation of excitation from emission is relatively well accounted for using the microscope in reflective mode as well as selection of the appropriate filter to produce the excitation energy. Since the intensity observed is proportional to NA^4, in order to maximise collection efficiency, NA should be as high as possible. However the intensity of the emission may be reduced by using a higher magnification governed by the relationship $1/\text{magnification}^2$, thus yielding an upper limit to the amount of useful magnification. Background is also problematic, since it is native to all cells because of endogenous metabolites[4] that autofluoresce and thus contribute to background [86]. It is reduced for fluorochromes with longer wavelengths [1] but is increased using fixatives, a necessary chemical used to preserve the cells so that they are 'frozen' in time. Background may also be reduced by restricting the illumination to a smaller region, but this reduces the Field of View (FOV). The signal is also influenced by the choice of fluorophore, concentration of fluorophore, type of cell and choice of emission filters. A final note on contrast during the procedure itself is to ensure that the full dynamic range is used, meaning that stimulation should be enough to produce bright structures, but at the same time not too much so as to produce high levels of background.

BLEACHING AND QUENCHING Photobleaching is one of the most serious effects to consider when conducting fluorescence microscopy. It occurs when, despite increasing excitation intensity, the number of emission photons cannot be increased - an *irreversible* effect, which is thought to be related to the oxygen content in the sample. As alluded to in Section 1.1, excitation to the triplet state is thought to have important consequences concerning the image quality. This is because firstly, the triplet state is much longer lived than the singlet state and secondly because electrons in the triplet state are more reactive. Thus interaction with molecular oxygen is more likely in the longer lived triplet state and if energy is transferred to molecular oxygen, it in turn is excited to a singlet state (photo-oxidation). The results of this may be responsible for inactivating neighbouring fluorophores [74]. Indeed our own experiment suffered from these effects, whose ramifications will be discussed in Part III Section, 4.

Quenching effects are similar to photobleaching in effect but the mechanisms differ somewhat. This is because quenching is a *reversible* process which does not have any effect on the photostimulation curve. It is due to short range interactions with the molecular environment and is considered to be reversible, because once these molecular agents are removed, the cyclical process of fluorescence can return.

4 Small molecule intermediates and products of metabolism.

2 THE THEORY OF AUTOMATED FOCI COUNTING

Foci counting is a staple of radiation-induced DSB analysis with a high demand for automated techniques. Over the years since the publication of the γH2AX assay [106], many people have sought to develop a method, which would automatically count the foci not only in an accurate and unbiased way, but also in the least time-consuming manner. Automated foci counting ranges from freeware, generally implemented through Java in ImageJ [98] up to commercial applications. And although many methods are available, many biologists are reduced to manual counting because it is still the easiest and most reliable way of foci counting, even if the most frustrating.

An automated method of foci counting that is often used is based on the method outlined in [26]. Though cheap, flexible and fast (faster than manual counting), it is subjective (because of its flexibility) and assumes a homogeneous foci number per cell per microscopic field of view. The assumption of homogeneity is a critical one in the analysis of the pulsed protons experiment because the dose was inhomogeneous. Whereas in other experiments this assumption would only be neglecting variances in cell uptake and fixation of the fluorescent marker, here, because the accuracy of the analysis would be restricted to the *average* of the dose and foci/cell per FOV of the microscope, unnecessary errors would be introduced.

2.1 ANALYSIS OF THE PROBLEM

When encountering the problem of automated foci counting, the following points need to be considered:

IMAGE FORMAT For the problem of automated foci counting, image format here refers to as whether the the analysis should be performed on 2D versus 3D (stacked) images, raw or deconvoluted. Most of the methods to date have been established with 2D images for simplicity using an intensity (usually maximum) projection. The maximum intensity projection image is produced by selecting the pixel with the highest intensity along the z axis, thus compacting the 3D stack into a 2D image. Evidently this is much faster as well as easier to verify with manual results, however the process is open to errors regarding loss of information as well as perhaps magnifying noise, which might otherwise have gone undetected due to the smaller size. Comparing a deconvoluted to a raw image, some methods produce better results in the raw image [16] despite blurring. In principle one would expect that the deconvoluted image is better because the blur has been removed; the images in this instance are definitely better in terms of contrast. However the choice of deconvolution algorithm such as whether it is based on a numerical solution to estimate the PSF or has been measured experimentally are amongst the many variables one can experiment with to produce varied results in the deconvolved image. This effect will be discussed in further detail in Section 4.4. In the usual sense, image format refers to how the image was saved such as tif, jpg, png etc. To clarify, images captured in the raw format are in an uncompressed format from Zeiss (.zvi) containing all three channels, whereas the deconvolved images were saved in uncompressed tiff format with one file per channel.

WIDEFIELD VERSUS SINGLE CELL APPROACHES Concerning this aspect, one must consider whether the widefield approach (i. e. processing all cells in the microscope FOV simultaneously) is appropriate for the data. The choice is an important one because it will affect the type of software that is used, since the majority of softwares are on widefield basis. Such a restriction is valid, however, when cells are irradiated with a uniform dose so that a uniform response (i. e. number of foci) is expected per FOV. Therefore it is of little consequence when all cells are processed simultaneously with a single set of input parameters for all cells in this FOV, because the average will actually be a fair representative of the biological effect.

THE EFFECT OF THE CHOSEN ALGORITHM The type of algorithm that is chosen can have a drastic effect on how many foci will be detected. Most programs approach the problem using one or a mixture of the following techniques: edge detection (e. g. Hough transformation), thresholding (e. g. Otsu's Method), region-based (e. g. region growing) or morphological watersheds (e. g. Watershed Segmentation). The complex and vast field of image segmentation will not be discussed here in detail, however the key algorithms will be briefly outlined before being presented in the review of automated foci counting; this is mainly to highlight the differences between the approaches, rather than be an exhaustive description. In practice then, the user is forced to make the 'correct' choice concerning the intensity threshold and volume of the structure at hand, and define essentially, what a focus is.

2.2 IMAGE SEGMENTATION ALGORITHMS

2.2.1 *Hough Transform*

The Hough transform [63] is an edge detection segmentation algorithm that works via a coordinate system transformation, best suited when parametric equations of the edges exist. For the simplest case, a straight line is used to illustrate this concept as demonstrated in Figure 10 where *points* on a line in *xy* space can be transformed into *lines* in *ab* space that always intersect at the point (a′b′). This can be extended now into polar coordinates so that *xy* space transforms to ρθ space to produce sinusoidal curves. By subdividing ρθ space into accumulator cells, the counts in the accumulator cells can be used to determine edges in the *xy* space, which could easily be managed by some thresholding. In order to make sense of the image, some connectivity rules are applied later on. The general procedure for this process is summarised into the following steps: first apply an edge detection algorithm, apply the transform, divide the transformed space into accumulator cells, assess according to pixel counts. This transform is likely to be the second edge detection algorithm used to assemble the preprocessed image into meaningful information, since the initial edge detection algorithm is generally unable to adequately separate the edges from noise. Thus a major disadvantage to this method of segmentation is the need for preprocessing of the image.

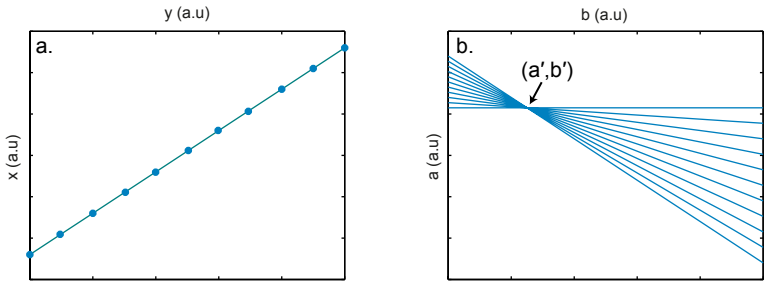

Figure 10: The line in *xy* space *y=ax+b* can be plotted in *ab* space using *b=-xa+y*. All points on the line in *xy* space will intersect at the point (a′b′) in *ab* space. Thus peaks in the image in *ab* space will correspond to edges.

2.2.2 *Otsu's Method*

Otsu's method [89] falls under the category of *Global Thresholding*. Otsu's method works by finding the threshold that produces the maximum variance between two pixel classes such that no *a priori* knowledge is required beforehand. The method can be summarised by normalising the image histogram, which represents the probability distribution. The pixels are then divided into two pixel classes $P_1(k)$ and $P_2(k)$ according to a threshold k. The mean of the first class m_1 is calculated from $P_1(k)$ and the mean of class two m_2 with $P_2(k)$. The global mean m_g using the entire image is also calculated so that:

$$P_1 m_1 + P_2 m_2 = m_g$$
$$P_1 + P_2 = 1$$

And k is the threshold when the variance is maximised, which can be evaluated by the dimensionless separability measure parameter η where $0 \leqslant \eta \leqslant 1$

$$\eta = \frac{\sigma_B^2}{\sigma_G^2}$$

where σ_B is the between-class variance and σ_G is the global variance. This formulation is easily expanded to multi-thresholding.

2.2.3 *Region Growing*

Region growing is a subset of region-based segmentation. These types of algorithms work by directly finding the regions; in contrast to Otsu's method, which uses intensity thresholding based on the pixel distribution. Instead of examining intensity distribution, region growing looks for the regions to be segmented directly, known as the *seeds* [47]. The seeds are then grown out according to shared pixel properties up to a certain point, based on a stopping rule. The seeds may be based on *a priori* knowledge, or else the properties of all pixels are examined individually and clusters are searched for. The centroids of the clusters can then be used as the seeds, which need to exhibit some minimum degree of connectivity.

2.2.4 *Watershed Segmentation*

The connectivity requirements of the segmentation algorithms can be disadvantageous. Algorithms that already incorporate this idea, however, are known as morphological watersheds. The general idea can be illustrated by considering the image as a topographical 3D image in which high intensities represent the peaks. Regional minima corresponding to the gaps between these peaks are a collection of points satisfying the condition that if water were to be dropped from above, it would collect at a single minimum; these are termed catchment basins. Next, water is imagined to incrementally rise from the base of these catchment basins so that if it were allowed, the water would eventually spill over into neighbouring catchment basins on a "first in first out" basis (FIFO). Dams, however, can be constructed to prevent slippage so that in a region of multiple catch basins, the tops of the dams correspond to those points that satisfy the condition that the water will fall with equal probability to neighbouring catchment basins. The points that satisfy such a condition are called the watershed lines and thereby retain connectivity. Thus, the goal of these segmentation algorithms is to find these watershed lines, defined by the dams. These general ideas form the basis of morphological watersheds;

further details can be found in [47][15]. In practice, these algorithms tend to overly segment the image. There are some ways to account for this, one of which is through the use of image preprocessing, which again demonstrates that no method is perfect.

THE TOP HAT TRANSFORMATION is not strictly an image segmentation algorithm, rather an image processing technique used to prime the data before applying a threshold segmentation algorithm such as Otsu's Method. Such a transformation can be applied to images with uneven background illumination by reducing the extremes between light and dark regions of an image. The transformation works by first eroding an image f with a structuring element b (defined by Equation 7); and then dilating (defined by Equation 8) [47]. This process is called *opening* an image by b shown in Equation 9. The top hat refers to the opened result being subtracted from the original image, shown in Equation 10. Because the structuring element 'doesn't fit' into the small high intensity peaks, the tops of the peaks will be clipped off. In this way the average background is changed and thresholding can be more easily applied.

$$[f \ominus b](x,y) = \min_{(s,t)\in b} f(x+s, y+t) \tag{7}$$

$$[f \oplus b](x,y) = \max_{(s,t)\in b} f(x-s, y-t) \tag{8}$$

$$f \circ b = (f \ominus b) \oplus b \tag{9}$$

$$T_{\text{hat}} = f - (f \circ b) \tag{10}$$

2.3 REVIEW OF AUTOMATED FOCI COUNTING

A summary of current methods is presented below along with some relevant comments taken from the corresponding publication. The purpose of the tables is to show the methods that are available (to my knowledge) and highlight the flaws associated with each method, giving necessary reason as to why these methods were not used in the analysis here. Many of these methods can produce good results and are in common use today, however due to the inhomogeneous dose distribution with which the cells were irradiated as well as the complexity and/or costs associated with these other methods, it was necessary to develop a new method. A final caveat to the tables is that only methods that count foci per cell and not integrated γH2AX intensity[1] were included in these tables. In addition methods that are/will be neither available to the public through freeware (see Table 1) or commercial use (see Table 2) have also been disregarded.

2.4 INTRODUCING FOCIPICKER_3D

Summarising the available methods of automated foci counting at present, it's apparent that due to the specialised nature of the experiment, it was best to use a method that could analyse single cell foci numbers. Thus the possibilities available to us for analysis are quite diminished, from which we decided to use the FociPicker_3D [36][37] due to its simplicity and ability to discern 3D objects. FociPicker_3D uses region growing segmentation to produce masks of the foci in the cell. The details of the algorithm have been described elsewhere [37], so that here we assume the core algorithm need remain essentially untouched. Analysis can be performed

1 Integrated γH2AX with immunoblotting is another common measure of DNA damage using γH2AX.

on either a 2D intensity projection or a 3D stack of images. The program requires a single cell image as input after which a Graphical User Interface (GUI) appears where the user can input parameters specific to the cell in question upon which the program runs. The key input parameters are known as the tolerance value t and minimum volume V. The latter is given in units of pixels so that for increasing size of minimum volume, less foci are detected. The tolerance value specifies the minimum range of pixel intensities that should appear in a focus and so is an absolute number depending upon the properties of the image. As such, a larger tolerance value then reduces the number of foci that are detected by the program, which are shown as the coloured peaks in Figure 11.

The result is a foci mask along with a log file of results, which can be exported into excel. Though the program is easy to use and produces good results, several problems were encountered using it in its initial form:

- The program can only be used through a GUI: In order to make this program usable for High Throughput Analysis (HTA), the program needs to be called automatically, i. e. respective input parameters need to be read in and images need to be opened/closed without user interaction.
- The GUI requires a single cell input: Cells therefore need to be isolated from each other in the microscope FOV image and managed logically.
- Choice of input parameters: Most input parameters could be left on default settings, however for the volume and tolerance value, a reasonable value needed to somehow be selected.
- Results need to saved per cell: Output results are viewed in log files and tables and therefore not automatically saved though the possibility to export results to an excel file exists; again requiring user interaction.

Thus though we have at our disposal the core algorithm that in principle can deduce the 'correct' number of foci, the ambiguity in choice of input parameters and the fact that the program is not automated make it difficult for objective analysis of HTA. To review the problem, this section must deliver two things: execution of the program so that the procedure is automated and the user would not be required to make these decisions per individual cell; determine the appropriate combination of input parameters that yields the known linearly increasing dose response of foci against dose.

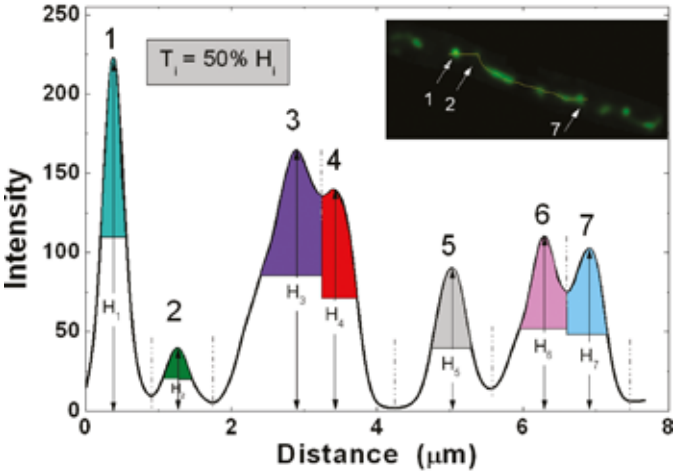

Figure 11: Line profile illustrating the concept of tolerance value taken from [37]. The coloured regions at the numbered peaks are detected by the program according to whether T_i exceeds the given tolerance value, which is an absolute number according to how many pixel intensities are in the image. For example if the given image were 8 bit, then the tolerance value cannot be greater than 256, similarly for a 16 bit image, where it cannot exceed 65536. The 50% fraction is adjustable however here it was left as is.

Table 1: Comparison of foci counting methods. Asterisks $*$ indicate that this method can be be used for single cell analysis. This table shows freeware methods that are accessible on the internet; references can be checked for details.

REFERENCE	IMPLEMENTATION	ALGORITHM	COMMENTS
Cai et al. [26]	ImageJ	Watershed	• Macro, which cannot completely separate overlapping foci (>30%). • Underestimation of foci at higher doses, semi-automatic.
Carpenter et al.* [27]	MATLAB/c++	Based on Otsu's method	• Designed for high throughput screening using 'pipelines'. • Optimised thus for 2D images. • Setting up "*may take several days*".
Du et al.* [37]	ImageJ	Region growing	• Requires manual cell outlining. • Input parameters must be defined per cell.
Gerashchenko et al. [43]	ImageJ	Voxel-sized colocalisation-based	• RAD50/MR11 proteins rather than γH2AX foci detected. • Based on user-defined threshold.
Hou et al. [62]	ImageJ	Otsu's Method	• Easy to implement. • Assumes a homogeneous dose across widefield image.
Ivashkavich et al. [64]	Not given	Top Hat H-Dome transformation Intensity threshold	• May be difficult due to large number of parameters. • Not yet available. • Image processing involved.
Jucha et al. [66]	ImageJ	Top Hat transformation Intensity threshold	• Available on Windows and linux but not supported on Vista. • Image processing involved.
Mistrik et al.* [82]	Multiple softwares	Manual intensity threshold	• A macro of user-defined procedures, which "*can crash unexpectedly*". • "*Not recommended to run on office computer*". • Uses image enhancement techniques in Photoshop.

Table 2: Comparison of foci counting methods. None of the softwares shown here have been personally tested, however Metacyte has been used by a colleague [145] at a collaborating institute from whom the corresponding comments are derived from.

REFERENCE	IMPLEMENTATION	ALGORITHM	COMMENTS
Barber et al. [10]	LabWindows/CVI	Hough Transform (CHARM)	• Requires *a priori* knowledge of approximate foci size. • Some involved setting up required. • Speed is comparable to manual counting although reduces counting bias.
Böcker et al. [18]	Image-Pro-Plus	Top Hat transformation Watershed	• May underestimate overlapping foci. • Image enhancement used.
Hiemann et al. [58]	AKLIDES	Object segmentation histogram-based and threshold algorithm	• Integrated image capturing component. • Forces certain image requirements for analysis.
Leatherbarrow et al. [73]	Quantity One	not given	• Foci number based on most intense light emission, thus tends to underestimate. • Foci size ranges from 1-4 px thus some overlapping takes place.
Roch-Lefévre et al. [105] Valente et al. [127]	Histolab	Top Hat transformation Intensity threshold	• Semi-automatic. • Cannot distinguish for overlapping cells >20%. • Image enhancement used.
Vandersickel et al. [129]	MetaCyte	Direct spot count 3D spot count	• Direct foci count results in underestimation of foci. • 3D counting is processor intensive. • Requires training the program (first 100 cells must be scored manually).

3 IMPLEMENTING FOCIPICKER_3D FOR AUTOMATED COUNTING

3.1 DATA PREPARATION

As mentioned in the previous chapter, the FociPicker_3D program functions only on single cells. Thus the cells needed to be isolated into individual images from the widefield image. Since ~15 cells are in a microscope image, it is essential to come up with way to not only first contour the cells but second maintain the huge amount of data in a structured way. This was done by writing a program in Java mostly via the ImageJ Application Programming Interface (API) called CellContourer3D [1]. The program takes two or three input images, which for our purposes were the Dapi (blue), Alexa488 (green) and or Cy3 (red) channel. The program operates by cutting out a Region of Interest (ROI) on a copy of the image, but the original input images are kept and marked so as not to contour the same cell twice. The procedure is detailed as follows:

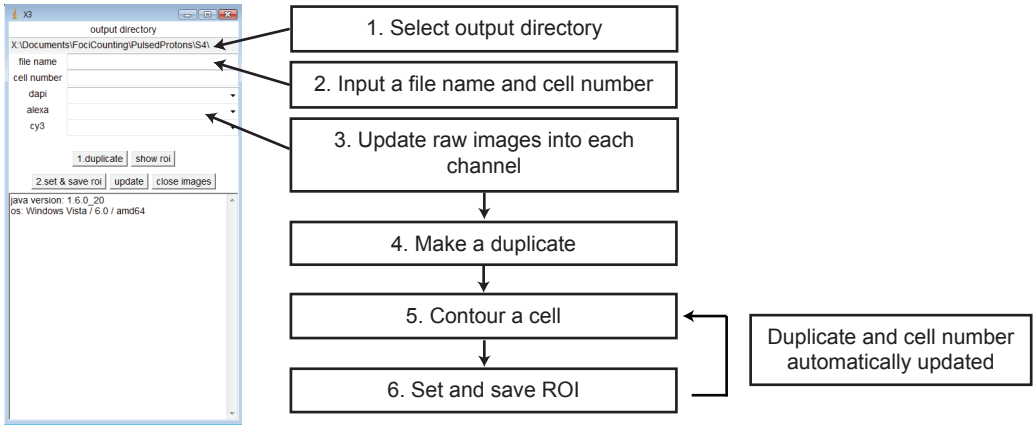

Figure 12: The CellContourer3D GUI alongside the procedure for using the program. Steps 1, 2 and 3 can all be interchanged in order however the duplication in step 4 is critical in outlining the first cell in the microscope image, after which this step is condensed into the *set and save* function. Thus the overall procedure has been minimised to steps 5 and 6 for each cell in the image and the overall number of clicks required is minimised.

To contour, any of the ROI cutting tools provided by ImageJ including a rectangle, circle, and freehand can be used. For irregular shaped ROIs, outside of the boundaries, the area is set to black. Therefore using either the circle or freehand tool serves the additional advantage of eliminating noise outside of the cell, for that which has not been completely eliminated in the deconvolution process. Once the cell is outlined, the program automatically saves the maximum intensity projected images, the 3D image stack and a corresponding text file of the ROI size, coordinates and cell number. The data is binned into folders according to its name, 3D stack/projection then respective channel in the relevant root directory defined at the start of contouring. The entire process of contouring a cell and saving the subsequent data was

1 Developed upon X2_ : Christoph Greubel, Universität der Bundeswehr München. The program produces average intensity projection images by selecting the top and bottom of the image stack. Information can be saved in individual text files per cell image.

therefore minimised to a contour then single click. This was an important consideration in the design of the program due to the high volume of data required for processing.

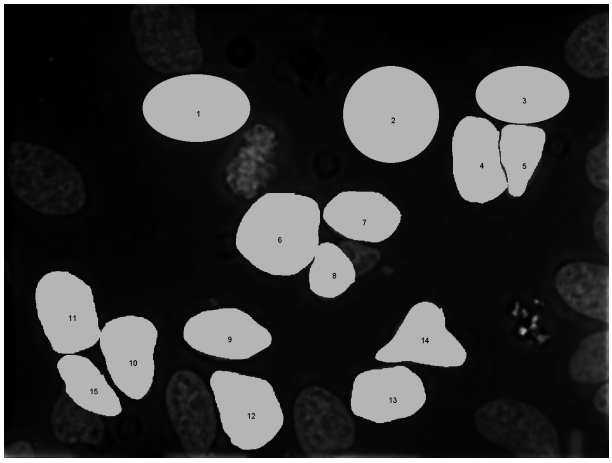

Figure 13: Final Dapi slice of a completely contoured microscope image. Either overlapping, mitotic or borderline cells are excluded from the analysis. Cells already contoured are 'greyed out' and imprinted with a number to keep track of and identify cells later for dose analysis. Here, the oval/circle and freehand ROI have been used for cell contouring. An average box requires ~2 minutes to contour, where speed is mainly limited by the time to write the file to the hard drive.

The next problem is then to determine an appropriate tolerance values per cell. The problem of what might be a reasonable tolerance value could be framed by considering how a focus might be defined. One proposed method has been to define foci as only those that occur both in the Alexa488 and the Cy3 channel. This therefore leads onto a discussion on colocalisation; the following section is based on this principle.

3.2 COLOCALISATION-BASED FOCI COUNTING

There is evidence to suggest that 53BP1 and γH2AX foci should be colocalised at the site of the DSB [87][14]. When choosing parameters appropriate to foci counting, it is therefore tempting to use this information as a decisive element in separating repair protein-induced foci from noise. Just as the question of how a focus should be defined remains unclear, the concept of colocalisation itself is subject to ambiguities. For an excellent overview of freely available techniques the reader is referred to the tutorial review article by Bolte and Cordeliéres [20]. Two of the most elementary definitions of colocalisation are investigated - the first being that two objects are colocalised when their pixel intensities fall within a certain range; this is referred to here as *Intensity-based colocalisation*. The second definition investigated would define two objects as being colocalised when lying within a certain number of pixels; this being referred to as *Coordinate-based colocalisation*. Since many images had missing data from the γH2AX channel, simply finding colocalised foci and then including only those that were consistent in both channels as might be carried out in other analyses, was not feasible here. Instead, a relationship was hypothesized to exist that could be modelled based on the parameters that produced these colocalised foci, and applied to data that was lacking in the missing channel.

3.2.1 *Intensity-based Colocalisation*

Assuming the colocalised pixels represent biology and not noise, a relationship was hoped to be established between colocalised foci and tolerance value to objectively determine this parameter. A mask of colocalised pixels was obtained by adapting the plugin Colocalization_Finder[2]. The ROI in the scatter plot 14c reflects the intensity incidences common to image 1 I_1 (Figure 14a) and image 2 I_2 (Figure 14b), such that the x-axis contains the intensities of

2 Christophe Laummonerie and Jerome Mutterer, Institut de Biologie Moleculaire des Plantes, Strasbourg, France.

I_2 and the y-axis the intensities of I_1. Since both I_1 and I_2 are 8 bit images, the axes are thus from 0-255. Thus the majority of the data resides in the bottom left quadrant since most pixels in I_1 and I_2 are black ($I = 0$) or close to it. Colocalised pixels are shown in white as depicted in Figure 14d. Comparing the mask of foci with the actual image however showed poor correlation, thus invalidating this method.

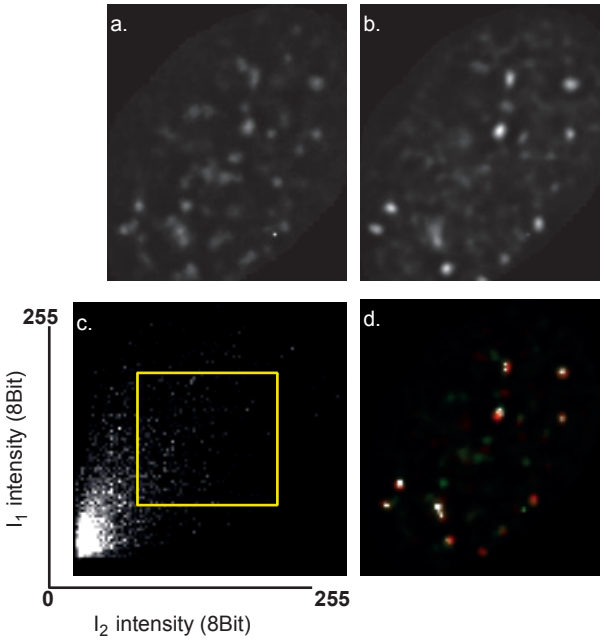

Figure 14: a. and **b.** I_1 and I_2 corresponding to the maximum intensity projections of the γH2AX and the 53BP1 respectively channel.
c. Scatter plot of the intensities in both images with the default ROI centred on the plot. In this current version though, the ROI starts in the upper right corner and progressively increases up to a threshold of colocalised pixels.
d. The corresponding mask and overlay of both channels. Colocalised pixels are shown in white and depend on the size and position of the ROI. Thus larger ROIs correspond to more correlated pixels so that the number of regions in the mask not only increase in size but number as well. The number of clustered regions in the mask was used to deduce the tolerance value, which would produce such a number of colocalised foci.

3.2.2 *Coordinate-based Colocalisation*

An investigation was also conducted to determine whether the xy coordinates of the foci found by FociPicker_3D could be used to define the input parameters. Here FociPicker_3D was run over a low tolerance value (~1000 for a 16 bit image) in both channels such that a greater number of foci than those likely to be actually existing were detected. Colocalised foci were defined to be true when the x and y coordinates lay within 4 pixels of each other. The foci detected using such a tolerance value to generate the number of colocalised foci, did not correlate well with the colocalised foci. Thus although some degree of colocalisation between the Alexa488 and Cy3 channel was observed this proved to be not so useful in determining reasonable input parameters into the program.

Finally, the ways in which these types of colocalisation could not be used in automated foci counting can be summarised by the fact that the intensity-based colocalisation essentially required thresholding to determine the degree of colocalisation. Thus in having to address such an issue, another definition is required for which no real answer exists and so adds to the problem. Furthermore for these thresholds that were tested, the tolerance values obtained that would produce the corresponding degree of intensity-based colocalisation showed an inconsistent number of foci between the foci generated in FociPicker_3D and the original image. For the coordinate-based colocalisation, although this additional threshold would not be necessary, the inferred tolerance value to generate the colocalised number of foci produced foci whose were not visually consistent with the original images.

3.3 OTHER METHODS FOR AUTOMATED FOCI COUNTING

Other properties of the images were also investigated as reference points to determine the program parameters. Outlined below are the various attempts at determining adequate input program parameters. In the ensuing sections, all methods were performed on the maximum intensity projection images. Although this results in some loss of information, it is useful for the investigative stages because firstly, processing is orders of magnitude faster than 3D and secondly, we assumed that the radiation is low LET and so produces non-dense foci structures that should not overlap one another.

3.3.1 *One Tolerance Value for All Data*

A tolerance value $t = 2000$ was used for all cells and yielded relatively good results; good results being a linearly increasing dose response. However this method was discarded because firstly, the controls were too high, and secondly, it is difficult to justify why one value should be selected over the other. This latter point demonstrated an optimum dose response of $t = 2000$ in one data set but $t = 3000$ in another data set. For future experiments, no gains have been made in determining a good, uniform way of determining input parameters for the program. The dose response is shown in Figure 16a and b.

3.3.2 *Average Tolerance Value per FOV*

In order to reduce the effect of outlier cells, an average tolerance value per widefield FOV was determined based on individual tolerance values per cell t'_i. This was calculated using a fraction, γ of the maximum pixel intensity I_{max_i} in each cell i and N is the total number of cells in an image.

$$\begin{aligned} t'_i &= \gamma \cdot I_{max_i} \\ t &= \frac{1}{N} \sum_{i=1}^{N} t'_i \end{aligned} \tag{11}$$

tested at $\gamma = 0.05, 0.10, 0.15$ and 0.2. t was then applied to all cells within an image however the results again were unsatisfactory regarding the expected number of control foci and the linear dose relationship. The dose response is shown in Figure 16c and d.

3.3.3 *One Tolerance Value per Cell*

Alternatively, to make t as specific to the cell as possible, it was applied to each individual cell:

$$t_i = \gamma \cdot I_{max_i} \tag{12}$$

The effect now is that the tolerance value appears to be too low in the low dose region (and thus too many foci are detected) and too high in the high dose region (resulting in too few foci detected). This is shown in Figure 16e and f.

3.3.4 *Normalising the Image*

In order to account for t being an absolute value, normalising the image was also investigated so that this number would effectively become relative. This seems reasonable since by normal-

ising the images to a universal reference point, the effect of absolute parameters could then be considered as relative as well. The image was normalised by scaling to some value with respect to the maximum of the histogram so that a single absolute tolerance value could be used. For example in a 16 Bit image A the position of the histogram peak was found at a bin with a pixel value of 50. Therefore the new image, $B = A \cdot 20$, so that the new peak position is at 1000, after which a tolerance value of 2000 can be applied to the image and then foci were detected.

Several problems were encountered with this method though:

- If the position of the peak in the histogram was too low, the corresponding factor by which the image had to be multiplied was so large that the noise was blown up to a level that would detect many more foci than actually exist. This often meant that the FociPicker_3D was stuck in an infinite loop. Thus the factor needed to be restricted accordingly, which meant that our data was no longer treated in a uniform manner.
- For histogram peaks at the high end of the spectrum, the limit of a 16 bit image was exceeded. Thus forcing the normalised image's peak to the upper bin of the histogram and in doing so, lose a non-negligible amount of information.

This last point particularly led to the conclusion that this method could not be considered as an acceptable option.

3.3.5 *A Background Noise-based Method*

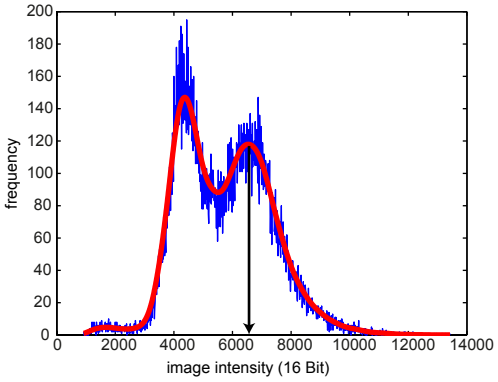

Figure 15: An example of an image histogram of a cell that had not been exactly contoured to the border of the nucleus. In this case, some background of the image appears as an additional peak to the background of the cell. In such a case, the peak with the higher bin position was taken as shown with the arrow. The goal here is to use the position of the bin ($x_{max} = 6540$) as a reference point to find t.

The image background, rather than the maximum pixel intensity was used as a reference point to determine a tolerance value; motivated by the noise being a stable marker across the cells. Since a higher portion of the image is represented by background this should theoretically be a stable characteristic of the cell and not subject to some random outlier fluctuations as might be seen for the maximum intensity pixel value. By detecting the position of the maximum peak, a multiple of its position to determine the tolerance value might be inferred. The main principles of the program are outlined as follows: the peak detection process was based on finding the maximum of a function that has been fitted to the image histogram so as to exclude random small fluctuations in the histogram followed by defining some minimum width and height the peak should have. Once the maximum intensity was obtained, the corresponding bin needed to be determined with a fine enough discretisation so as to prevent information loss. The final tolerance value applied was then tested using a linear relation with some scaling factor from:

$$t(x_{max}) = \gamma x_{max}$$

where t is the tolerance value as a function of x_{max}, the bin position at the maximum frequency and $0 < \gamma < 1$. A further complication also arose because some cells were contoured with rectangle ROIs and others with manual or elliptical ROIs. Since the contouring program sets the background automatically to zero, an additional peak could be found in some of the cells, which can be seen in Figure 15. Peaks were defined as those having a maximum value that was at least 20% as high as the maximum peak. The dose response is shown in Figure 16g and h.

Before introducing the final implementation Figure 16 is presented showing the most important methods attempted so as to give the reader a feel for the ways in which these methods failed and how they compare to each other. Mostly it was difficult to find a set of parameters that could be applied to both continuous and pulsed proton data sets whilst maintaining the right number of foci for the controls and at 1 Gy.

3.4 FINAL IMPLEMENTATION

The previous section is a sequential account of methods that were attempted and yielded poor results. However during the course of these methods some significant advances were made in understanding the image requirements for the program. Therefore although the background noise methods failed, further inspection of the histograms showed that some parts of the data were significantly noisier than others and that these images were the ones that actually led to the bad results. Consequently these images were discarded.

ASSIGNING THE MINIMUM RANGE OF PIXEL INTENSITIES WITHIN A FOCUS The tolerance value is determined utilising the image histogram where the image is sorted according to intensity bins x, which summed cumulatively give the area A. As mentioned in Section 3.3.3, the maximum pixel intensity M is not necessarily a stable representation of the image properties since this maximum could be a single pixel of noise. A new maximum pixel intensity is therefore defined that makes up the majority of the image histogram A'. As mentioned, the tolerance value may be a single value per cell, per microscope image or per experiment. The tolerance per microscope image was chosen since this reduces the effect of outliers. If there are N cells per image, A is summed over all cells in the image and t is the same for all cells in the image using:

$$\begin{aligned} A &= \sum_{j=1}^{N} \sum_{i=1}^{M^{(j)}} x_i^{(j)} \\ A' &= \sum_{j=1}^{N} \sum_{i=1}^{M'} x_i^{(j)} = 0.9999A \\ t &= \gamma \cdot M' \qquad 0 < \gamma < 1 \end{aligned} \tag{13}$$

DERIVING THE CRITERIA FOR A MINIMUM VOLUME To determine the minimum volume that defines a focus, the distribution of focus volumes in a data set is determined from whose estimated probability density function a minimum volume is calculated. Figure 17 shows the volume distribution of foci for all irradiated cells by running FociPicker_3D with a minimum volume of 10 pixels so that the program detects all foci as well as some noise. By fitting the data non-parametrically, no distribution is assumed and the fit is defined by the smoothing

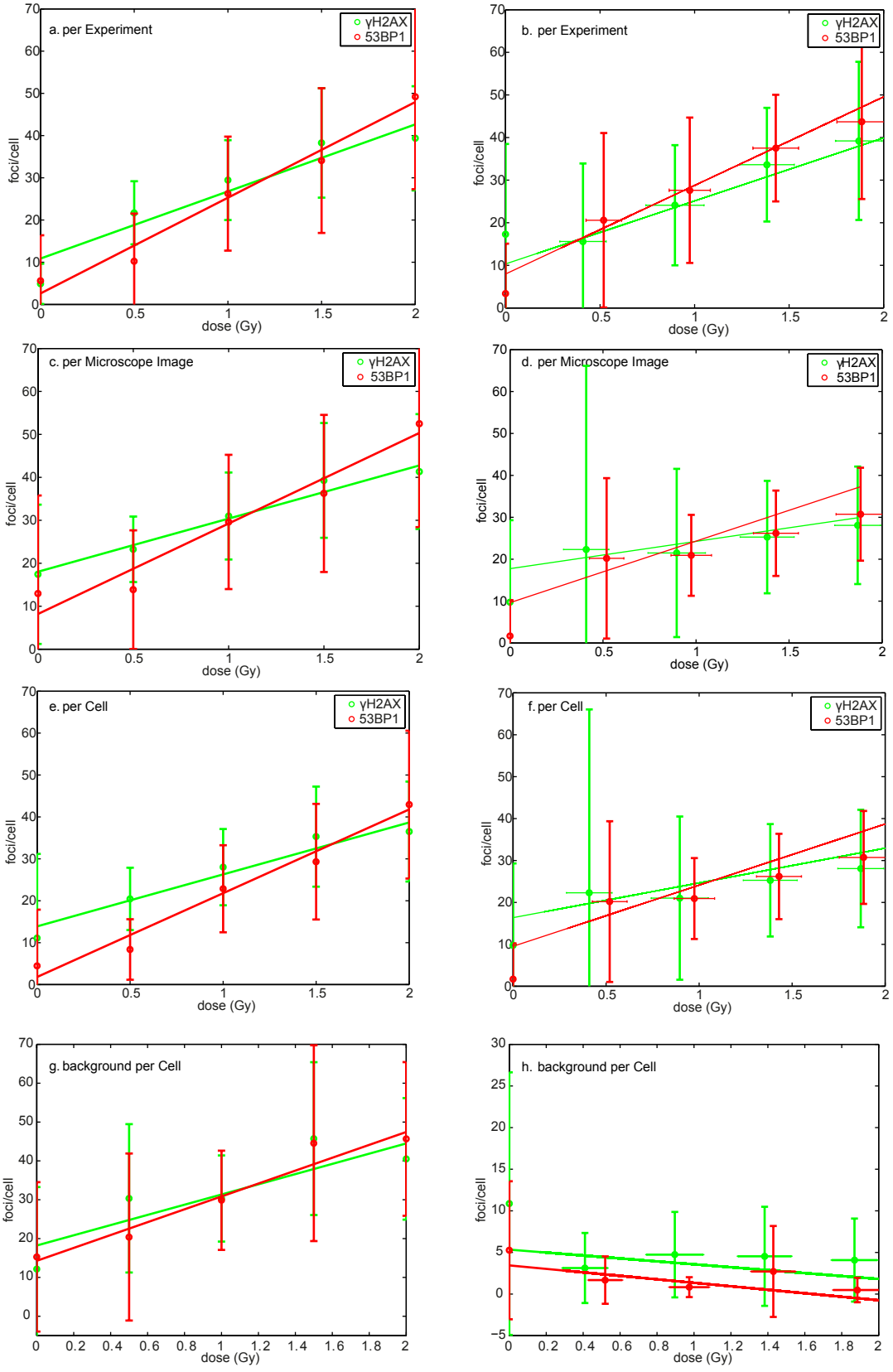

Figure 16: Dose responses for continuous and pulsed protons with various methods and constant minimum volume of 10 px. Error bars denote the standard deviation. The red data shows γH2AX and the green data shows 53BP1. **a.** Continuous protons dose response with $t = 3000$. **b.**Pulsed proton $t = 2000$. **c.** Continuous proton dose response using Equation 11 and $\gamma = 0.1$. **d.** Corresponding pulsed protons. **e.** Continuous proton dose response using Equation 12 and $\gamma = 0.1$. **f.** Corresponding pulsed protons. **g.** Continuous proton dose response with using the bin position of the histogram peak as a reference point for t. **h.** Corresponding pulsed protons.

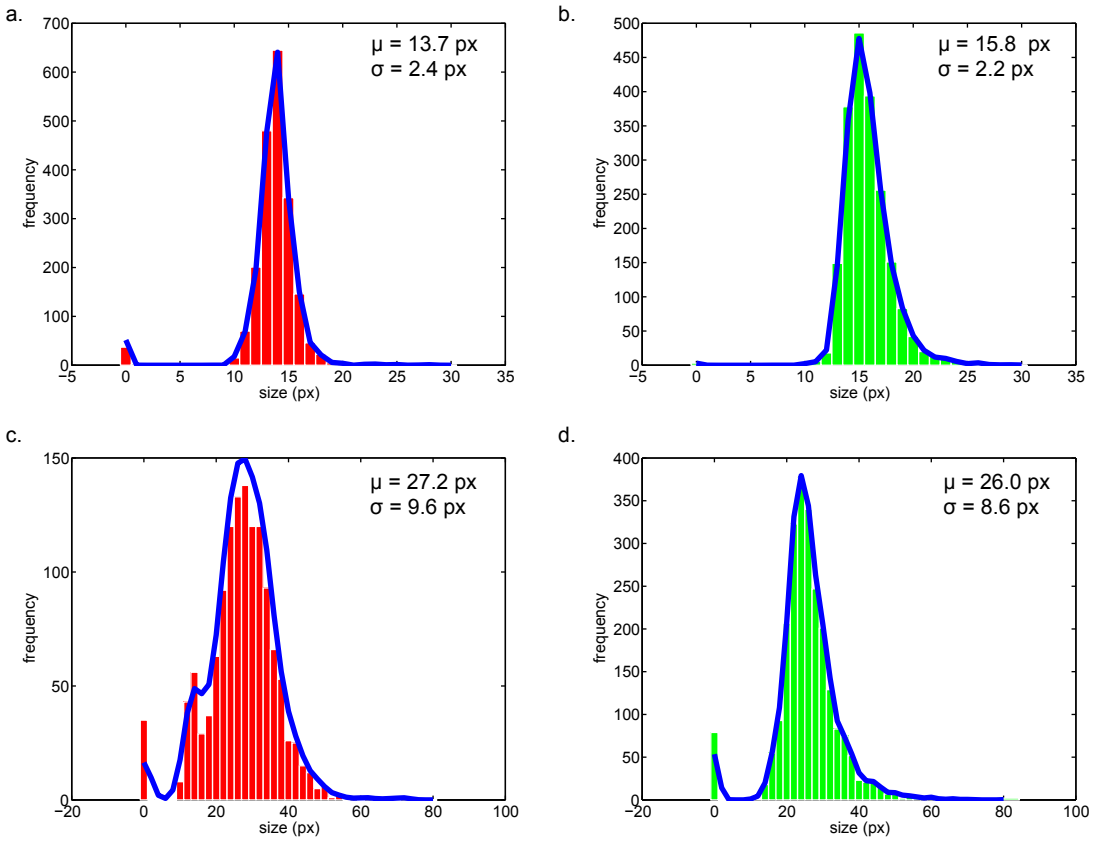

Figure 17: Distribution of focus areas for irradiated cells in 2D using the maximum intensity image projection. **a.** γH2AX volume distribution of continuous protons. **b.** 53BP1 volume distribution of continuous protons. **c.** γH2AX volume distribution of pulsed protons. **d.** 53BP1 volume distribution of pulsed protons.

Gaussian function, K to give an estimate of the probability density function $\hat{f}_h(x)$. This is calculated using the kernel distribution based on

$$\hat{f}_h(x) = \frac{1}{nh}\sum_{i=1}^{n} K\left(\frac{x - x_i}{h}\right) \quad -\infty < x < \infty \tag{14}$$

where n is the sample size and h is the bandwidth. Each data value is represented by the smoothing function, which when summed together gives a continuous $\hat{f}_h(x)$ as shown in Figure 17 as an overlay on each of the data sets. Based on the estimated $\hat{f}_h(x)$, the volume for a given data set is calculated using the following relation:

$$V = \mu - \sigma \tag{15}$$

where μ is the mean and σ is the standard deviation of $\hat{f}_h(x)$. The minimum volume in 2D is now 11 and 14 px for γH2AX and 53BP1 respectively for continuous protons. For pulsed protons it is 18 and 17 px γH2AX and 53BP1 respectively.

The final workflow of the automated method of foci counting is summarised as follows:

1. Cells were contoured using the program CellContourer3D in ImageJ.
2. Tolerance values were calculated using $\gamma = 0.1$ and Equation 13.
3. A minimum volume was defined using Equation 15.
4. The automated version of FociPicker_3D was run with the file produced in the previous step returning an output file containing the filename, tolerance value and number of foci.
5. Doses and foci were matched together and plotted based on the numbering scheme used in the filename to produce the dose response relationship.

The following section presents all the corresponding results from this method.

4

RESULTS

The results of the method detailed in section 3.4 are shown in Figure 18 with the maximum intensity projected images for the continuous and pulsed proton experiment. Because the input parameters that are passed into the FociPicker_3D program have a significant effect on the results, the most critical of these dependencies are examined below with respect to the fit line parameters of the dose response curve and/or the number of foci. The dose response curve has been fitted with a straight line of the form:

$$f = a_1 \cdot D + a_2, \tag{16}$$

where the foci f linearly increases with dose D in [Gy] according to the fit parameters $a1$ [Gy^{-1}] and $a2$. The data was fitted using ordinary least squares. In both the continuous and pulsed protons, because there is some plateau occurring around 2 Gy with respect to the 53BP1 channel, fitting a straight line to this response tends to lift $a2$. In order to account for the plateau, the fit line was performed for doses extending only up to 1.5 Gy. The results can be seen in Figure 18.

4.1 BINNING DEPENDENCE

A proof for the validity of this method is demonstrated with the pulsed proton data. Unlike the continuous data, where cells were irradiated at discrete dose intervals of 0.5, 1, 1.5 and 2 Gy, the pulsed proton data was over a continuum. Therefore when fitting the straight line to the data the effect of the number of bins B on the fit parameters was investigated. Data was binned using equidistant bin widths w starting from the minimum dose $D_{min} \neq 0$ through to the maximum dose D_{max}.

$$w = \frac{D_{max} - D_{min}}{B}$$

In Figure 19 the fit parameters are calculated for $B = 2, 4, ...20$ showing the fit parameters' slight dependence on binning, which is especially significant when less than 6 bins are used. Therefore since the error is minimised and a plateau region is reached after 6 bins, the fit line parameters are best taken from the data without binning as shown by the straight lines.

4.2 MINIMUM VOLUME DEPENDENCE

The number of foci can be filtered according to a minimum focus size [px]. Thus as the minimum volume is increased, the constraints allow for less foci to be found for a fixed γ. The concept is illustrated for the continuous protons in Figure 20, which shows that the program results are highly dependent upon the choice of the minimum volume for a fixed γ that has been tested at $\gamma = 0.05, 0.1, 0.15, 0.2$. For the volume range shown, a constant region in foci versus dose can be seen in the pulsed data shown in Figure 20e, where there appears to be a plateau. This can be understood in terms of the broad volume distribution seen in Figure 17(c and d), whereas for continuous protons, the gradient is sharply decreasing at a minimum volume of 15 pixels. Thus for a fixed tolerance value the gap between 0 Gy and 1

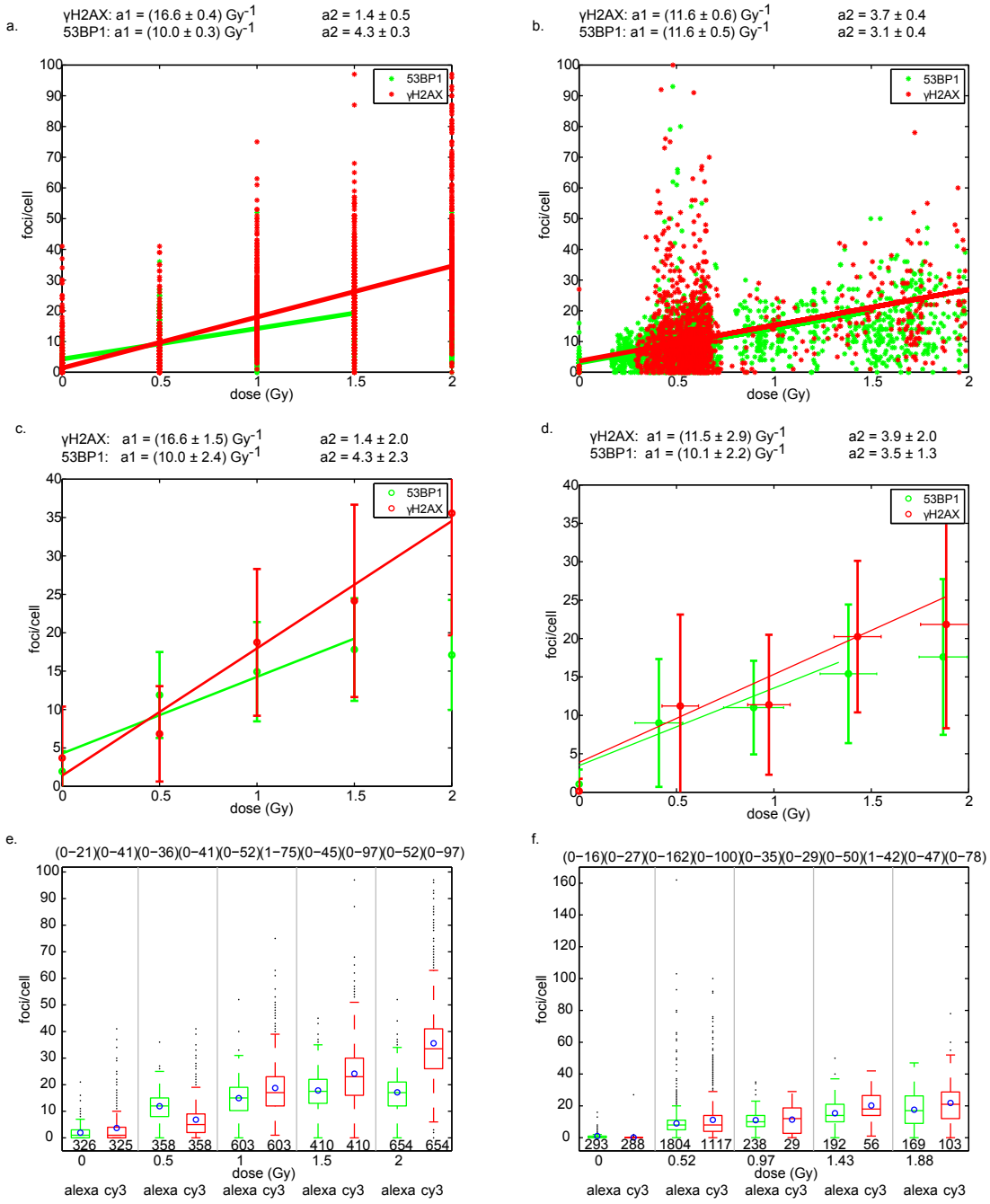

Figure 18: Results of the method outlined in Section 3.4. The relevant fit parameters are given in a, b, c and d where data >1.5 Gy in the 53BP1 channel was not used in the fit. **a.** Full data set with fit lines of continuous protons. **b.** Full data set with fit lines of pulsed protons. **c.** Continuous proton data shown as the mean of each dose point and the corresponding standard deviation in number of foci. **d.** Pulsed proton data binned with equal dose bin widths of 0.49 Gy (except for control data). The error bars indicate the standard deviation in both dose and foci directions. **e.** Continuous proton box plot. **f.** Pulsed proton box plot. The box plot shows the median within the box and the upper and lower boundaries of the box represent the interquartile range of the data per dose point. The whiskers show the extreme value limit (e. g. lower whisker=lower quartile value -1.5·lower quartile value) and any cells that are beyond the whiskers are presented as individual points known as the outliers. The number of cells per dose point are shown at the bottom of the graph and the range in number of foci is shown at top. The mean values are shown in blue circles.

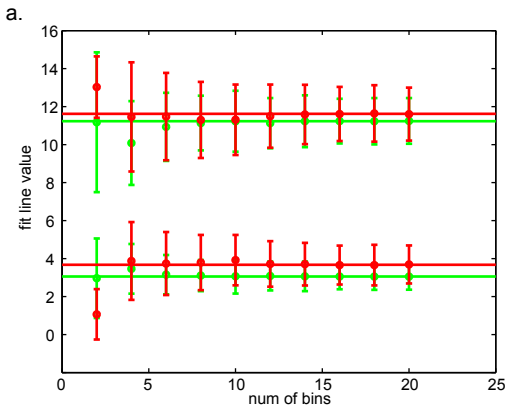

Figure 19: Fit parameter dependency on number of bins relevant only to the proton data. The top line is for the first fit parameter $\alpha 1$ and the lower line is for $\alpha 2$. No binning as shown in Figure 18a. and b. is given by the straight lines. Both the 53BP1 (Alexa488 - green) and γH2AX (Cy3 - red) channels are shown.

Gy increases with decreasing volume so that in order to maintain the necessary known values a corresponding decrease in tolerance value would be required.

4.3 γ FACTOR DEPENDENCE

The effect of changing the minimum range of allowed pixel intensities via the tolerance value was investigated at 5, 10, 15 and 20% of A'. From Figure 20, it can be seen that as the intensity threshold is increased, a corresponding decrease in minimum volume is necessary to reach the expected number of foci at a given dose level and Equation 13 would no longer hold. By comparing the figures of the various pixel intensities, we see that the behaviour remains more or less consistent across the data but the absolute number of foci is scaled.

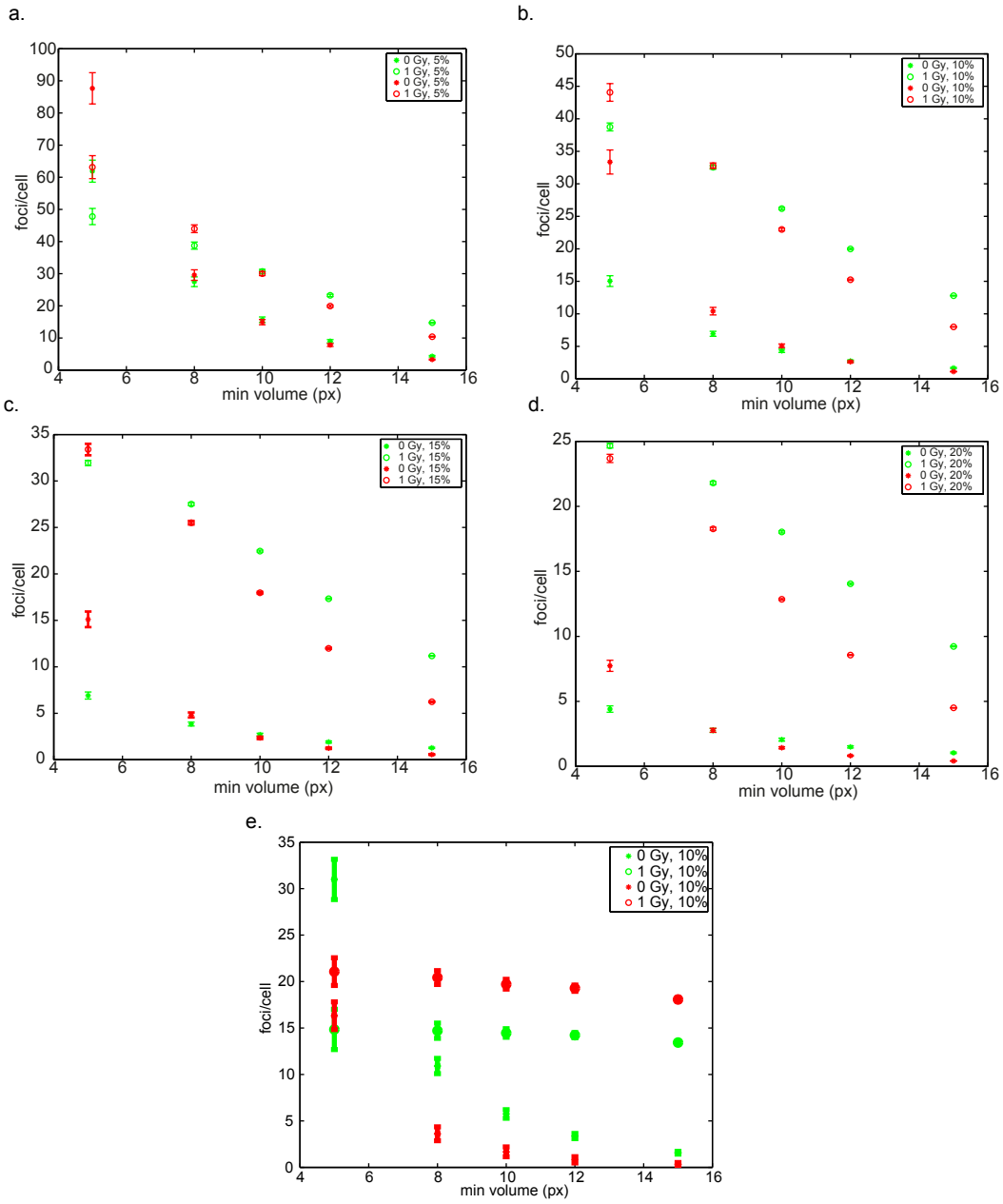

Figure 20: Comparing the effects of increasing the minimum range of intensity values at which foci are delineated via the tolerance value. The number of foci is shown as a function of volume for the control (0 Gy) and 1 Gy continuous proton data for **a.** $\gamma = 0.05$ **b.** $\gamma = 0.1$ **c.** $\gamma = 0.15$ and **d.** $\gamma = 0.2$. Evidently $\gamma = 0.05$ level is too low, since the effects of noise play too strong a role, whereas $\gamma = 0.2$ requires the minimum volume to be changed. **e.** Pulsed proton volume dependency with $\gamma = 0.1$ showing no variation in foci/cell at the 1 Gy dose level due to a wider volume distribution.

4.4 DECONVOLUTION DEPENDENCE

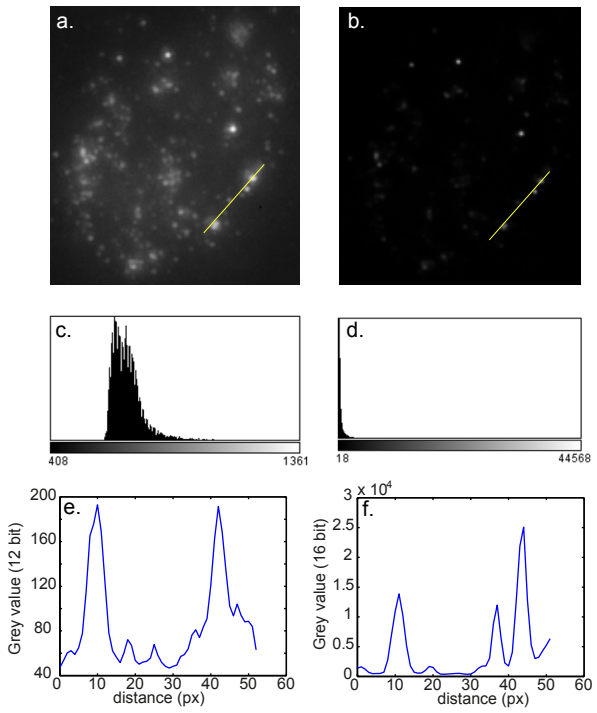

Figure 21: a. Raw image for a cell irradiated with 1 Gy xrays.
b. Deconvoluted image for the same cell.
c. Histogram corresponding to image in a. The histogram has a maximum value within the range of a 12 bit image since this is the .zvi format automatically saved using the Zeiss AxioObserver Z1.
d. Histogram corresponding to b. Following the deconvolution process, the image is converted into a 16 bit image and saved in the lossless .tiff format.
e. Line profile of Figure a.
f. Line profile of Figure b. Here the effect of deconvolution can be seen well where the foci have become more distinguished from the background so that the FociPicker_3D does not detect any foci in the raw image, in contrast to the deconvoluted case.

All images used in the analysis were of the deconvolved images. As described in Section 1.4, the image that we see is not precisely true to the object that is being imaged under the microscope. Since the perceived image $g(x,y,z)$ is a convolution of the object $f(x,y,z)$ with the imaging capabilities of the optical system i.e. PSF $h(x,y,z)$ (assuming a linear system), in order to improve the accuracy of the information we wish to view, deconvolution techniques are applied to the images. As mentioned in section 1.4, image processing is a subtly different process from deconvolution itself in that former distorts the object for some purpose. This may be to *enhance* a specific effect or aspect such as background reduction in a subjective manner. Whereas the latter attempts to *restore* the image to its original object by reducing the blurring created by the out-of-focus light and/or random noise in an objective manner [47][131]. Equation 4 is often ill-posed due to the difficulty in obtaining a good set of data from which the PSF of the optical system can be reconstructed. Multiple methods exist to deconvolute such an image; they may be via direct measurement of the PSF, blind deconvolution methods (numerical) or analytical [109]. Under the optical conditions used for the data here, the PSF has already been experimentally measured as well as numerically obtained via commercial software. Because experimentally measuring the PSF is difficult and tedious, and both methods were found to produce comparable results [52], the numerical method was preferred for the deconvolution.

Figure 21 compares the histograms of deconvoluted with convoluted images, demonstrating that the intensity peaks, which correspond to the foci are less defined and so difficult for the program to detect; this shows the sensitivity of the currently discussed method to the effect of deconvolution. This should be taken into consideration since not all institutes have direct access to deconvolution software.

5 DISCUSSION

Returning to the original question posed at the start of this section, we would like to determine whether there is a way to accurately automatically quantify the number of foci per cell and if so, what is the best way to achieve this? The results from the final method outlined here, corroborate the expected linear relationship between dose and the number of foci per cell [62][146]. The foci are extracted from the image using a region-growing algorithm which identifies the foci in a nucleus. This is based on growing out seeds, which must satisfy the tolerance value and volume criteria. Such an approach contrasts to the original γH2AX analysis whereby *immunoblotting* was used; involving a comparison between absolute levels γH2AX and H2AX [106]. Immunoblotting, however, would not have been possible with our data due to variations in dose. Also because of this, *immunofluorescence* analysis based on the widefield, intensity threshold-based approaches such as those utilising Otsu's method would result in too high an error when quantifying the number of foci/Gy cell [27][62]. Alternatively an integrated fluorescence intensity can be determined as Turner et al. have suggested for biodosimetry [125], which, in principle, could be calculated using the FociPicker_3D program, but is not shown here.

As detailed in Chapter 2, there are a number of different softwares available that are able to automatically quantify the foci, with the majority suited to widefield methods and require significant user-interaction; the latter factor not only present in freeware workflows such as that described by Cai et al. [26] but also in commercial software such as Histolab [127]. Consequently, analysis time can be lengthy should the user be required to make repeated adjustments in the program. While this reflects the flexibility of the program, it can also be subjective with regards to not only inter-observer variability but also intra-observer variability. As such, a key difference this method displays is the reproducibility of the data, which is as independent as possible of the analyst's actions.

From this study it was found that foci determination can be automated using pixel intensities via the tolerance value and fit parameters of the foci volume distribution via the minimum volume definition. Thus only two variables need be known to automate foci analysis; this being significantly less than Ivashkavich et al. [64]. The results generated with this method without using any image enhancement techniques is a promising feature in comparison to other automated methods that rely upon such modifications [27][64][66][82][81]. Although these modifications can be argued as necessary since the light intensity varies over a single microscopic FOV, this still distracts from the purity of the data, and is ultimately data interference. This is tempting, especially in images that have poor signal to background such as for one of the pulsed samples, which consequently had to be discarded. Had image processing techniques been applied, we might have been able to use all of the samples. Poor signal to background is most likely attributed to photobleaching when capturing the images, since when exciting the samples for an image, not only the FOV but also the surrounding area was exposed within a margin of ~100 μm. Since the images of the first sample were initially recorded systematically, moving downwards in a train and then back up again, it was some time before it was discovered that a change in image capture procedure had to be made. Thus perhaps a large component of this method's success owes to the large number of cells that were processed such that the effects of outliers had little relevance on the final result.

Typically the dose response relationship for radiation-induced cell damage displays a linear relationship. Although the controls receive negligible radiation, it is still possible that a DSB repair process is occurring, whether it be due to stress situations placed on the cells or even general repair processes encountered in every day life. However from the curves in Figure 18 the response reaches a plateau. This might be attributed to a saturation in response with the γH2AX assay. Therefore when fitting a line to the data, the plateau forced the control point (a_2) to a higher value due to saturation effects at high doses. This was accounted for by not including the last dose point when obtaining the fit line so that by including the large error bars and the low mean value for the controls, this value is not far from acceptable.

When considering the most important variables for foci expression the most important parameters can be categorised into: variances due to experimental procedures such as washing and staining of slides, variances in cell uptake of the dye due to damage to cells or stage of cell cycle at time of irradiation, exposure and biological effects of ionising radiation. Ideally we hope to purely see the latter variable, however due to the mixed effect of the other variables, the discussion becomes more complicated. Intuitively it was thought these first two effects should be eliminated as much as possible by conducting the evaluation per cell. However the best results were obtained with an average tolerance value per FOV applied to all cells in the respective image.

Therefore one can conclude that although these first two factors do play a role in the way we see the foci, the dominating effect is still the biological damage to the cell alone and so can be measured as an absolute in terms of intensity and volume, rather than having to adjust for each individual cell. It is likely that although variances in exposure and radiosensitivity play a role in foci detection with FociPicker_3D, the overwhelming effect is the dose response. To demonstrate these effects, the test cases 1-3 can be compared:

1. Multiple tolerance values applied individually per cell: Makes no assumptions concerning microscopy nor the way cells were handled.

2. Single tolerance value per microscopic FOV: Assumes variances only in exposure (whilst exciting the fluorophore during microscopy) and all other variables to be constant across the sample.

3. Single tolerance value per experiment: Assumes no variances in exposure, radiosensitivity (due to cell cycle) or biological handling.

It is likely that for case 3, too much information is lost as well as not being able to compensate for possible variations in scaling introduced by the deconvolution between images; whereas for case 1, outlier effects are given too much weight. Thus case 2 is argued to be the best compromise between tailoring for variances between images and minimising the effect of noise.

The investigations leading up to the final choice in parameters for the FociPicker_3D program highlight the importance of taking a good image at the microscope first time round. As pointed out in Chapter 1.5, due to the effects of bleaching, only one chance is offered to record the best image possible for analysis. Ideally a good image here should consist of such features as good signal to noise ratio, consistent exposure for all images and sharp, well-defined foci for which care must be observed in using the full dynamic range without saturating the signal. Concerning this factor, some methods of automation actually demand certain criteria in the images such as with the AKLIDES software by including the analysis component with image capturing to form a complete system [58][108]. Another way around this might have been to exclude out-of-focus cells such as proposed by Hou et al. [62]. Furthermore it would

also have been better had the images been equal in stack size, where the variation is due to selecting the upper border of where a repair focus is in focus down through to just before it goes out of focus. The implications being that if the images are not recorded well initially at the microscope, deconvolution can actually introduce errors in results by amplifying noise or reducing the signal.

The only degree of subjectivity here (and thus non-reproducibility in results), relies on the ability of the user to discern and discard mitotic cells in the cell contouring process. In this respect, cell cycle analysis would have been helpful. Hernández et al. are the only group to date who have incorporated cell cycle variability into their automated analysis, a factor which would possibly improve the results shown here [57]. At present, the major limitation is computational (on the contouring side), since the images are constantly being written to the hard drive. To give some approximate numbers, 2 minutes were required per FOV, equating to around 2 weeks of full time work for all three experiments.

Another time additive in the workflow is the writing of intensity values (i. e. tolerance values) into a file that can be read into the FociPicker_3D program. For simplicity, this was carried out in MATLAB, and provided the images are being read from a local copy on the hard drive, then to calculate and produce tolerance value data per experiment (for the data in this thesis), this has an order of magnitude of an hour. Thus the overall time required for analysis may still be comparable to manual counting, but this was also noted by Barber et al. in their method of automated foci analysis [10].

To summarise the limitations associated with this method of automated foci counting, the FociPicker_3D program demands well recorded images that can be accurately deconvolved such that they have good signal to background. Since the program only operates on single cells, there is a reasonable amount of time associated with contouring each cell from the data sample and the requirement that mitotic cells/border cells are eliminated; thereby requiring some judgement and thus possible error on the user's part. However running the FociPicker_3D for ~3000 cells, takes some hours, which compared to manual counting would still be preferable.

The state of automated foci detection programs is constantly improving. A major hurdle that current automated foci detection programs face concerns the 2D nature of the majority of automated foci counting softwares mentioned in the opening statements, thus a major way forward would be the development of such a program. Especially in the context of this thesis where we are dealing with potentially larger foci, the loss of information presented by 2D images, cannot compete with a method that is able to distinguish 3D images as well as the FociPicker_3D program. 3D data is something new, that few automated softwares are capable of implementing. As seen in Tables 1 and 2, 3D foci counting is difficult and this method of utilising the FociPicker_3D in a fast, efficient way could be very interesting to the community of γH2Ax analysis. Not explicitly mentioned here are the massive costs of such commercial softwares, which as a result, are not available to a large majority of institutions. The fact that FociPicker_3D is free and open source mean that it is likely this method can easily be expanded upon and further improved in future use.

Part III

FIRST CELL EXPERIMENTS AT ATLAS WITH LASER-DRIVEN PROTONS

1

THE BIOMEDICAL BEAMLINE

Since one of the main applications of laser-driven protons is intended for clinical use, it is necessary that biological experiments first be carried out to ensure that we completely understand the damage that laser-driven protons can induce. As already mentioned, production of laser-driven protons differs considerably to conventional methods. Thus the primary aim of this section was to optimise the setup for a low-energy proton cell irradiation and determine the RBE of laser-driven protons, thereby adding to our understanding of these particles. Optimising the setup prior to the irradiation was a necessary part of preparations for the experiment due to the unpredictability of the laser. The situation was additionally complicated by the low-energy protons so that special considerations were made concerning the transmission through the successive layers before irradiating the cells and dose detection. These preparations and methods unique to the laser system are outlined in the following section along with the ensuing results.

1.1 PROTON PRODUCTION

For simplicity, the set-up will be subdivided into 3 components: the process of proton production will be presented as a starting point for the experimental arrangement, followed by a description of the transportation methods before ending in the delivery of protons to the cells. In this way the complete path of the proton is traced from its production through to stopping. The setup is shown schematically in Figure 22.

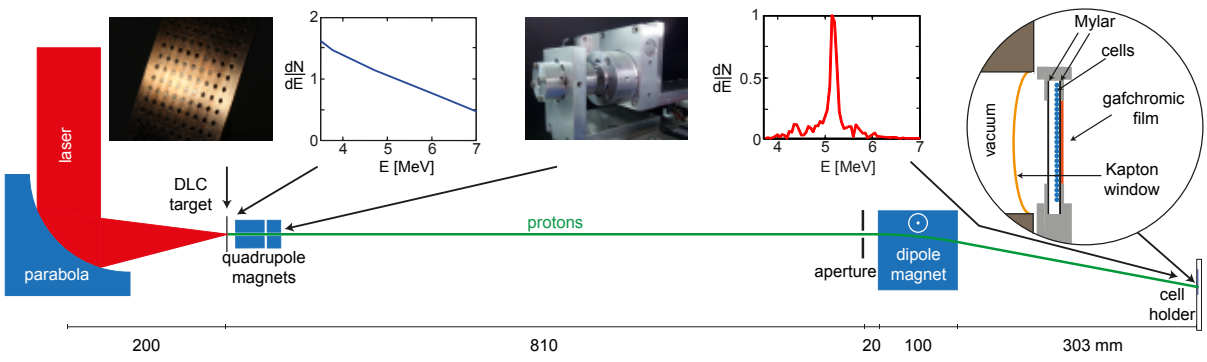

Figure 22: Scaled schematic of the biomedical beamline at the Max Planck Institute of Quantum Optics (MPQ). The laser is focused onto one of the DLC foils accelerating the protons out of the rear side of the target. Two mini-quadrupole magnets collimate the broad energy spectrum after which a permanent dipole magnet separates the protons from the xrays. The protons exit the high vacuum conditions via an exit window before entering the cell holder to inflict damage on the monolayer of cells on the back wall of the cell holder. Radiochromic film lies behind the cell holder.

Proton production is carried out at the Max Planck Institute of Quantum Optics (MPQ) with the ATLAS table-top Ti:Sapphire laser capable of delivering intensities of up to 10^{19}W/cm^2 in 35 fs with wavelength 795 nm. Although a relatively high intensity laser beam is produced through the exploitation of CPA technology, due to incomplete recompression of the pulse

[137], the resulting pulse is said not to be 'clean' with respect to the low intensity, albeit relevant prepulse, which if not appropriately cleaned, will destroy the target before the main pulse even reaches this point. A double plasma mirror is employed to clean the laser pulse by allowing the low energy prepulse to pass through, whereas the main pulse forms a plasma and is reflected off the surface. This results in a 10^{-8} contrast such that the final beam energy on target is ~0.4 J since the trade-off in superior contrast is a reduction in the beam energy. Once the prepulse has been reduced to an acceptable contrast, the laser strikes a 90° parabolic mirror to focus the laser pulse onto the target. The target is one of the defining features of the setup at MPQ in comparison to other groups [39][71][138], who have conducted likewise cell experiments with laser-driven protons, who tended towards thicker targets (order of μm). At MPQ the target is DLC, which is a type of amorphous carbon containing a mixture of sp^2 and sp^3 bonds. The latter to which DLC owes its diamond-like properties [56] thus making it a suitable candidate in laser-driven proton production because of the subsequent hardness and optically transparent characteristics of the material [77]. Over the course of the cell irradiation experiment, the target thickness used ranged between 20 and 40 nm, a value that has been optimised by previous measurements. The target itself is not large in size (~2 mm diameter), however quite a number of these are required, since upon interaction with the laser, the target is completely destroyed. Therefore for each shot, the beam needs to be realigned to a new target so that the most efficient way at present is to have the targets arranged in a lattice formation as seen in Figure 22. Consequently, due to refocusing of the beam between subsequent shots, the shot frequency is 1 per 10 minutes. Further details concerning the laser diagnostics can be found in [55] and on the target production in [77].

1.2 TRANSPORTATION

A key aspect in differentiating between the setup here and that of other institutes that have performed laser-driven cell irradiations, lies in the beam transportation. As mentioned in the introduction, under the current acceleration scheme, an exponential energy spectrum can be expected. As a result, the clean Bragg peak will broaden, so that a sharp definition in dose can no longer be expected. In order to ameliorate this, several setups have been proposed, one of which being through the use of two mini-quadrupole magnets, which focus the beam in the axial plane. The high magnetic gradient that is generated by such magnets thus collimates the spectrum into a quasi-monoenergetic spread. The trade-off that results in the reduced energy spread is a loss in fluence as well as an additional complexity in focusing the beam. Once the protons have passed through the mini-quadrupole magnets, another aperture filters the spectrum even more after which a dipole magnet of 0.9 T, separates the low energy protons from the xrays that are also generated in the plasma. The final energy spectrum is (5.2 ± 0.23) MeV, before exiting vacuum conditions.

1.3 DELIVERY

Since the beam is of such low energy, delivering the protons from vacuum conditions to the cells in normal aerobic conditions required appropriate design of an exit window and cell holder. Our system has the dosimetry downstream of the cells, so that the beam is attenuated first by the exit window made from 50 μm thick Kapton foil followed by the successive layers of the cell holder upon whose last layer the radiochromic film adheres to. The thickness of the Kapton foil might possibly have been halved so that the energy attenuation would not

be as great, however owing to the vacuum conditions in the beam line, it was decided to err on the safe side and endure the energy loss. Aside from biological reasons with respect to the analysis, energy transmission was also a reason for having the cells seeded onto a single layer on the rear window foil. As already mentioned, the cells need to be maintained under normal pressure on a thin layer on the rear foil window. The cell holder is thus two steel plates with Mylar foil on each side. Cell medium is also in the cell holder, where the cells are maintained in a horizontal position up until time of irradiation, during which they are positioned vertically as shown in Figure 23a. The Mylar foil onto which the cells are seeded contains a grid, which allows to localise dose to cells as shown in Figure 23b.

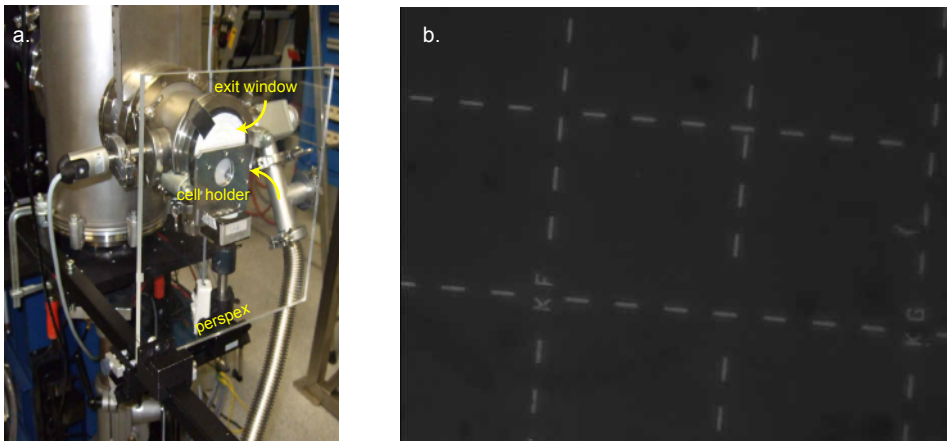

Figure 23: a. Key components of the proton delivery section to cells. The cell holder is placed at a height relative to the window taking into account the deflection from the dipole magnet upstream of the cell holder. The perspex window is also shown and marked behind the cell holder for radiation protection. **b.** Microscopic image taken with 20× magnification showing the grid and coordinates (KF) etched onto the back Mylar layer of the cell holder window.

Table 3 shows the laser diagnostics for 10 cell samples that were irradiated at the ATLAS laser under the biological conditions described in Section 2.3.

Table 3: Laser characteristics of 10 cell samples. The film dose is the average dose over the line focus 5 mm in length using a 6 MV photon calibration.

	CELL SAMPLE	TARGET THICKNESS (nm)	LASER ENERGY (mJ)	FILM DOSE (Gy)
day 1	S1	20	318	0.15
	S2	20	329.2	0.32
	S3	20	318	0.37
day 2	S4	20	385.4	0.38
	S5	20	396.6	0.38
	S6	20	385.4	0.26
	S7	40	389.1	4.24
	S8	40	400.3	1.22
	S9	40	400.3	0.96
	S10	40	392.8	1.21

The column of cell samples shows the names assigned to each irradiated cell sample; this naming system will remain throughout the rest of the chapter. The following section of methods is concerned primarily with the delivery portion of the beamline; specifically the dosimetry and biological analysis necessary to judge the properties of laser-driven protons with the intention of clinical use. Further details concerning the proton production and transportation can be found in [16].

2.1 DOSIMETRY

The uniqueness of the laser-driven cell irradiation placed some specific demands on dosimetry, which are not commonplace in clinical radiation dosimetry. From previous measurements of the ATLAS laser characteristics, the energy and dose were known to be inhomogeneous across the line focus. However precisely because of this feature, a complete dose response could be acquired in a single shot of the laser and in doing so avoid the long irradiation times associated with laser-driven cell experiments by which an insight into the pulsed nature of the dose delivery could be provided. Thus by simply selecting various regions of the line focus produced by the quadrupole magnets, regions of low dose right through to high dose could be extracted - see Figure 24. The challenge in this procedure however is to be sure that the dose recorded in the film corresponds to the biological damage seen in the cells according to their position.

Although other dosimeters such as image plates are often used in detection of laser-driven protons [99], radiochromic film is advantageous here firstly because it can be easily positioned immediately behind the cells and secondly because it can be scanned in as an image so that all

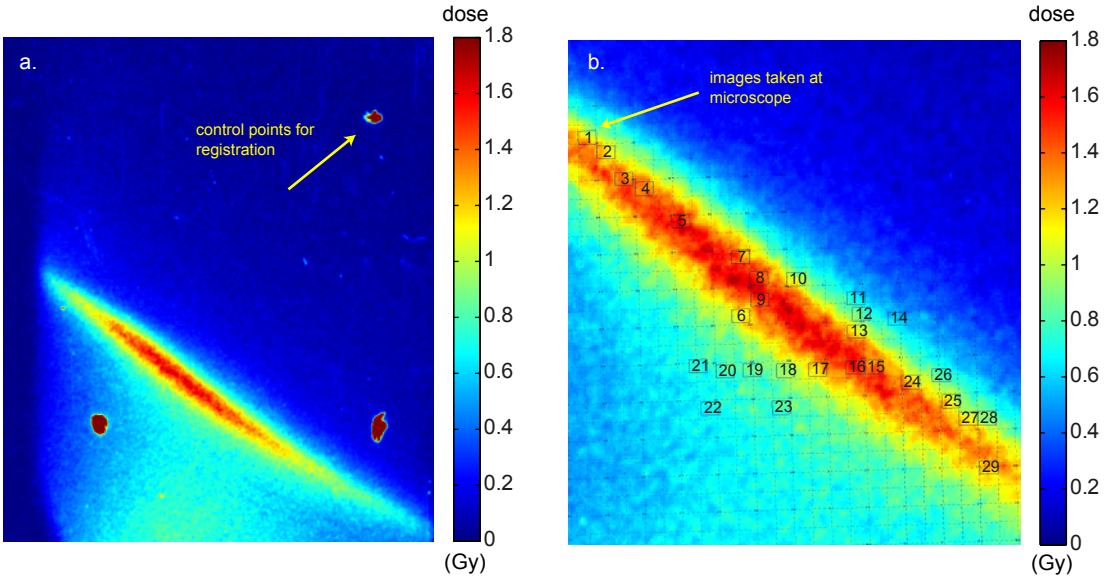

Figure 24: a. Dosemap produced in a single laser shot showing the line focus of S10 before registration to grid (see Section 2.2.2). The dose shown here is the dose when variation in stopping power is taken into account as well as the low energy response. The calibration used here was performed with 6 MV photons. **b.** Registered dosemap to grid image of S10 where the microscope images numbered from 1-29 are spread out over different regions of the line focus in order to generate a complete dose response (< 2 Gy). The grid has a resolution of 150 µm and a coordinate at every 300 µm.

the image registration and processing techniques would be at our disposal. Therefore the first step in the process is to determine the calibration factors necessary for dose determination. EBT2 film, calibrated at the radiation therapy department at Klinikum rechts der Isar with 6 MV photons, was the radiochromic film of choice. The film is self-developing and is essentially an active layer (where the dose is detected) sandwiched between some clear polyester layers. The structure of the film can be seen in Figure 25. The dose is detected via a dose-dependent film darkening due to polymerisation in the film [69] so that the darkening (known as the net optical density OD) is obtained using the background pixel intensity I_0 and the irradiated film pixel intensity I in the red channel. The dose in the film D_f can be calculated using the net optical density and calibration factors $a = (10.44 \pm 0.30)$ Gy, $b = (59.53 \pm 3.61)$ Gy, and $c = 2.8$ from:

$$\text{netOD} = \log_{10} \frac{I_0}{I}$$

$$D_f = a \cdot \text{netOD} + b \cdot \text{netOD}^c$$

If the beam had been high in energy, the dose measured in the film would have been sufficient. Since this was not the case two corrections needed to be applied with the dose to the cells D_c given by $D_c = D_f F_1 / F_2$. F_1 and F_2 are described below:

1. Owing to the rapid energy degradation penetration depth, the dose detected in the film was greater than the dose delivered to the cells. This might be pictured by overlaying a Bragg peak over the successive layers traversed by the protons, so that we are on the rising edge of the Bragg peak when detecting the dose. Thus the dose was adjusted by a factor F_1. The estimate for the stopping power dependence was arrived at using the ratio of the stopping powers in the corresponding layers - at the cell layer (layer we are interested in) and active layer of the film (layer where dose is measured). The energy at

the cell layer E_c was taken with the average energy in the cell layer and was calculated similarly for the active layer of the film's energy E_a. These energies were determined with SRIM [144] Monte Carlo transport simulations (see Figure 25) and their relevant stopping powers in water were calculated using both the electronic and nuclear stopping powers to yield the dose correction factor F_1:

$$F_1 = \frac{S_{E_c}}{S_{E_a}} = 0.76 \pm 0.02 \tag{17}$$

2. EBT2 film is known to under-respond at low energies. At the time of the experiment, this had not been calibrated yet for our system, so we took an estimate from the literature [69], correcting the dose by another factor F_2=0.9.

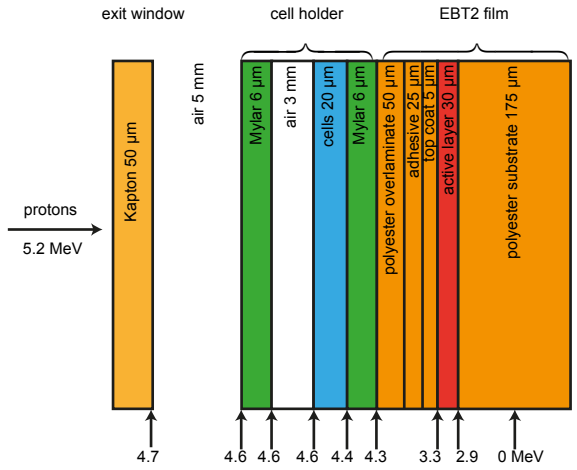

Figure 25: SRIM simulation of the energy loss throughout the layers in the delivery portion of the beamline. Some of the essential details of the simulation are given in Appendix A. Diagram is not drawn to scale.

The program to calculate the dose to the cells was initially obtained using the registered dose map described in the following section and a manually controlled rectangular ROI defined to be of the same size and rotation as the microscopic FOV. By moving such a ROI over the dose map according to the notes recorded during the microscopy session, all relevant dose information can be obtained such as mean dose, standard deviation, max dose, min dose and the coordinates of the region selected for dose calculation. Each ROI corresponds to the image recorded in the microscopy session, which is called a "box". The accuracy of the box placement was improved by taking advantage of the grid lines in the images, which were present in most but not all of the images, in which case the position required an educated guess.

Since the Mylar foil is manually positioned in the cell holder, the boxes appear slightly rotated due to some misalignment of the foil, obvious when looking at the grid. To compensate for this, the ROI was rotated by an angle θ when calculating the box dose.

2.2 IMAGE REGISTRATION

One of the key components in accurately determining the dose over a given microscopic image was through the use of image registration so that the inhomogeneous dose distribution could be fully exploited. Several registrations were involved in the entire process itself: registration of the markings image to the grid image provided by the manufacturer (see Figure 26); and grid registration to the film i. e. dosemap.

2.2.1 *Mark to Grid*

Beginning with the former of the two, these markings were simply drawn onto the film prior to irradiation, which was fixed onto the back of the Mylar foil in the cell holder. Photographs under the microscope were then taken of the markings, which showed the markings superimposed onto the grid on the foil. This is the reference point for the experimental conditions. Assuming no movement between the film and the grid on the foil, the result is a mapping from the experimental conditions to a high resolution image of the grid. These photographs were registered to the grid via scaling and rotation to coincide with the appropriate lines and coordinates on the grid image. This was performed on all 10 cell samples with 3 markings per sample. The precise placement of these markings was crucial to the second registration as these are the markings which map from grid to dosemap.

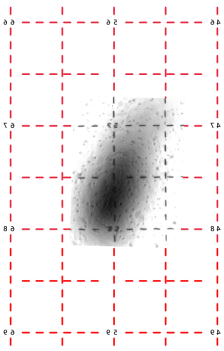

Figure 26: The black mark in the centre of the image is a scaled and rotated image taken under the microscope and registered to the grid. The grid lines have been modified to red so as to clearly distinguish between the two images. The grid intersects at intervals of 150 µm.

2.2.2 *Grid to Film*

The registered markings on the grid established in the previous step were registered to the actual markings drawn onto the radiochromic film. To clarify definitions, the dosemap is referred to as the *base* image and the grid as the *input* image. The selection of input and base input is extremely important as these definitions determine upon which image the transformation is applied in the registration procedure. As such, priority was given to the dosemap for complete data preservation. The problem in general follows a relatively straightforward outline for two bitmap images for whose control points are used to define a transformation matrix. This transformation matrix is applied to the input image after which the images are placed in a new coordinate system with the base image overlaying the transformed input image - see Figure 27. The details are presented below:

SCALING: The first problem encountered was to match the resolution of the film to the high resolution of the grid image. The grid needed to be high in resolution so that the coordinates and grid lines remained visible. As a result the film had to be blown up by a factor of μ to match the high resolution of the grid image. μ was calculated taking the ratio of film resolution, $r_{film} = 21$ µm to grid image resolution, $r_{grid} = 1.5$ µm $\therefore \mu = 14$.

CONTROL POINTS SELECTION: To create the transformation matrix, reference points needed to be selected in both images. These points are referred to as the *control points* and were determined visually. A minimum of three control points is required in order to construct the transformation matrix. The goal here is to select exactly the same spot *within* a pixel in both the input and base image. The relatively large size of the markings, however, only increased the difficulty in selecting the exact points in both images. Therefore a

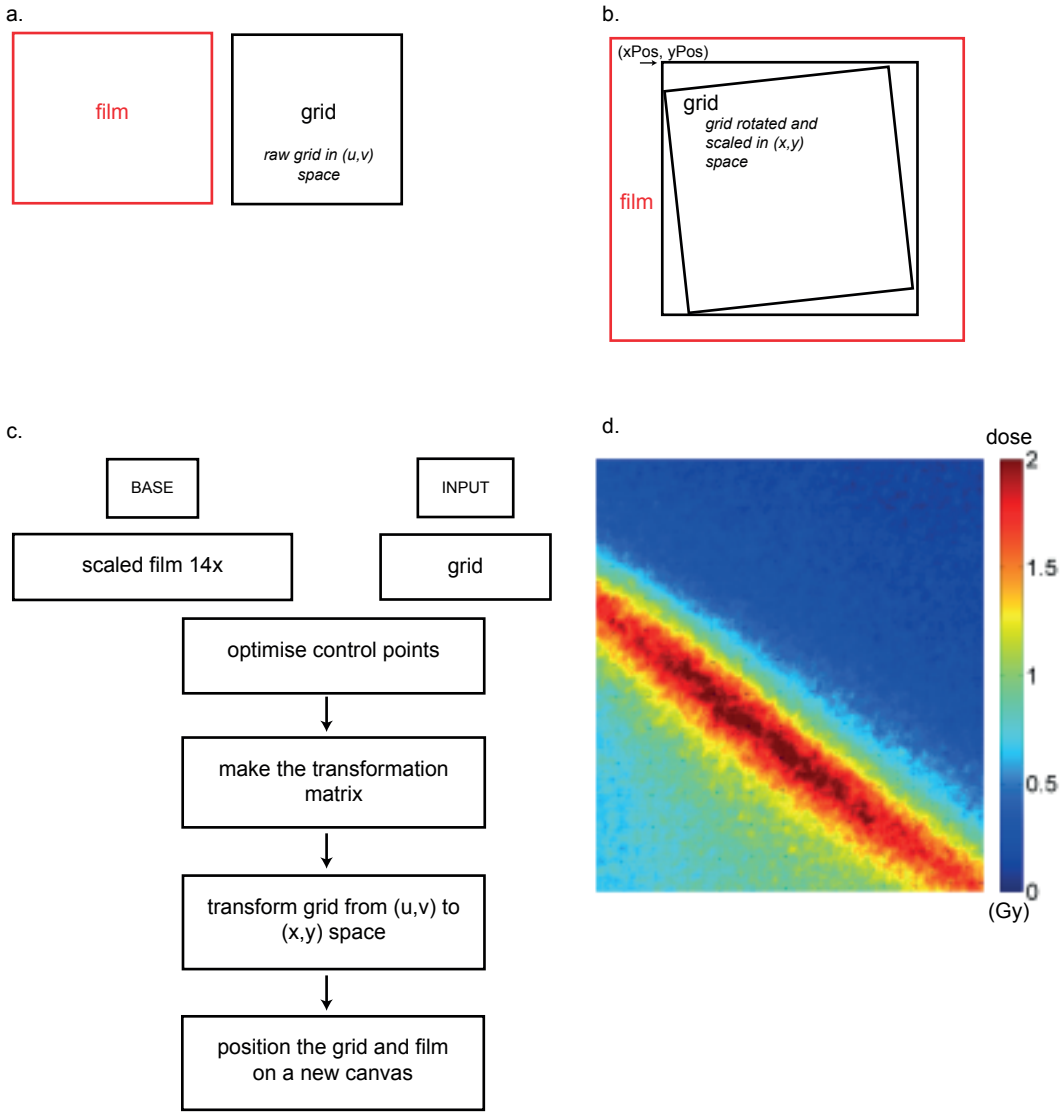

Figure 27: a. Original input and base images. **b.** Registered images in output space corresponding to the final image shown in d. **c.** The process of image registration using a transformation matrix constructed out of control points. **d.** Registered film to grid image for S10.

method was devised to ascertain the accuracy of control point selection. The process of control point selection is demonstrated in Figure 28.

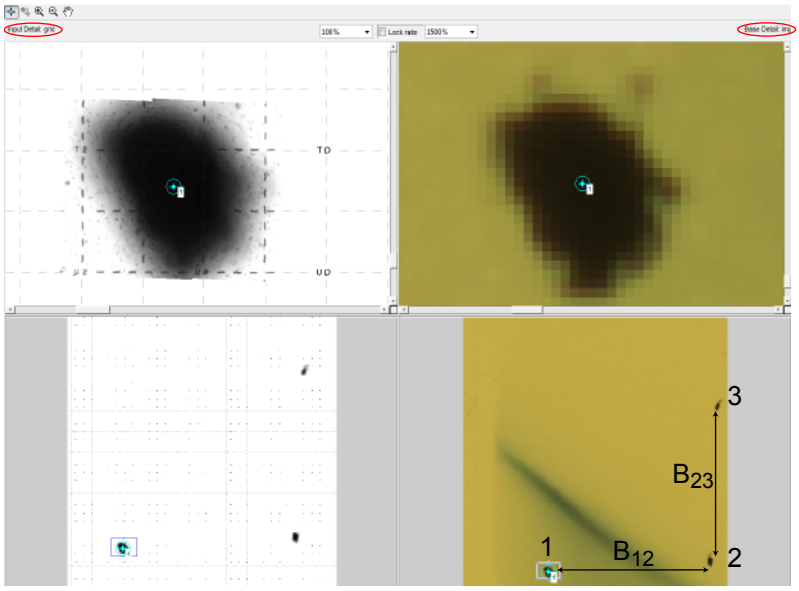

Figure 28: Upper quadrants show the zoomed portion of the input and base images. Where the input image on the left is the grid and the base image on the right is the film. The blue mark in both input and base image is one of three control points that must be in the same pixel in both images. All control points were chosen to coincide with the markings (point 1, 2 and 3) on the film, which make it easier to select the same pixel in both images.

Accurate selection of the control points was determined by minimising the difference in distance between all three points and comparing them to each other to ensure the control point selection was never inaccurate by more than one pixel. This was calculated using the following: Consider the point 1 (x_1, y_1) and point 2 (x_2, y_2) on the base image as shown in Figure 28. The distance between point 1 and point 2 is $B_{12} = \sqrt{(x_1 - x_2)^2 + (y_1 - y_2)^2}$ and the distance between point 2 and point 3 (x_3, y_3) is $B_{23} = \sqrt{(x_2 - x_3)^2 + (y_2 - y_3)^2}$. If the distance between points 1 and 2 is I_{12} and between points 2 and 3 is I_{23} in the input image, then the goal is now to have the error in control point selection P_{diff} as close to zero as possible.

$$
\begin{aligned}
I_{ratio} &= \frac{I_{12}}{I_{23}} \\
B_{ratio} &= \frac{B_{12}}{B_{23}} \\
P_{similarity} &= \frac{I_{ratio}}{B_{ratio}} \approx 1 \\
P_{diff} &= (1 - P_{similarity}) \cdot 100 \quad (\%)
\end{aligned}
\tag{18}
$$

The question then is: how close to zero should P_{diff} be? An acceptable accuracy was defined by ensuring the pixel offset never exceeded one pixel. Using P_{diff}, an error in terms of pixels was found by calibrating two identical film images so that both input and base images were the film. The idea here being that it is much simpler to pick the same pixel if both images are the same and by using known pixel offsets, a calibration curve as in Figure 29, can be established. This was performed by selecting a pixel at (x_1, y_1) in the input image and calculating P_{diff} when the pixel was 0, 1, 2 and 3 pixels offset in the north, east, south and west direction of the base image. Note that even for a 0 pixel offset i.e choosing the same pixel in both input and base image, it is impossible to achieve 0% difference between the two images. The reason for this being that the pixels in the film are big (due to the scaling) and the zoom capability is limited. The final

calibration curve is then the average of each pixel offset calculated in all four directions for all three points. The values are given in Appendix B.

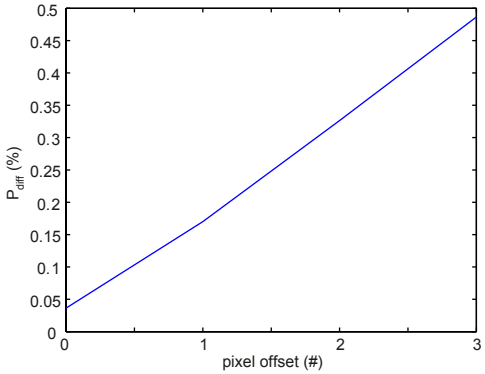

Figure 29: Error calibration of the control point selection process. The known pixel difference was used to calculate the difference between input and base image. Since this was performed on two identical images, the pixel offset could easily be controlled, which can be used when selecting points between film and grid so that the differences obtained can be used to determine a pixel offset of 1 - the inverse problem of the calibration. The pixel size here is that of the grid resolution i. e. 1.5 µm.

Thus when selecting control points for differing input and base images, the quantity P_{diff} provides a means of ensuring that the error in the grid to film registration σ_{GFR} is

$$\Delta_{GFR} = 1 \quad (px) \tag{19}$$

CREATE AND APPLY TRANSFORMATION MATRIX: Once the appropriate control points have been selected, a transformation matrix must be generated, which includes scaling, translation and rotation, where scaling could not be suppressed. Inclusion of any other parameters such as shearing or reflection resulted in a badly transformed grid. The goal of the transformation matrix is to provide a suitable mapping from the primary (u, v) space to the transformed space (x, y) so that the following equation must be solved for sc, ss, tx, and ty where

$$\begin{aligned} sc &= scale \cdot \cos(\alpha) \\ ss &= scale \cdot \sin(\alpha) \\ t_m &= translation \end{aligned}$$

then

$$(u, v) = (x, y, 1) \cdot \begin{pmatrix} sc & -ss \\ ss & sc \\ tx & ty \end{pmatrix}$$

Once the transformation matrix has been solved for, applying it to the grid generates the grid in the required form. The coordinates of the image in the output space $(xPos, yPos)$ are returned from the transformation and show where the transformed grid was placed in the output space. This is necessary when creating the final merged image.

CREATE FINAL IMAGE: The final image was created by putting the resized transformed image and base image in their aligned positions onto a new 'canvas'. The aligned position being such that the grid is placed at $(xPos, yPos)$ extracted from the previous step and the film at the canvas origin.

2.3 ANALYSING RADIATION-INDUCED DAMAGE

Although the cell survival assay is considered to be the standard in quantifying radiation-induced damage, because of the demands placed on recovery of precise spatial dose information, the γH2AX assay was chosen over other types of analysis. As mentioned in Part II

Chapter 1, the assay is based upon the large number of repair proteins recruited to the site of the DSB. Since antibodies are highly specific molecules, they are an ideal choice when it comes to viewing selective processes. Therefore by tagging an antibody with a fluorophore, DSBs can be imaged assuming the antibody singularly binds to the site of the DSB. This can then be viewed using confocal or widefield microscopy, appearing as a bright dot which is generally referred to as a focus.

In this experiment, cells were seeded onto all of the cell holders 24 hours prior to the first cell irradiation. Therefore the second day's cells had a much larger number of cells because they had an extra day to grow. 30 minutes following irradiation shows a maximum in foci production after which DSBs repair removes many of the induced foci [113]. Therefore the cells were fixed and stained with two antibodies 30 minutes after irradiation and the radiation-induced damage was assessed using the DSB markers γH2AX and 53BP1.

2.4 MICROSCOPY ANALYSIS

In order to exploit the full dose range, images were recorded over high and low dose regions of the line focus. This can be seen in Figure 24. Images were captured over a week, within two weeks after the time of irradiation in order to take advantage of the maximal signal strength. Images were recorded as z-stacks with at least 10 slices per stack at a distance of 0.25 μm between each slice. Since the registration was performed prior to microscopy, we were able to move to specific areas over the line focus in order to capture the complete dose response. The location of where an image was taken was recorded for later use in the widefield dosimetry.

3 RESULTS

3.1 WIDEFIELD RESULTS

Typically microscopy and dosimetry based on the γH2AX assay is conducted with widefield analysis. The results presented here will be divided into two sections: widefield analysis, which is based on the microscope images (box) i. e. over an area of 139×103 μm^2; followed by the single cell foci analysis (based on the method presented previously in Part II, Section 3.4) and single cell dosimetry, which was performed by Sarah Brueningk. The approximate diameter of a HeLa cell nucleus is 20 µm. To understand the way the results are divided, the data nomenclature and hierarchy is shown below in Figure 30.

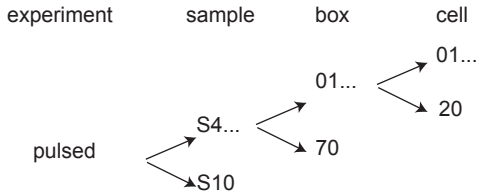

Figure 30: Data hierarchy with pulsed protons. The widefield approach stops at the box whereas the single cell approach continues one level further. Not shown are the permutations possible when green and red channels or 2D and 3D data are considered.

3.1.1 *Uncertainties in Registration*

Table 4 shows the dose results and the corresponding uncertainties generated on the second day of irradiation measured at the active layer of the *film*. However when calculating the RBE, the dose to the *cells* is required and is actually a little less according to F_1 (Equation 17). Here the maximum dose is tabulated to demonstrate the high dose generated within a single laser shot, however since this high dose could also just be one pixel, the average dose is actually somewhat lower.

The error in registration owing to the widefield method σ_W has four sources:

- Dose inhomogeneity in a box σ_I: The dose inhomogeneity is determined across all pixels n contributing to the mean dose $\bar{d}$ in a box.

$$\sigma_I = \sqrt{\frac{1}{n-1}\sum_{i=1}^{n}(d_i - \bar{d})^2} \cdot \frac{100}{\bar{d}} \quad (\%) \tag{20}$$

- Error from the pure registration σ_{reg} is comprised of three registration processes:
  - Mark to grid registration Δ_{MGR}: This was performed manually, however the error is estimated to be small - less than 1 px (1.5 µm).
  - Grid to film image registration Δ_{GFR}: Defined in Equation 19 and set to 1 px (1.5 µm).
  - Box to grid registration Δ_{BGR}: Since the dose box was placed manually, the error is estimated to be large - one pixel (film size pixel 21 µm) per box. A small contribution also comes from the rotation angle of the box θ i. e. Δ_θ with respect to the

grid since this was determined by hand, however it was not included in the error analysis.

σ_{reg} can be simplified by considering the following:

$$\sigma_{reg} = \sqrt{\Delta^2_{MGR} + \Delta^2_{GFR} + \Delta^2_{BGR}} \quad (px) \tag{21}$$

$$\Delta^2_{BGR} >> \Delta^2_{MGR} + \Delta^2_{GFR} \quad (px) \tag{22}$$

$$\sigma_{reg} \approx \Delta_{BGR} \quad (px) \tag{23}$$

σ_{reg} was calculated in terms of dose using the maximum deviation in dose d_{max} obtained from the vector of doses $\mathbf{d}_{vec}$ such that each element is the average dose when the box is translated by one film pixel or 14 grid pixels. If $\bar{d}$ is the mean dose in a box at position (x, y) i. e. $d(x, y)$ then

$$\begin{aligned} d_{east} &= d(x+1, y) \quad (Gy) \\ d_{south} &= d(x, y+1) \quad (Gy) \\ d_{west} &= d(x-1, y) \quad (Gy) \\ d_{north} &= d(x, y-1) \quad (Gy) \\ \mathbf{d}_{vec} &= \{d_{east}, d_{south}, d_{west}, d_{north}\} \\ d_{max} &= max(\mathbf{d}_{vec}) \end{aligned}$$

$$\sigma_{reg} = \frac{d_{max} - \bar{d}}{\bar{d}} \cdot 100 \quad (\%) \tag{24}$$

Therefore the final registration error in the widefield method per box is

$$\sigma_W = \sqrt{\sigma^2_{I_i} + \sigma^2_{reg_i}} \quad (\%) \tag{25}$$

Table 4: Dose information for each cell sample irradiation on day 2. $\bar{\sigma}_I$ is the average for all boxes in the corresponding sample according to Equation 20. $\bar{\sigma}_{reg}$ is the average registration error for all boxes in a cell sample, where the number of boxes per sample varied between 29 and 70. Each σ_{reg} is calculated according to Equation 24. Dose analysis corresponding to the microscopy session was not performed on S7 and S8, thus no standard deviation in dose could be calculated. S9 was eventually also discarded due to high noise levels for the foci detection.

CELL SAMPLE	MAX DOSE (GY)	$\bar{\sigma}_I$(%)	$\bar{\sigma}_{REG}$ (%)
S4	1.9	7	2.0
S5	0.8	7	2.1
S6	1.0	10	2.9
S7	9.3	NA	NA
S8	2.7	NA	NA
S9	1.6	6	NA
S10	2.3	6	2.5

3.1.2 *Dose Response Curve*

In the widefield analysis, the number foci per cell were determined based on the following principle: calculate the number of cells in a microscope image N and then calculate the number

of foci in a microscope image f. Therefore the number of foci per cell in an image is f/N. This was a semi-automated method using window/threshold techniques [146]. The methods of dosimetry applied have already been outlined, so that in order to generate the dose response curve, these two data sets were plotted against each other. The dose response curves shown in Figure 31 only include S10 as a widefield analysis translating to: microscope images, 2D data and both repair proteins i. e. γH2AX and 53BP1.

In order to calculate the RBE a dose response curve was generated comparing protons with reference 200 kV xrays. Cells were handled in the same way as in the laser experiment and microscopy was performed. Xrays were irradiated at finite dose levels to cover the same dose range as for S10 protons so that the dose points for the xrays were at 0, 0.5, 1, 1.5 and 2 Gy. From Figure 31 at an effect of 30 foci, the RBE was calculated to be 1.3±0.3 in both γH2AX and 53BP1 dose response curves. The error is calculated using Gaussian error propagation where, for the xrays, error is attributed to 10% from the fit dose response curve and 5% in absolute dosimetry. Whereas for protons, the error is attributed to 9% from the fit dose response curve, 4% from the registration (not taking the dose inhomogeneity into account) and 20% error was estimated in absolute dosimetry; the latter of which was explicitly measured in the following chapter.

3.2 SINGLE CELL ANALYSIS

Table 4 shows that the dose inhomogeneity across a microscope image is not negligible. Therefore in order to reduce this effect, cell dosimetry was conducted on a single cell basis rather than across the microscope FOV. The foci analysis was conducted using the method outlined in the previous Chapter 3.4, which through the contouring process, additionally returned information concerning the coordinates of the cells. These coordinates were used to determine the dose to the cell, which was later fused to the foci information previously calculated. Since the dose response curve of the pulsed protons on a single cell basis has been shown elsewhere, (Figure 18) the following section deals with the gains in accuracy when switching to the single cell method. A dose response curve necessary for RBE calculation with the single cell method, which might be comparable to Figure 31 could not be generated with this method due to poor image quality in the xray data. An alternative however will be presented in the proceeding chapter.

3.2.1 *Uncertainties in Registration*

In order to determine the dose to these individual cells, three coordinate transformations were applied.

1. Cell to Reference coordinate system Transformation (CRT): Here a reference position was determined as the centre of a grid line with respect to the box so that there was error in its estimation. In addition the grid line was rotated by some angle ϕ with respect to the box, which has some error, but is small compared to the position error.

2. Reference coordinate system to Grid Transformation (RGT): The coordinates of the reference position with respect to the grid were calculated. Since the coordinates are assumed to be of negligible error with respect to the position of the lines, there was no error in this step. However some images did not originally have the grid in view, thus an additional error was introduced in this step to register images with the grid present to those

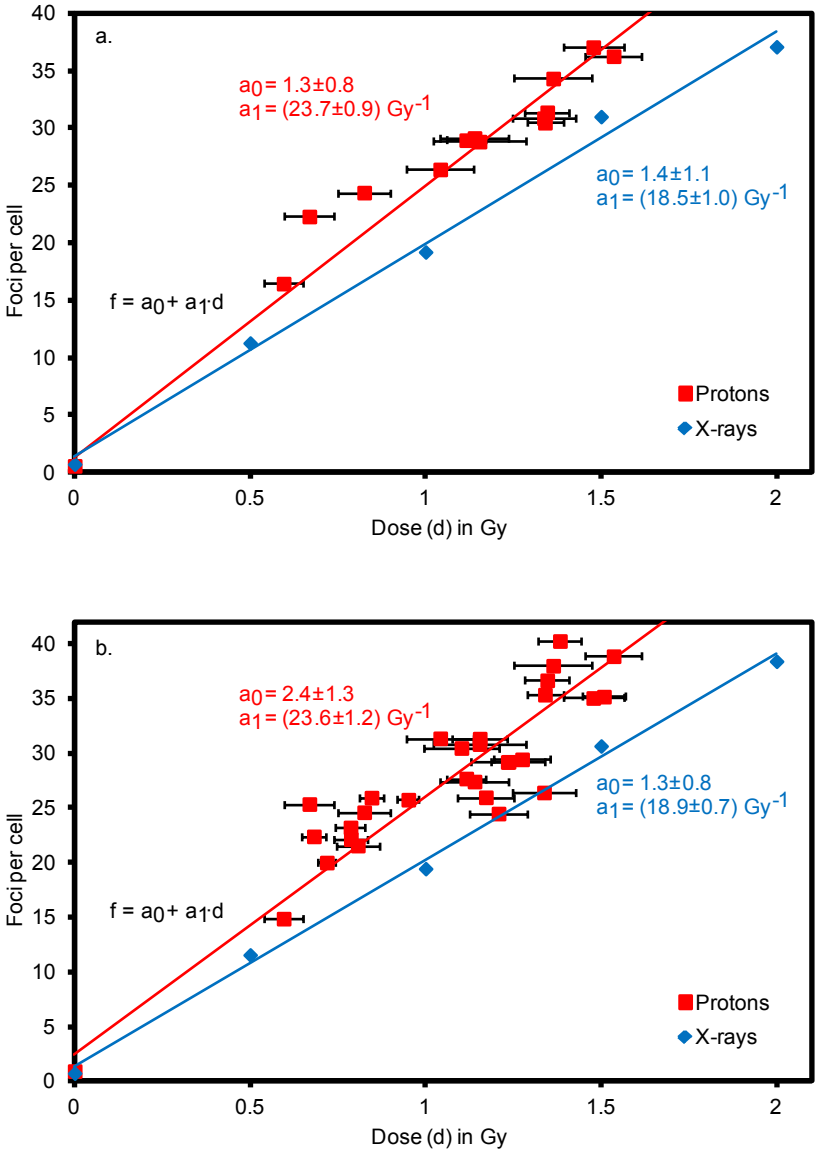

Figure 31: Dose response compiled with data from the S10 cell sample using the *widefield* method. Error bars in dose are given by the standard deviation across a microscope image. Foci were determined using a semi-automated method in ImageJ. **a.** γH2AX dose response. **b.** 532BP1 dose response. Note: There are fewer data points in the γH2AX dose response curve due to some problems with the Cy3 dye in the microscopy session.

originally without the grid. Therefore for these particular images (30% of the images), there was also an occasional additional registration error:

3. GFR: The final transformation required transforming the coordinates from the RGT to the registered dosemap obtained in Section 2.2.2. Thus the error in this registration was also included using Equation 19.

The errors were calculated in each of the following transformations and propagated to the next transformation in units of distance (μm). This was based on the transformations having the following form:

$$\begin{pmatrix} x' \\ y' \end{pmatrix} = \begin{pmatrix} \cos\phi & -\sin\phi \\ \sin\phi & +\cos\phi \end{pmatrix} \begin{pmatrix} x \\ y \end{pmatrix} + \begin{pmatrix} r \\ t \end{pmatrix}$$

where (x, y) are the coordinates of the points to be transformed from one coordinate system to another (x', y'). Translation is given by (r, t) and for the last step when scaling was introduced, an error in scaling μ was included. The error in each transformation, was propagated into the next using:

$$\Delta f = \sum_i \left(\frac{\partial f}{\partial x_i}\right)^2 \cdot \Delta x_i^2 \tag{26}$$

$$\begin{aligned} \Delta x'^2 &= \mu^2 \cos^2\phi \cdot \Delta x^2 + \mu^2 \sin^2\phi \cdot \Delta y^2 + \Delta r^2 \\ &\quad + x^2\mu^2 \sin^2\phi \cdot \Delta\phi^2 + y^2\mu^2 \cos^2\phi \cdot \Delta\phi^2 \qquad (27) \\ &\quad + x^2 \cos^2\phi \cdot \Delta\mu^2 + y^2 \sin^2\phi \cdot \Delta\mu^2 \qquad (28) \end{aligned}$$

This was calculated similarly for $\Delta y'^2$ so that the final error in the single cell method σ_s per cell was converted into pixels and then into dose. σ_s was converted into units of pixel offset and determined by expanding the region by the pixel offset in all directions to find the maximum dose (d_{maxPx}) within the newly defined region. The error is thus the difference between the maximum dose and mean dose within the expanded borders. The results of these transformations were then used to determine the cell dosimetry and were performed with S4, S5, S6 and S10, where S9 was discarded due to high noise and thus poor foci discrimination. The difference between the widefield and single cell dosimetry is presented below where the difference between widefield dose d_w and single cell dose d_s is given by:

$$\Delta d = \frac{d_s - d_w}{d_w} \cdot 100 \quad (\%)$$

The distribution of the differences between widefield and single cell dosimetry are displayed in Figure 32. Here the broad distribution of inhomogeneity in a dose box can be seen for all cell samples with the majority being within ±10% of the average dose value calculated with the widefield method. In Figure 32a, the difference between the widefield method and single cell method can be seen to mainly lie within 10% of the original dose estimate d_w. Figure 32b., confirms this since the Δd is still centred within this region, however the line structures now show the amount of dose change across a FOV since each point represents the difference in dose between the single cell method and widefield method per cell.

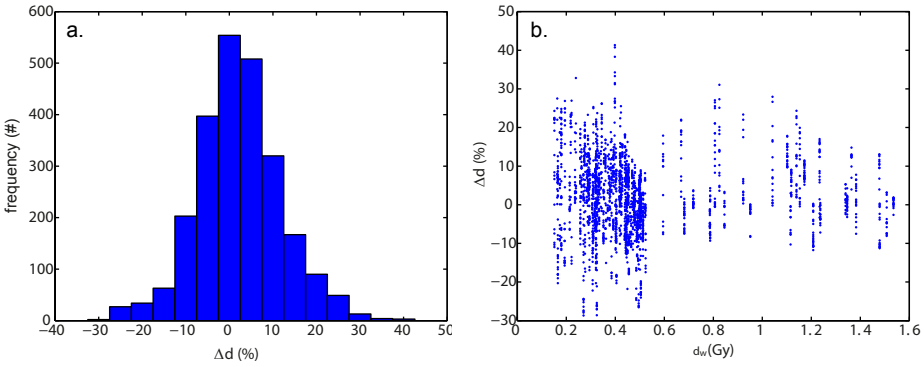

Figure 32: a. Distribution of the difference in widefield dose and cell dose for all cell samples (S4, S5, S6, S10). **b.** Difference between widefield and cell dose as a function of the cell dose for all cell samples.

3.2.2 *Accuracy Gained*

The worst case scenario errors associated with both the widefield (Equation 25) and single cell method (Equation 28) are compared in Table 5 to demonstrate the improvement in accuracy when switching to the single cell analysis. The errors from the single cell dosimetry come from three coordinate transformations rather than the two transformations in the widefield method and the dose inhomogeneity, which had the largest contribution.

Table 5: Comparison between the mean dose error in widefield and single cell analysis by taking the largest error from all error sources. The max σ_W is from σ_I and the max σ_{reg} using Equation 25. The max single cell error σ_S has been similarly produced from its own sources of error.

CELL SAMPLE	MAX σ_I (%)	MAX σ_{REG} (%)	MAX σ_W (%)	MAX σ_S(%)
S4	13	6.1	14	4
S5	13	5.0	14	6
S6	17	6.5	18	5
S10	11	5.4	12	3

4 DISCUSSION

The primary goal of this part was to determine the RBE of laser-driven protons to ensure their biological safety for clinical use so that no unexpected clinical outcomes should result. Here, based on the widefield analysis with just the S10 cell sample, the RBE was calculated as 1.3±0.3 for both γH2AX and 53BP1 DSB repair proteins. Although the single cell method can significantly reduce the uncertainty in dose-foci determination, an analogous RBE could not be produced with such a method since the xray data had poor deconvolution results and using the raw image had a much too poor signal to background ratio. This result, however, is within current expectations for monoenergetic, low energy protons. Furthermore, other groups have achieved similar results with laser-driven proton cell irradiations [139][71][138][35], adding to the general body of evidence that no biological difference exists between laser-driven protons and conventionally-produced protons. The results from Doria et al. correlate especially well with the findings presented here since the dose delivered to the cells was also given in a single shot [35]. This methodology differs somewhat to Kraft et al. [71] and Yogo et al. [138], who achieved comparable dose levels to ours though over multiple shots due to the low dose delivered per shot. Therefore total time to achieve 1 Gy is dependent upon shot frequency so that in the end, the dose delivery time differs little compared to conventional protons; in contrast to the results shown here where it was over nanoseconds.

A secondary aim of this part was to optimise the setup for a low proton energy cell irradiation using laser-driven protons. This highlights another difference in the results shown here to those from Kraft et al., Yogo et al. and Doria et al., since all are based on a magnetic chicane [76] to control the wide energy spread resulting from the TNSA process, whereas here miniquadrupoles were used. Nevertheless an inhomogeneous dose still needs to be dealt with and very much influences the accuracy of the biological analysis. The cell survival assay [97] is strongly preferred and all groups have approached this problem differently. Yogo et al. used the cell survival assay but rotated the sample halfway through the dose delivery to improve dose homogeneity. A similar technique was performed by Kraft et al., though with the γH2AX assay. Our group makes use of a film to cell registration through the use of a grid and the γH2AX assay, whereas Doria et al. also implemented a kind of registration with the cell survival assay. This again shows the comparability between our results and those from Doria et al.

UNEXPECTED FINDINGS: In the RBE calculation concerning the protons, error came from the fit line curve, registration and absolute dosimetry. Using the widefield method, the absolute dose uncertainty was estimated to be 20%, attributed to our estimate of the low energy under-response in EBT2 film. Registration errors were estimated to be 4% and were due to GFR, MGR and BGR registrations, the latter of which was performed manually. Comparing the widefield method with the single cell method, the GFR uncertainty remains, though this is very small compared to the manual BGR registration performed in the widefield method. The GFR registration is small because although both GFR and BGR registrations have an error of 1 pixel, the pixel size differs by 14 times between grid resolution and film resolution thereby making the GFR error negligible.

Therefore using the single cell method we were able to significantly reduce the registration error via an improvement in the BGR 2% registration, as well as eliminate the even larger average 7% or so dose inhomogeneity. Taking the worst possible scenario to compare the widefield method to the single cell method, the error can be more than halved by switching to the single cell method. The final error in this method might be improved upon by having higher resolved dosimetry systems.

As mentioned, the absolute dosimetry error was a generous estimate concerning our estimate of the low energy dose response in EBT2 film. Thus we decided to measure this for ourselves; this was investigated in the following experiment with continuous protons (Part IV). This new calibration was used for the data presented here and in the the previous chapter in Figure 18..

LIMITATIONS: The accuracy of this analysis is mainly dependent upon the registration in the dosimetry analysis and the error in the foci analysis. In the widefield method of foci analysis it is difficult to give a concrete error estimate owing to the subjective nature of the analysis, so that the number of foci counted on one day would not necessarily be the same the following day. This (along with the dose inhomogeneity) was a leading reason to perform the single cell analysis using the FociPicker_3D program with the automated method outlined previously. Therefore the single cell analysis reduces the error in foci inhomogeneity as well as the user-related error associated with widefield analysis. The obvious limitation here being in the FociPicker_3D program being able to accurately define a focus, something that is already difficult to define manually. Therefore the errors in the foci number represent the uncertainty in the program, which is shown as the standard deviation of foci.

In hindsight, there are a significant number of things that would have been done differently in this experiment had we had the chance to repeat it. On the automation side, the way the data was recorded exceedingly added to the complications of the large data analysis. Though it may seem obvious now, small things such as choosing a sensible, consistent name across all irradiated samples and all microscopic photographs would have simplified the programming complexity necessary to structurally organise and analyse so much data.

On the biological side, cells should ideally be seeded onto the cell holder 24 hours prior to irradiation, however due to the unpredictable nature of the laser, the irradiation was conducted over two nights. As a result, S4-S10 cells had double the time to divide so that many more cells were in the day 2 samples than the day 1 samples. Consequently the cells were probably under stress, which again influences our results. Accuracy in the foci number might be improved if the state of the cell cycle is known, since varying states of the cell cycle show varying degrees of radiosensitivity [92]. This problem however was not accounted for in the other cell irradiation studies and may even be superfluous when considering that this is difficult to control in a clinical setting if such technology were eventually to be implemented.

Furthermore the Cy3 dye, which was used to mark the γH2AX protein showed very poor signal throughout the microscopy session, so that in many cases, no images could be taken. Since the γH2AX protein is the most important, this resulted in a significant data reduction. And, although 10 samples were irradiated, a significant number were excluded for the following reasons:

- S1, S2, S3: due to low average dose.
- S7: dose outside of the useful range of γH2AX assay.
- S8: photobleached cells so that microscopy could not be performed.

- S9: poor signal to background ratio, which did not allow effective use of the FociPicker_3D program.

Therefore ~40% of the data was lost, accounting for the fact that less cells were in the day 1 samples, but half of the data that was kept had missing data from the red channel. Fortunately the absolute volume of data nevertheless remained high, which is evident in the consistent linear relationship in the dose response curves.

IMPLICATIONS FOR FUTURE RESEARCH: Although the final goal of these preliminary experiments is the clinical implementation of a cheap, compact source of protons, not all of the features considered here would necessarily be of use in the final application; a few of these will be discussed here at length. Concerning the setup optimisation, much effort here has gone into preserving the Bragg peak as best as possible in comparison to that seen from conventional sources. However there is reason to believe that this might actually be a redundant act, since ion therapy always involves spreading out the dose distribution, which is essentially what has already been produced here. Reasonable programs have been written to demonstrate the feasibility of using the beam more or less as it is and ostensibly demonstrate a reasonable treatment plan under such conditions [110] [61]. Therefore the use of mini-quadrupole magnets in our setup will perhaps not feature in future experiments, which would involve mice models and so possibly require the pre-generated energy spread that is a natural feature of the laser. On the other hand, this poses a new set of problems for the dosimetry. Not to mention the massive advances required in laser technology before the energy would be adequate enough to irradiate a solid mouse tumour in which case the energy needs to be more than double what it is now.

Concerning the methods used here for future similarly-designed experiments with regards to improvements in image quality, photobleaching might be better addressed. The mechanisms involved in photobleaching are thought to be due to photo-oxidation (described in section 1.5) and (less prominently perhaps) photo-ionisation [132]. Based on these supposed photobleaching mechanisms, approaches to decrease photobleaching include deoxygenation, adding antioxidants, oxygen scavengers, singlet oxygen quenchers or triplet state quenchers [132]. Many of these tend to retard the photobleaching process but do not increase the amount of fluorescence. Furthermore depending upon which process dominates, the success of implementation of these strategies can be altered, which are further affected by environmental conditions and may even vary from molecule to molecule. Therefore although these approaches *may* be successful, it may actually be better to simply avoid the immediate area that has been stimulated by the laser as we were forced to do. Alternatively simply decreasing the laser intensity during excitation would significantly help photobleaching. Consequently high-speed pulsed laser light at lower intensities has been suggested as a mechanism to avoid the photobleaching rather than retard it [65].

Finally the accuracy of the image registration (GFR) might be improved upon if the marks drawn onto the film were smaller in size thereby reducing the pool of possible pixels common to both input and base image upon which the registration is dependent. A possible substitution might be a pin prick in the film, which would distinguish itself by being brighter than its surroundings or even a very small point drawn by a fine marker.

With regards to the pulsed nature of the dose delivery, although we were able here to truly deliver nanosecond pulses to living cells and investigate the effects, it is questionable whether this would have much meaning in the clinic. In all likelihood single fractions of treatment would require more than one shot to achieve adequate tumour coverage and toxicity. Indeed this is the case for conventional photon and proton treatment today. Such a fact, however, is

highlighted in our experiment, firstly because it sets an unprecedented efficiency in the number of protons that can be delivered despite still being in the TNSA regime, and secondly that precisely because of the high dose and inhomogeneity, we were able to investigate the timescale properties of radiation-induced DSBs. Thus what has been tested here is an extreme case of the maximum occurring difference between continuous and pulsed protons, which nevertheless showed no biological differences within the current error range. Consequently it is reassuring to know (though not biologically exciting) that when/if laser-driven protons were to be clinically implemented, it would not be necessary to make any biological adjustments in the context of treatment planning optimisation.

Part IV

CELL EXPERIMENTS WITH TANDEM ACCELERATOR CONTINUOUS PROTONS

1

MOTIVATION

In order to make a biological assessment of laser-driven protons with the utmost precision, an experiment was devised to replicate all conditions except for the time over which the dose was delivered. This means that in the newly devised experiment, the same proton energy, energy spread and biological conditions were maintained to examine the nature of pulsed delivery (as in the laser experiment) in comparison to continuous delivery (tandem accelerator). As previously mentioned, the pulsed proton dose was delivered over the order of nanoseconds, whereas the continuous proton dose is delivered over the order of milliseconds. The goal here was to quantify and compare the dose required to induce the same biological effect in pulsed and continuous protons, where the continuous protons are used as the reference radiation. The analysis is performed using the γH2AX assay as carried out previously in the laser experiment in terms of the number of foci/Gy cell as well as for the respective sizes of the foci, which is measured in both 2D and 3D.

A parallel aim to this chapter was to quantify the under-response of the radiochromic EBT2 film. For clinical purposes EBT2 film is energy independent, has high spatial resolution and is self-developing [7], thereby making it a natural choice for use in radiation therapy dosimetry. Crucially for the pulsed proton experiment, there is a limit to the energy independence, which, for EBT2 should ideally be measured. Following the dosimetry results obtained with the low energy protons produced by the laser, it was apparent that owing to the approximate correction factor deduced from the literature, there was significant room for an improvement in accuracy. Whereas previously a correction factor of $F_2 = 0.9$ was applied to the dose to take the under-response into account, here the film is explicitly calibrated.

Because of the well-known dose underestimation produced by EBT2 film at low energies, it was decided that this effect should be measured under comparable conditions to what was produced with the laser but with a controlled beam energy and dose. Therefore we turned to a more traditional method of proton production: the tandem accelerator. The principle idea being that the energy would be high enough to produce dose in the film's energy independent regime but by using a series of beam degraders, the low energy dependence could be measured in a second film downstream of the initial, stable film dose, which is used as the reference film.

1.1 SETUP

The *Maier Leibnitz Labor* tandem accelerator has several beamlines, however the one used in this experiment was the Supraleitendes Nanoskop für Angewandte Kernphysikalische Experimente/superconducting nanoprobe for applied nuclear physics experiments (SNAKE), which is capable of sub-micrometre resolution [60] in pulses as short as nanoseconds [34]. For the experiment here, however, a continuous beam (10^{-3} s) was delivered to be compared to the pulsed beam from the laser.

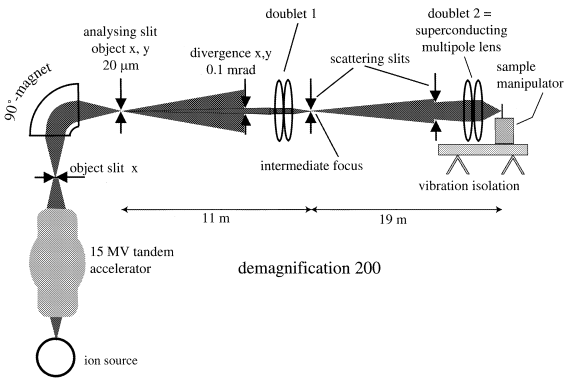

Figure 33: Schematic of SNAKE taken from [31] on the 0° beamline at the tandem accelerator. The negative ion source supplies ions, which, after being accelerated halfway through the tandem accelerator, undergo charge stripping to become positive ions. The 90° bending magnet ensures only the appropriate energies are selected. The SNAKE beamline is a two component demagnification system, comprised of a quadrupole doublet (doublet 1) followed by a superconducting multipole lens (doublet 2), which does the majority of the focusing. Together, the doublets result in a demagnification of 200.

1.2 CELL IRRADIATION EXPERIMENT

The main goal in the cell irradiation was to have the cells irradiated over a comparatively long time scale with a similar energy produced by the laser to compare the biological effect between proton types. To achieve the same energy in the cell layer and active layer of the film as was delivered in the pulsed proton experiment, simulations were performed with SRIM. A variety of configurations were tested so that the energy and the energy spread delivered to the cells by the tandem accelerator would be as close to 4.6±0.23 MeV as possible. The energy spread was taken from the spread in entrance energy ($\sigma_{\text{entrance}} = 0.23$ MeV)[1] produced by the laser and the standard deviation in energy of the traced particles at the cell layer ($\sigma_{\text{cell}} = 0.03$ MeV) from an SRIM simulation.

The final configuration involved two energy degraders (aluminium sheets 2 x 200 µm) and a film dosimeter (film 1), which also acted as an energy degrader and can be seen in Figure 34.

1.3 FILM CALIBRATION EXPERIMENT

For the film calibration, the setup was nearly identical except for an additional film (film 2) placed immediately behind the cell holder. In this case, since the cells were not required, the cell holder needed only to be filled with water. The film was oriented with the active layer upstream i. e. facing the beam.

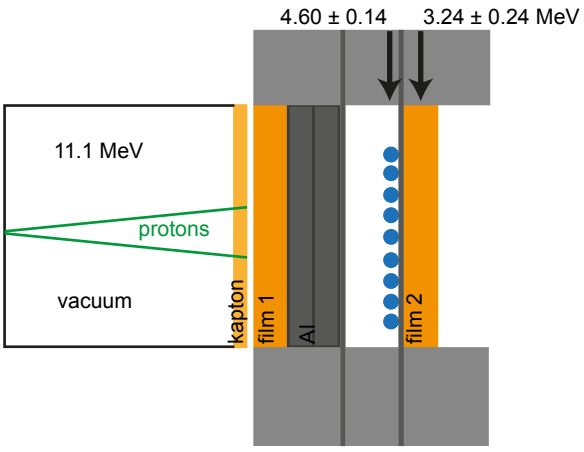

Figure 34: Experimental setup for continuous proton irradiation. Film 2 was only in place for the film calibration to reproduce the low energy spectrum from the laser from which the low energy calibration was established. Film 1 was present for both the cell irradiation and the film calibration; functioning as both a reference dosimeter and energy degrader. The cell monolayer was not required in the film calibration, however water was substituted instead.

1 Data according to a Monte Carlo simulation by Jörg Schreiber.

2

METHODS

2.1 CELL IRRADIATION EXPERIMENT

The experiment was designed to have three different cell samples irradiated at four different dose points each: 0.5, 1, 1.5, 2 Gy; bringing the total number of films irradiated to 12. Although higher doses were imparted with the ATLAS laser, the γH2AX assay is best used within the range of 0.1-2 Gy, which limited the pulsed proton analysis to the current dose range. Consequently this study was limited to a similar range.

As with the pulsed proton irradiation, HeLa cells were seeded onto the cell holder 48 hours prior to irradiation. γH2AX foci were recorded using the Cy3 dye and 53BP1 repair foci were stained with Alexa488. Microscopy was performed under similar conditions as in the laser-driven proton experiment - within 2 weeks of irradiation, images collected as z-stacks, minimum 100 cells per dose point. The number of foci/Gy cell was evaluated with the single cell method outlined in Part II, Chapter 3.4, which also returns information concerning the size of each focus detected.

The experiment was designed for fixed dose points to the cells, using the fluence values Φ_E in Table 6, which shows the preparatory values for the experiment. From Φ_E, an expected dose D_{Film1_E} was calculated as being delivered to film 1. Thus using the expected doses in film 1, a measure of how accurate the fluence delivery was can be assessed by comparing it with the experimentally measured dose D_{Film1_M}. The dose was measured using the 6 MV photon calibration curve and assumes a homogeneous dose delivery by the beam from:

$$\text{netOD} = \log_{10}\frac{I_0}{I} \tag{29}$$

$$D = a \cdot \text{netOD} + b \cdot \text{netOD}^c \tag{30}$$

where the curve has been fit using the parameters $a = (10.44 \pm 0.30)$ Gy, $b = (59.53 \pm 3.61)$ Gy, and $c = 2.8$. An intended field size of 3.7 mm^2 was used for all dose points. Due to lateral scattering of the beam however, as the particles pass through each successive layer, there was some dose inhomogeneity along the periphery of the irradiated area. To account for this the dose was evaluated over an inner area of 2.2 mm^2 where each dose square is slightly rotated. To calculate the dose, the dose square was manually positioned in the middle of the irradiated area.

2.2 FILM CALIBRATION EXPERIMENT

For the EBT2 film calibration experiment six different dose points were used: 0.4, 0.6, 1, 1.5, 2, and 4 Gy, where 0.4 Gy was the minimum stable dose achievable with the SNAKE beamline. In comparison to the last experiment, an additional piece of film was mounted behind the cell holder, which is referred to as film 2. The respective fluence for each dose point is calculated in Table 6. The expected doses for each dose point are again calculated from Φ_E.

The required fluences were calculated assuming dose to water at the corresponding energies simulated for the traversed layer. Thus the mass stopping power S at energies of 10.6 and

Table 6: Expected fluences Φ_E to be delivered with the SNAKE beam alongside the corresponding expected doses necessary for the cell experiment (with 4 dose points) followed by the film experiment (with 6 dose points). The dose to cells is the reference point from which Φ_E is calculated using Equation 2. Using Φ_E, the expected dose to film 1 D_{Film1_E} and film 2 D_{Film2_E} were derived. Expected fluences and doses are calculated assuming the energy delivered to be E_{cells}=4.6, E_{Film1}=10.6, E_{Film2}=3.2 MeV in the middle of the respective layer. Cell doses with an asterisk(*) were not used in the cell irradiation.

D_{CELL} (Gy)	$\Phi_E \cdot 10^7$ (p/cm^2)	D_{FILM1_E} (Gy)	D_{FILM2_E} (Gy)
0.4*	2.96	0.21	0.54
0.5	3.70	0.26	0.68
0.6*	4.44	0.31	0.81
1	7.40	0.52	1.35
1.5	11.09	0.78	2.03
2	14.79	1.04	2.71
4*	29.58	2.07	5.42

3.2 MeV was used to calculate dose. Normally at the SNAKE beamline, the required dose is delivered using the readings from the photomultiplier tube coupled to a scintillator in the beam path downstream of the cells [52], however this was not possible in this part of the experiment since the starting energy was so low and would not penetrate the final film layer in film 2. Thus the fluence was delivered utilising count rate rather than signal from the photomultiplier tube. This assumes that the number of protons is proportional to the count rate and therefore introduces the most significant source of error, which was estimated at the time to be 10%.

DETERMINING THE FILM UNDER-RESPONSE To determine the under-response of the film, the dose to film 1 is assumed to be the reference whose dose is calculated using the calibration curve obtained from 6 MV photons as in Equation 30. According to this reasoning then a negligible difference is assumed to exist between the calibration of 10.6 MeV protons and 6 MV photons when detecting dose via the net OD. From the dose measured in film 1, D_{Film1_M}, a calculated dose to film 2, D_{Film2_C} can be obtained via the calculated fluence, Φ_C:

$$\begin{aligned} \Phi_C &= \frac{D_{Film1_M}}{S_{10.6}} \\ D_{Film2_C} &= \Phi_C \cdot S_{3.2} \end{aligned} \tag{31}$$

where $S_{10.6}$ is the mass stopping power of protons in water at an energy of 10.6 MeV. Similarly $S_{3.2}$ is the mass stopping power of protons in water at an energy of 3.2 MeV. For each dose point one film was irradiated using four beam spots except for the 0.6 Gy dose level, since this was the most fluctuating in terms of stability, the film was irradiated with six dose areas. The field size of the irradiated area was again intended to be 3.7 mm^2. Dose regions were evaluated again as in the cell irradiation i. e. rotated ROI with area 2.2 mm^2 and manually positioned.

3.1 CELLULAR RESPONSE WITH LOW-ENERGY CONTINUOUS PROTONS

3.1.1 *Dosimetry*

The fundamental assumption in this method of dosimetry is that the clinic calibration with 6 MV photons is applicable to 10.6 MeV protons. Here the net optical density (net OD) of the film was used to calculate the measured film dose ($D_{Film_{1M}}$) according to Equation 30 where the background pixel intensity I_0 was taken as the average of the non-irradiated control films that were placed beside the irradiated samples during time of irradiation. A sample film and its corresponding dosemap according is shown in Figure 35. The doses measured in film 1 are shown in Table 7 and are compared to the expected doses calculated from the fluences in Table 6. This demonstrates a systematic error between the measured dose and delivered dose expressed as $cell\Delta_{M/E}$. The average discrepancy, $cell\bar{\Delta}_{M/E}$ was found to be -8%, which is explained by a 5% error in fit uncertainty of the 6 MV calibration and 3% uncertainty in batch to batch variation of films. Therefore this places a lower limit on the accuracy that can be achieved using EBT2 film.

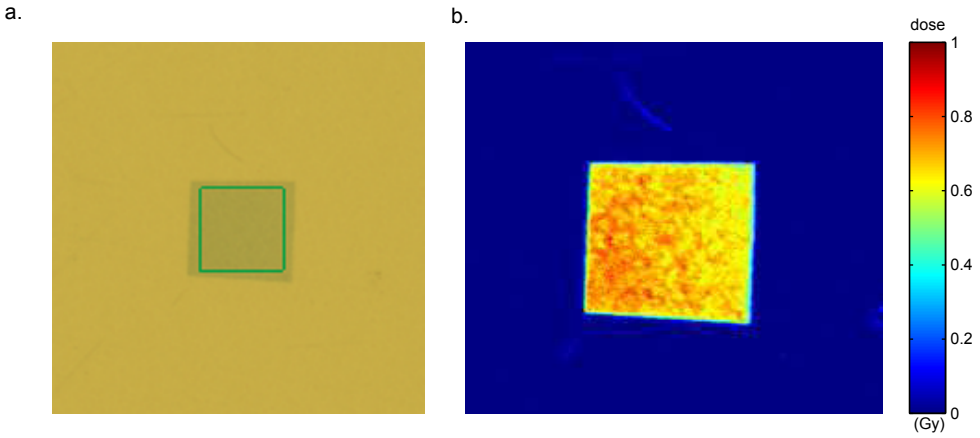

Figure 35: a. Raw image of an irradiated film during the cell irradiation showing the ROI in green over which the dose was taken. **b.** Corresponding dosemap to the irradiated film.

3.1.2 *The Relative Effect (biological)*

To make a fair assessment of the biological damage induced by laser-driven protons, the protons produced at the tandem accelerator were compared directly against the laser-driven protons for the same biological effect defined as the relative effect RE:

$$RE = \left.\frac{D_{cont}}{D_{pulsed}}\right|_{20\ foci} \tag{32}$$

Table 7: Film 1 measured film doses in the cell irradiation calculated from net OD and the 6 MV photon film calibration data listed in Equation 30. The difference between the measured dose using the 6 MV calibration and the expected dose according to the preparatory fluences shown in Table 6 is given as $cell\Delta_{M/E}$ as a percentage. The mean difference between the expected and measured dose in film 1 was calculated as $cell\bar{\Delta}_{M/E} = -8\%$.

D_{CELL} (Gy)	CELL D_{FILM1_E} (Gy)	CELL D_{FILM1_M} (Gy)	CELL $\Delta_{M/E}$ (%)
0.5	0.26	0.23	-10
		0.24	-6
		0.24	-6
1	0.52	0.45	-13
		0.46	-12
		0.50	-5
1.5	0.78	0.70	-10
		0.70	-10
		0.71	-9
2	1.04	0.97	-7
		0.98	-6
		0.98	-6

where D_{cont} is the dose required to induce 20 foci in the continuous proton data and D_{pulsed} is the dose required to induce 20 foci in the pulsed proton data given in Gy. The dose response curves used were those produced from the complete data set where dose >1.5 Gy in the 53BP1 channel was not included in the fit. The pulsed and continuous data have been plotted together in Figure 36 and is plotted using fit lines according to: $f = a_1 \cdot D + a_2$ as shown previously in Equation 16. The results for the relative effect using Equation 32 are given in Table 8, which summarise those shown in Figure 36. The data here shows the amount of information that is lost when drawing biological conclusions from 2D data rather than 3D since Table 8 shows the 2D RE to be consistently lower for both repair proteins in comparison to 3D.

Table 8: The Relative Effect for protons measured at 20 DSBs with 2D maximum intensity projected images and 3D image stacks calculated using the fit lines shown in Figure 36.

	γH2AX	53BP1
2D RE	0.8±0.1	1.1±0.2
3D RE	1.3±0.2	1.9± 0.3

The error in the RE was obtained using:

- Continuous error = fitted dose response (4-5%) for the 2D case and (6%) for the 3D case; absolute film dosimetry (10% see Section 3.2).
- Pulsed error = image registration (6% see Table 5); fitted dose response (5-7%) for 53BP1 and γH2AX respectively in the 2D case or (11-12%) in the 3D case; absolute film dosimetry (10% see Section 3.2).

The error was then calculated using error propagation and the largest error was always taken for the fitted dose response per channel; a channel being either γH2AX or 53BP1. Since the

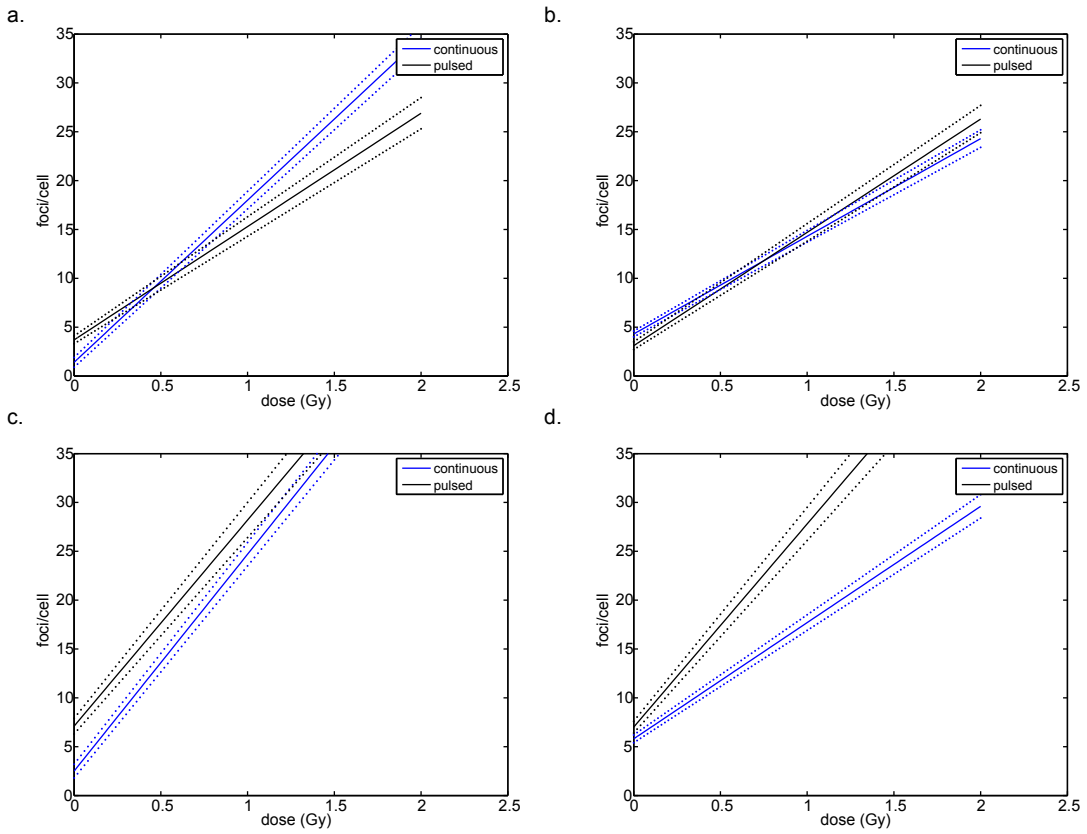

Figure 36: The dose response curves of continuous and pulsed protons using the maximum intensity projected images (a-b) and the 3D stack images (c-d) where the data has been compiled for each individual cell i. e. no binning. Fit parameters are given for each data set of the form shown in Equation 16. **a.** γH2AX 2D dose response using $\alpha 1 = (16.6 \pm 0.4)\ \mathrm{Gy}^{-1}$ and $\alpha 2 = (1.4 \pm 0.5)$ for continuous protons; $\alpha 1 = (11.6 \pm 0.6)\ \mathrm{Gy}^{-1}$ and $\alpha 2 = (3.7 \pm 0.4)$ for pulsed protons.
b. 53BP1 2D dose response using $\alpha 1 = (10.0 \pm 0.3)\ \mathrm{Gy}^{-1}$ and $\alpha 2 = (4.3 \pm 0.3)$ for continuous protons; $\alpha 1 = (11.6 \pm 0.5)\ \mathrm{Gy}^{-1}$ and $\alpha 2 = (3.1 \pm 0.4)$ for pulsed protons.
c. γH2AX 3D dose response using $\alpha 1 = (22.2 \pm 0.6)\ \mathrm{Gy}^{-1}$ and $\alpha 2 = (2.5 \pm 0.8)$ for continuous protons; $\alpha 1 = (21.0 \pm 1.0)\ \mathrm{Gy}^{-1}$ $\alpha 2 = (7.0 \pm 0.8)$ for pulsed protons.
d. 53BP1 3D dose response using $\alpha 1 = (11.9 \pm 0.4)\ \mathrm{Gy}^{-1}$ and $\alpha 2 = (5.8 \pm 0.4)$ for continuous protons; $\alpha 1 = (20.8 \pm 1.1)\ \mathrm{Gy}^{-1}$ and $\alpha 2 = (4.9 \pm 0.6)$ for pulsed protons.

error was always largest in the pulsed fitted dose response, this was taken over the smaller, continuous proton fitted dose response error.

3.2 EBT2 FILM RESPONSE TO LOW-ENERGY PROTONS

From the film measurements, a likewise comparison is made containing both the error in dose rate and error in the film calibration. As in Table 7, the measured dose in film 1 $\mathtt{filmD}_{\mathrm{Film1_M}}$ is compared to the expected dose based on the fluence said to have been delivered but now with 6 dose points. The measured dose shown in Table 9 has been obtained using the net OD and 6 MV photon calibration given in Equation 30. Although no cells were irradiated for the film calibration, the tabulated results shown below are always depicted alongside the cell dose as a reference point since this was designed especially for the experiment. A sample film and its corresponding dosemap is shown in Figure 37. Whereas Table 7 depicts the uncertainty in the fitting of the calibration curve and batch to batch variations during the cell irradiation, Table 9 contains an additional uncertainty due to fluctuations in the beam current. This effect increases with dose since the offset at low doses corresponds roughly to what was seen in Table 7, whereas for higher doses the uncertainty in the beam current becomes large enough to offset the sum of calibration fit line uncertainty and batch to batch uncertainty.

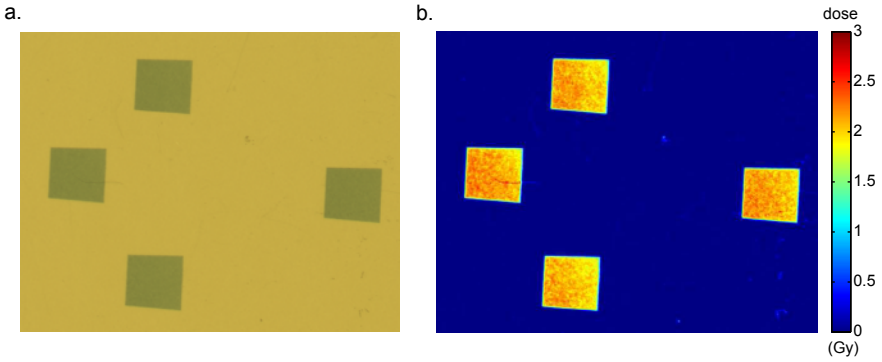

Figure 37: a. An example of a film 1 (active layer received 10.6 MeV protons) used for the film calibration irradiated with 4 dose squares for improved statistics. **b.** Corresponding dosemap to the irradiated film.

DETERMINING THE FILM UNDER-RESPONSE The under-response of the film UR is performed as a two-step process by first obtaining the calibration curve as in Figure 38a using the net optical densities in the film 1 and film 2, where the net OD has been determined according to Equation 29. The doses have been obtained using various measures: $\bar{\mathrm{D}}_{\mathrm{Film1_M}}$ utilises the 6 MV calibration curve established previously, $\bar{\mathrm{D}}_{\mathrm{Film2_C}}$ utilises Equation 31 and $\bar{\mathrm{D}}_{\mathrm{Film2_E}}$ is from Table 6, which was determined according to the hypothetical dose at the cell layer, defined by our experimental aims. The doses are the mean of several irradiated fields on a single film and are shown as points in Figure 38a with their corresponding fit lines. Additionally the lines $\mathrm{film1_R}$ and $\mathrm{film2_R}$ are plotted according to an independent calibration in the same experiment, which have been published in [100]. Figure 38a thus shows several important things:

- The 10.6 MeV proton curve conforms well to the 6 MV photon calibration thereby validating the use of the 6 MV photon calibration curve to determine the dose in film 1.
- Film 2 shows a definite under-response compared to film 1 by observing the net ODs based on the expected dose as well as the calculated dose.

Table 9: Average measured film doses in the cell irradiation calculated from net optical density and the 6 MV film calibration data listed in Equation 30. The difference between the measured dose using the 6 MV calibration and the expected dose shown in Table 6 is shown as $\mathrm{film}\Delta_{M/E}$ as a percentage. The average difference between $\mathrm{film}D_{\mathrm{Film1_E}}$ and $\mathrm{film}D_{\mathrm{Film1_M}}$ is $\mathrm{film}\bar{\Delta}_{M/E} = -3\%$.

D_{CELL} (Gy)	FILM $D_{\mathrm{FILM1_E}}$ (Gy)	FILM $D_{\mathrm{FILM1_M}}$ (Gy)	FILM $\Delta_{M/E}$ (%)
0.40	0.21	0.18	-14
		0.19	-10
		0.19	-7
		0.21	-2
0.60	0.31	0.29	-7
		0.27	-13
		0.30	-4
		0.30	-4
		0.33	6
		0.28	-8
1.00	0.52	0.49	-6
		0.53	2
		0.48	-7
		0.45	-13
1.50	0.78	0.80	2
		0.77	-2
		0.79	1
		0.81	4
2.00	1.04	1.01	-3
		0.99	-5
		1.00	-4
		1.04	0
4.00	2.07	2.08	1
		2.11	2
		2.05	-1
		2.14	3

- The low energy fit is not as good as the high energy fit thereby thereby adding to the error in the low dose dosimetry.
- Independent measurements of net OD generate slight variations in fit parameters.

The second step is to calculate the under-response itself, which is plotted in Figure 38b and uses the fit lines from Figure 38a with the parameters in Table 10 and Equation 33 at a fixed net OD defined here as:

$$UR = \frac{D_{6\,MV}}{D_{test}} \tag{33}$$

so that $D_{6\,MV}$ is the reference dose compiled with the 6 MV photon calibration and D_{test} is the dose according to the tested calibration curve. From Figure 38b it can be seen that *apparent* slight differences when fitting the calibration curve actually lead to substantial differences in UR values; illustrating the inherent uncertainties associated with film dosimetry. The final dose calibration curve used to calculate dose for the cell irradiations described in this thesis

was that given by film2_R as published in [100]. Using this fit, it is conceded here that usage must be accepted with an error of 10% owing to variations in netOD, batch to batch film variations, uncertainty in fit parameters and beam fluctuations.

Table 10: Top row shows fit parameters according to the photon calibration performed at the clinic. Film1 parameters are determined from 10.6 MeV protons and film2 parameters are determined from 3.2 MeV protons. Confidence intervals are shown at 68%. Parameter c remains fixed throughout the fitting procedure and a and b have been obtained using unconstrained non-linear least squares fitting.

CALIBRATION	A (Gy)	B (Gy)	C
6 MV	10.4 (10.1, 10.7)	59.5 (55.9, 63.1)	2.8
film1_R	11.6 (11.2, 12.1)	12.8 (3.8, 21.8)	2.4
film1_M	10.2 (10.1, 10.2)	33.0 (32.0, 34.1)	2.4
film2_R	14.6 (13.9, 15.3)	40.6 (28.5, 52.7)	2.4
film2_E	14.1 (13.2, 15.0)	43.1 (35.6, 50.6)	2.4
film2_C	13.5 (12.7, 14.3)	48.7 (42.3, 55.1)	2.4

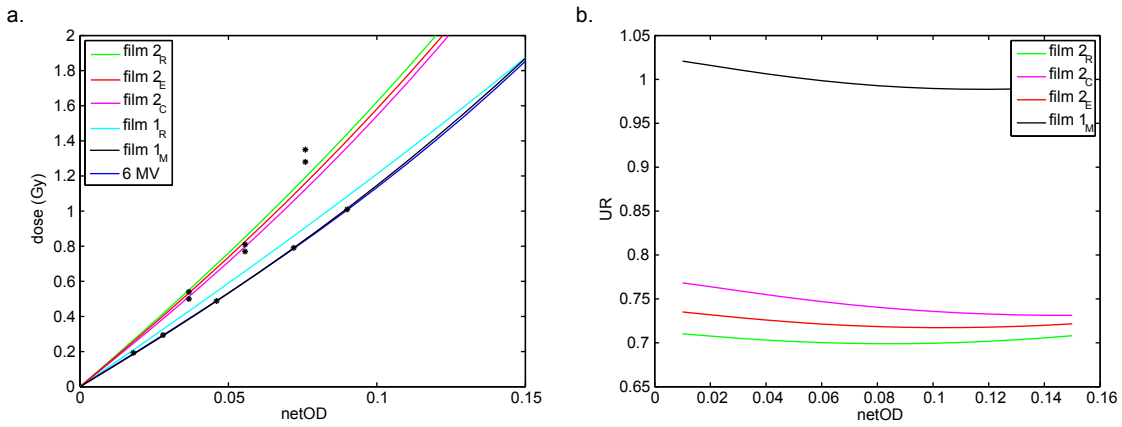

Figure 38: a. Fit lines according to the values in Table 10. The black data points correspond to film2_E, film2_C and film1_M over the dose range relevant to the cell irradiation. **b.** The under-response of EBT2 film at low energies determined as a function of net OD with respect to the 6 MV photon calibration.

3.3 COMPARISON OF CONTINUOUS AND PULSED PROTONS

3.3.1 *Focus Size*

The size of the foci is now analysed between the two radiation types. As mentioned in Part II Section 4.2, declaring a minimum volume when using this method of automated foci determination plays a critical role in the number of foci one counts. In 3D we again need to determine a minimum volume for foci counting, which, as for the 2D images, approaches the problem inversely. Figure 17 shows the volume distribution in 2D for a constant volume of 10 pixels - based on the assumption that this number is small enough to detect all foci as well as some noise. Adopting a similar mechanism in 3D, Figure 39(a-d) shows the distribution of the size of foci when using a minimum volume size of 20 pixels; this number being a starting estimate based on the knowledge that the foci must be bigger in 3D compared to 2D and necessarily small so as not to miss any foci. The volume distribution can be seen to approximate a Gaussian distribution for both continuous and pulsed protons in both the 2D and 3D case for all irradiated cells; this was not assumed when determining the μ and σ of the volume distribution. The minimum volume was determined as in Equation 15. As a final check on the validity of an appropriate volume, the controls are shown separately in Figure 39(e-h) in 3D, showing little difference in the mean value neither within an experiment (between γH2AX and 53BP1) nor across experiments (between continuous and pulsed protons). Thus comparing Figures 39(a-d) with Figure 39(e-h), an indisputable difference in size between irradiated foci due to continuous protons and irradiated foci produced by pulsed protons can be seen. This lends weight to the claim that different radiation types need to be treated differently according to variability in focus volume. In 3D, the minimum volume to define a focus is 27 and 30 pixels for γH2AX and 53BP1 foci respectively in continuous protons; and 79 and 78 pixels for γH2AX and 53BP1 foci respectively in pulsed protons.

To determine whether the focus size is influenced by dose, the mean focus area (Figure 40 (a-b)) and volume (Figure 40(c-d)) was calculated as a function of dose. The average area of one focus is plotted with resolution 1 px = 0.0104 μm^2. Thus aside from the controls, there is little dependence of focus size on dose for the given dose range. The continuous proton foci were smaller than the pulsed protons when both the mean area as well as the volume are considered. This effect is even more pronounced in the volume case. The results are summarised in Table 11.

Table 11: Comparison of mean focus sizes for continuous and pulsed protons.

	CONTINUOUS		PULSED	
	AREA (μm^2)	VOLUME (μm^3)	AREA (μm^2)	VOLUME (μm^3)
γH2AX	0.16±0.02	0.47±0.08	0.24±0.15	1.36±0.86
53BP1	0.20±0.02	0.50± 0.12	0.26±0.11	1.38±0.65

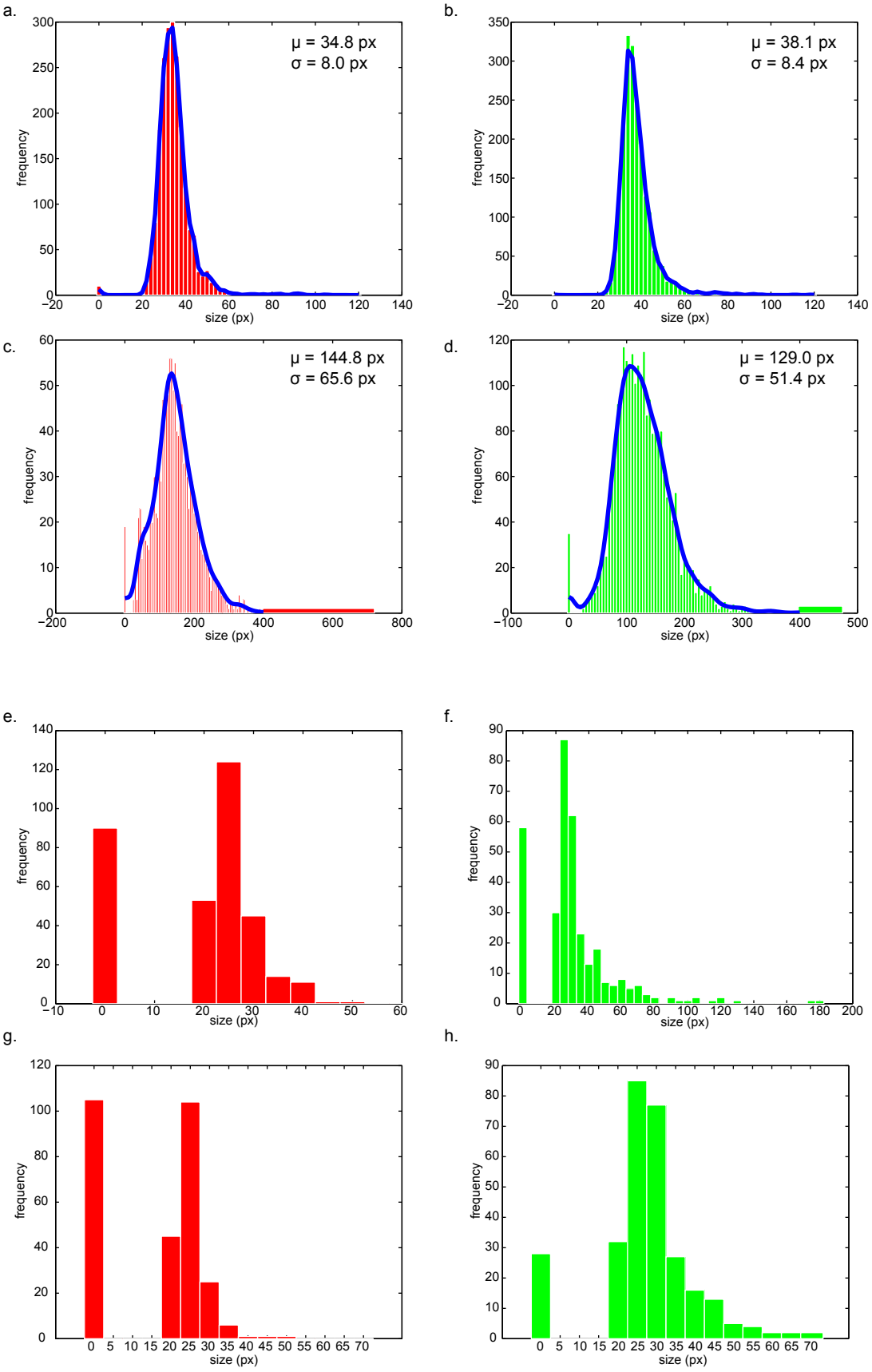

Figure 39: Volume distributions in 3D. **a.** γH2AX continuous protons. **b.** 53BP1 continuous protons. **c.** γH2AX pulsed protons. **d.** 53BP1 pulsed protons. **e.** γH2AX control continuous protons. **f.** 53BP1 control continuous protons. **g.** γH2AX control pulsed protons. **h.** 53BP1 control pulsed protons.

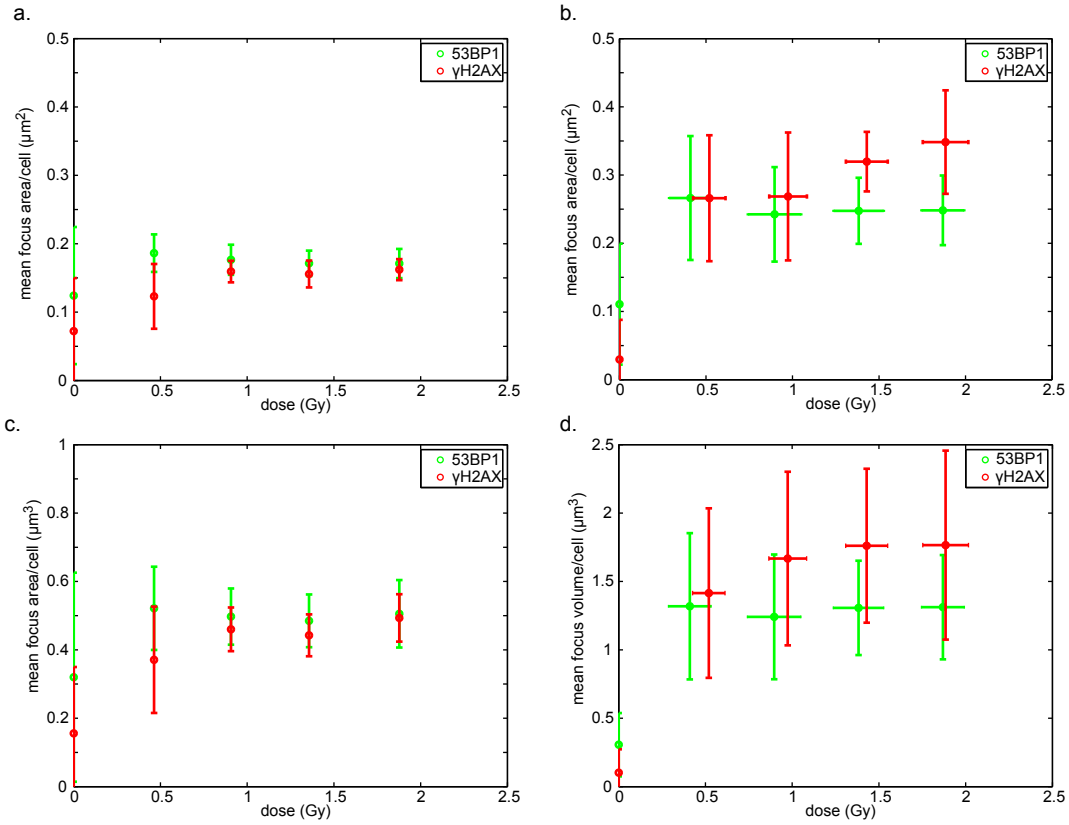

Figure 40: The mean size of a focus as a function of dose. Both the green channel (53BP1) and red channel (γH2AX) are shown. **a.** Mean focus area of continuous protons assuming the dose to be homogeneous. **b.** Mean focus area of pulsed protons where the mean focus area has been determined over 4 equally spaced dose bins not including the controls where error bars are the standard deviation for each dose point. **c.** Mean focus volume of continuous protons. **d.** Mean focus volume of pulsed protons using same binning procedure as in b.

3.3.2 *3D Dose Response*

We return now to the dose response in 3D with different minimum volumes between continuous protons and pulsed protons to compare the projected data directly with the 3D data. Figure 41 is shown again from Part II, Chapter 4, from which continuous protons appear to be more or less equal biologically in 2D. Producing a likewise comparison in 3D (see Figure 42) now yields a higher biological effect for the pulsed protons where we see that the loss of information when switching to 2D projection data proves to have an important effect in determining the RE. It is interesting to note that the loss of information when switching from 3D to 2D images is not as critical in the continuous proton data as for the pulsed proton data.

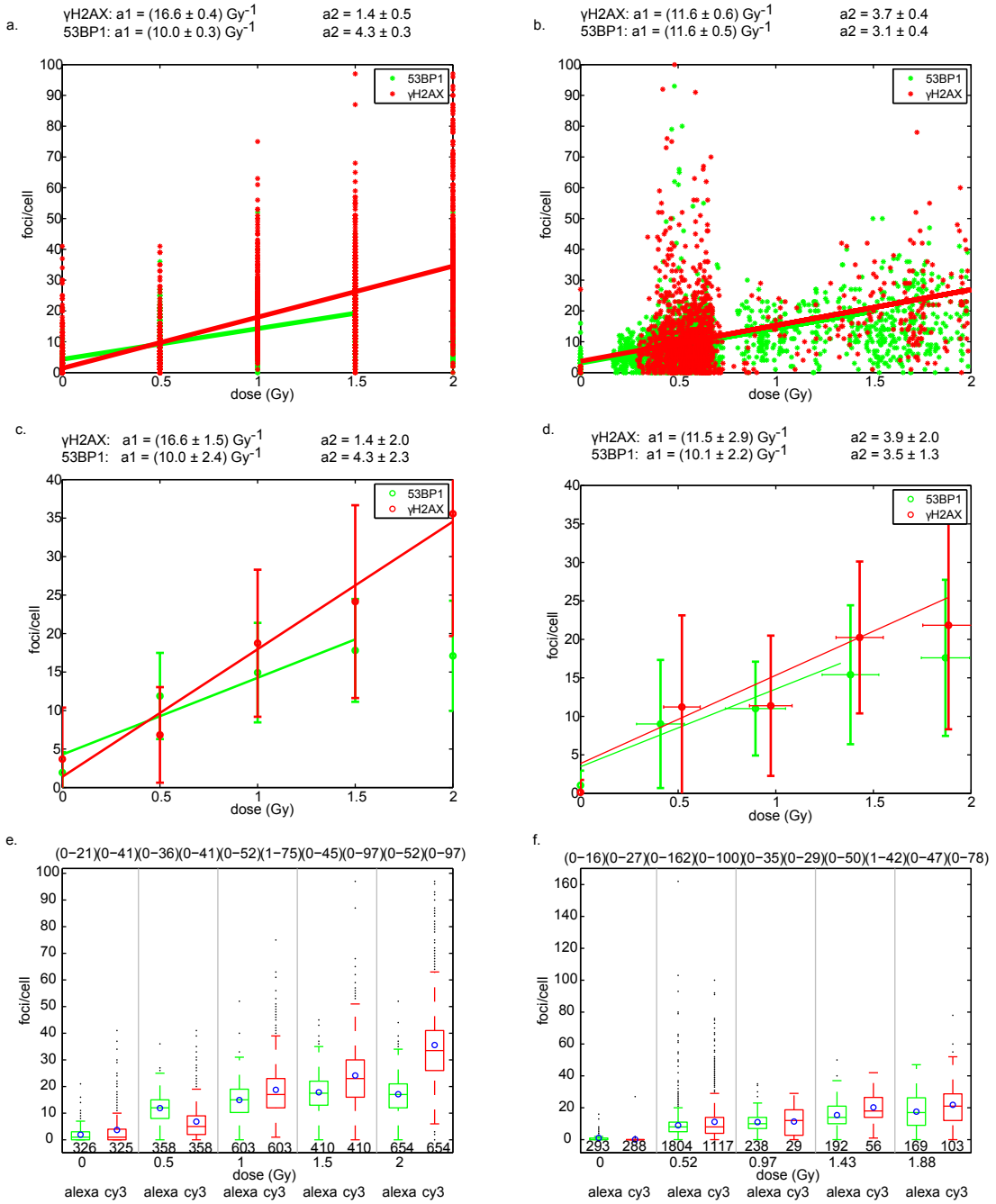

Figure 41: Maximum intensity image projection dose response as shown previously in Figure 18. **a.** Full data set with fit lines of continuous protons. **b.** Full data set with fit lines of pulsed protons. **c.** Continuous proton data shown as the mean of each dose point and the corresponding standard deviation in number of foci. **d.** Pulsed proton data binned with equal dose bin widths of 0.49 Gy (except for control data). The error bars indicate the standard deviation in both dose and foci directions. **e.** Continuous proton box plot. **f.** Pulsed proton box plot. The box plot shows the median within the box and the upper and lower boundaries of the box represent the interquartile range of the data per dose point. The whiskers show the extreme value limit (e. g. lower whisker=lower quartile value -1.5·lower quartile value) and any cells that are beyond the whiskers are presented as individual points known as the outliers. The number of cells per dose point are shown at the bottom of the graph and the range in number of foci is shown at top. The mean values are shown in blue circles.

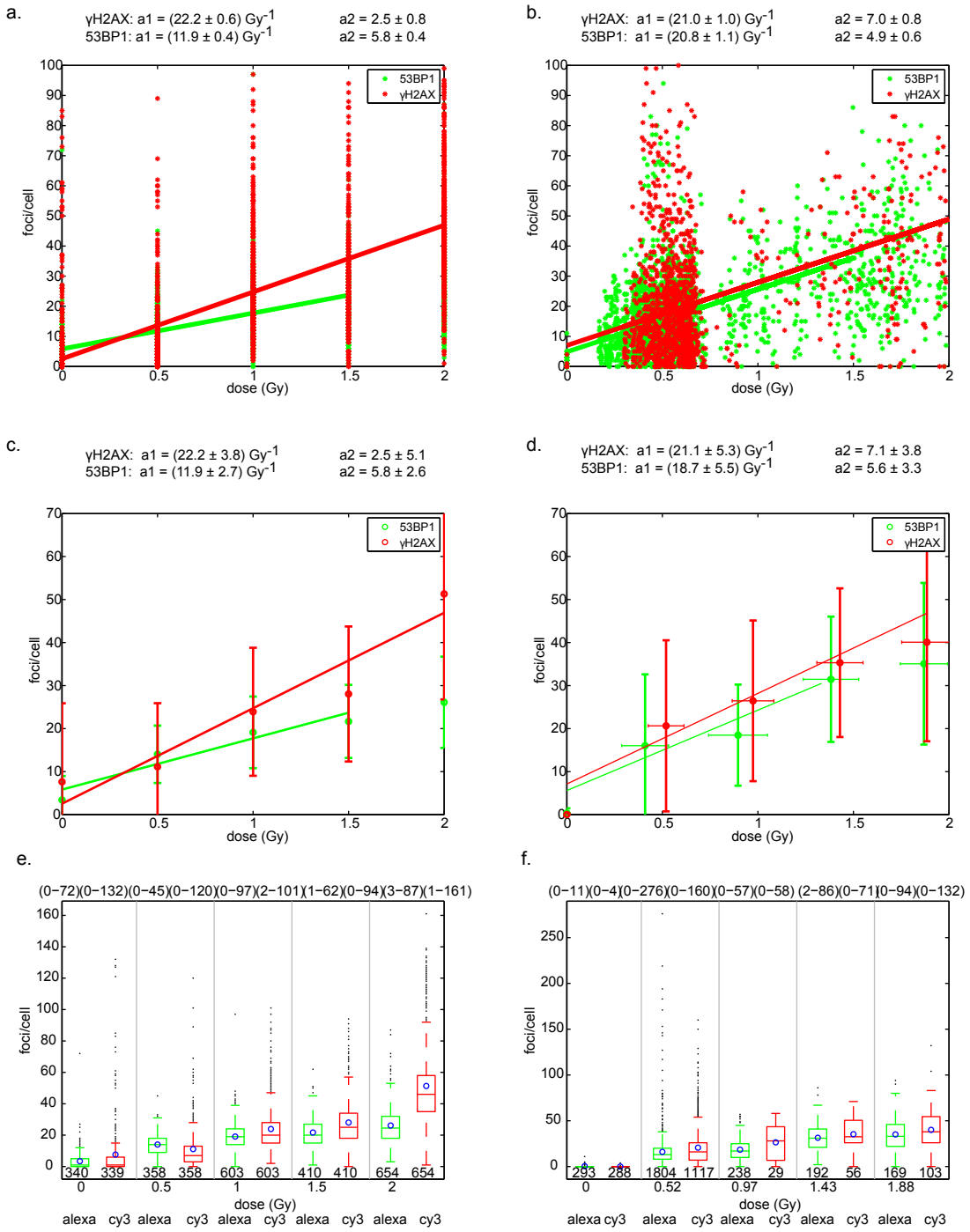

Figure 42: Dose response curves for a 3D analysis using Equation 13 and $\gamma = 0.1$ with minimum volume 27 and 30 px in the continuous protons and 79 and 78 px in the pulsed protons for γH2AX and 53BP1 respectively. Error bars correspond to the standard deviation in both foci and dose direction. The corresponding fit line parameters are shown in (a-d), which are applicable to the dose-response equation shown in Equation 16. Cells with doses > 1.5 Gy in the green channel (53BP1) were not included in the fit line. **a.** Continuous protons with fit lines constructed without any dose binning. **b.** Pulsed protons constructed as in a. **c.** Continuous protons mean foci/cell for each dose point. Error bars given by the standard deviation in the number of foci/cell. **d.** Pulsed protons mean foci/cell with 4 dose bins not including the controls. **e.** Boxplot of continuous proton dose response. **f.** Boxplot of pulsed proton dose response.

4

DISCUSSION

In this experiment, we set out to determine whether a biological difference existed between pulsed and continuous protons via an automated method of counting of γH2AX and 53BP1 foci. Here two time structures in proton dose delivery were directly compared against each other using the maximum intensity projected images to deduce a relative effect of 0.8±0.1 and 1.1±0.2 for γH2AX and 53BP1 respectively. This corroborates the findings by Zlobinskaya et al., who determined the RBE for both pulsed and continuous protons and found the continuous protons to have a higher RBE at all measured time points after irradiation [146]. Both these findings demonstrate a larger dose required by pulsed protons to produce the same biological effect than with continuous protons. In a comparable study, Zeil et al. also gauged the effect of the conventional protons in comparison to laser-driven protons using both γH2AX and 53BP1 foci, as well as cell survival, for which no biological difference was found [141]. However these results are not entirely equivalent to those presented here since the dose was delivered over several shots with a mean dose of 81 mGy delivered per shot by the laser in contrast to the results shown here for which the entire dose was delivered in a single shot.

Using 2D projected images rather than a stack of images as they were originally captured though results in a systematic error, which, depending upon the type of irradiation produces different effects. This became apparent when comparing the relative effect results to the average foci sizes since the amount of information that is lost when switching to 2D data results in a systematic underestimation of foci, which is also evident in the corresponding increase in size of the foci for pulsed compared to continuous foci. Consequently it was hypothesized that switching to the 3D data set should yield more reliable results. The RE now was found to be 1.3±0.2 and 1.9±0.2 for γH2AX and 53BP1 respectively. However this unusually high RE for 53BP1 foci is unlikely and reflects more the limitations in the procedure of foci estimation; especially when viewing the plateau in Figure 42a.

Comparing the size of the foci is an additional feature of the FociPicker_3D program output. In the projected images, on average, the pulsed proton foci were found to be consistently larger than the continuous protons. Our results here correspond well with the focus size findings reported in [26], however this group also found a dose dependence on foci size, which was not seen in our data except perhaps in the γH2AX pulsed proton data. However, with the size of the error bars, cannot be claimed with certainty. The overall size of the foci is interesting because it is thought that larger foci are indicative of the LET [73]. On the other hand, this increased size may also be put down to the fact that the dosimetry uncertainties in the pulsed proton data can account for more foci. These would show up as being larger because the foci tend to overlap at higher doses, assuming the doses are actually higher than what is shown here. Although no statistically relevant difference in the *number* of foci between the experiments was seen, there is a definite *size* difference in foci. Since the differences are subtle, perhaps the sensitivity of this respective method of foci counting is not great enough to observe an effect. As already seen, the absolute size of the foci in the pulsed experiment was significantly larger than the size of foci in the continuous experiment when comparing both volume and area. Since this aspect coincides with the minimum volume used to count foci, it is argued here that the minimum volume should be declared specific to both experiment and marker. By comparing the distribution in size of control foci for both continuous and pulsed

protons we can eliminate any differences in focus size being due to variances in experimental procedures. Whether this is due to an enhanced LET is difficult to say with certainty but might be verified/invalidated in other ways such as with experiments comparing irradiated hypoxic and normal cells.

A weakness in the biological data is the exclusion of data points with doses greater than 1.5 Gy in the 53BP1 channel. A possible cause of this may be that images were over-exposed in the Alexa488 channel during microscopy so that the signal saturates at high doses. This is certainly a reason to regard the 3D results in with 53BP1 with care. The Cy3 channel on the other hand consistently appeared weaker in signal (according to the human eye) for which however FociPicker_3D generally produced better results; this may be useful for the future.

The biological effect between continuous and pulsed protons here has been shown to be negligible within the error estimates using projected 2D images. In 3D however the pulsed protons show a slightly enhanced biological effect. This contrasts to the existing body of knowledge of radiation dose rate effects with xrays and electrons where ultra-high dose rates (10^9 Gys^{-1}) have been shown to deplete oxygen so that damage fixation did not occur; yielding a dose response similar to that of hypoxic cells [12][53][135].

The secondary aim of this chapter was to establish a low-energy calibration curve for EBT2 film under the assumption that the film exhibits an invariant dose response at an energy of 10.6 MeV. Assuming this to be true, the film exhibited an average under-response of 26% for an energy of 3.2 MeV. The error here largely resulting from the uncertainty in delivering the dose (10%), which is discussed in further detail below.

Radiochromic film is well known to exhibit an under-response at low energies whether for photons [25][28][75][102], protons or heavy ions [79] where the under-response in the dye is said to be due to recombination of free radicals at high LET that are responsible for the darkening in the gel [50]. Several generations of radiochromic film exist with MD-55 being amongst the first used for clinical dosimetry and reporting a dose underestimation ranging between 5-44% depending upon the energy (ranging from 5.3-100 MeV) owing to quenching at higher LET values [95][130]. An improvement in LET dependence was found in the next generation of gafchromic films - EBT, measured by Kirby et al. in the low energy region [69]. Additionally, Zhao and Das measured the energy response of EBT film with proton beams 50-160 MeV, demonstrating up to 20% under-response in the Bragg peak (~20 MeV) [143]. Angellier, Gautier and Hérault [6] summarised these findings by generating a low-energy response curve in EBT film from Kirby, Zhao and Martíšková, which is plotted as a relative effect in terms of LET. According to NIST data [11], we can expect our protons to have an LET value of 115 MeV/cm. Visually extrapolating this LET values with Angellier's curve, leads to a relative effect of ~0.75 thus falling into good agreement with the under-response reported here. The successors to EBT is the EBT2 film followed by EBT3. Thus a better comparison to our data might be that from Arjomandy et al. [7] who measured the EBT2 film response at proton energies of 100 and 250 MeV to find an UR within 5%. Since this correlates well to the data generated by Zhao and Das, and sensitive media are the same for both EBT and EBT2 [79], lending some weight to our results.

As mentioned in the methods section, a significant source of error during the film irradiation was the fact that dose delivery assessment could not be made in real time. Normally at SNAKE a photomultiplier is put in place to assess how many photons were delivered by noting the scintillation, however during the film calibration, this had to be removed because the films were placed in the beam path instead. This error, was estimated to be ~10% and is confirmed by comparing Tables 7 and Table 9 since $cell\bar{\Delta}_{M/E}$ shows the uncertainty with-

out beam fluctuations and $\mathrm{film}\bar{\Delta}_{M/E}$ shows the error with the fluctuations. Here the beam fluctuations approximately cancel out $\mathrm{cell}\bar{\Delta}_{M/E}$; especially evident at higher doses. Therefore we can conclude that the beam-related error is indeed ~ 10%, tending toward overdosing for increasing dose. Another difficulty associated with the beam delivery was some discrepancy between the expected field size and that which was measured in the films (45% less than what was expected). This however has not been taken into account in the dose calculation and should be verified with additional measurements.

Comparing the UR determined from $\bar{D}_{\mathrm{film2_C}}$ and $\bar{D}_{\mathrm{film2_E}}$ for the same net OD and that from $\bar{D}_{\mathrm{film2_R}}$ produced with a different net OD, a variation of 3% can be seen; this being due to differences in measuring net OD and possible differences in fitting algorithms. Comparing the calibration parameters between $\bar{D}_{\mathrm{film1_M}}$ and $\bar{D}_{\mathrm{6MV}}$, relatively good agreement can be found; justifying the use of the 6 MV calibration curve in measuring doses for proton energies exceeding 10.6 MeV. A very slight under-response in comparison to the 6 MV curve can be seen, however, using $\bar{D}_{\mathrm{film1_R}}$. This confirms the data by Angellier et al., where a slight under-response can be deduced with the corresponding LET [6]. Since the UR is relatively independent of dose [79], the accuracy of this experiment might be improved upon with more measurements at higher dose levels.

A final comment concerning the under-response calculated here is a difference in under-response definition. Equation 33 is not defined according to the conventional relative effectiveness definition of $RE = d_w(netOD)/(d_w)_{ic}$ [69], which utilises the dose to water in an ionisation chamber as a reference. For this reason the response tested here is termed the under-response (UR). The accuracy might be improved upon by using ionisation chamber measurements as a reference rather than film irradiated at a higher energy.

It has been shown here that in order to perform dosimetry with EBT2 film in laser-driven proton experiments, corrections need to be applied to the film due to quenching effects at high LET. It is envisaged that the energy will increase with increasing laser power [104][142] in the future and so the difficulty in accounting for the LET dependence at low energies will perhaps be a redundant calculation. Although some estimates have been produced here for a fixed energy, laser-driven protons are yet to produce sharply monoenergetic beams thus complicating our ability to accurately deduce the necessary correction factor. Given that the latest gafchromic film is EBT3, future experiments are likely to utilise this film rather than EBT2. However measurements comparing these two films indicate similar performance, most pertinently here, the quenching effects in regions of high LET [101].

Part V

SIMULATING A SHORT-RANGE CELL IRRADIATION

1 MOTIVATION

Charged particle interactions in matter are broadly classified by their LET, which may be high or low. In general protons are, like photons, considered to be low LET particles characterised by a high portion of indirect damage and non-dense track structure. When the high intensity, ultra-pulsed ATLAS laser interacts with an ultra-thin foil the resulting protons are accelerated out of the resulting plasma in the TNSA process. Because of this, the proton spectrum energy is wide (exponential with energy) and divergent out of the rear target side; arriving as a bunch, whose duration is largely affected by the broad energy spectrum as well as the angular divergence and target to cell distance. Owing to the bunching of the protons produced via the laser acceleration process, it is thought that the protons may exhibit higher LET and thus higher RBE than conventional sources of proton production due to collective processes where the bunched protons interact with each other and the irradiation target (i. e. cells) [40]. The mechanisms are yet to be completely understood, perhaps fuelled by the fact that such an hypothesized effect is yet to be seen experimentally. However with track-modelling software, the mechanisms behind such an effect are thought to be owing to the right combination of minimised time and space [72]. Indeed our own experiment with the ATLAS laser at MPQ failed to produce such an effect and pulsed proton experiments at the tandem accelerator for various biological endpoints have also come up negative. One proposed reason for such a failure, specifically relating to the laser-driven experiments is that, the spatial density of protons at the DNA site no longer meets the requirements for the high LET effect. A maximum distance of 10 cm has been estimated to be the limit before the interparticle distances within a cluster become too large for collective effects to occur [40]. Thus one could argue that the experiments to date have not yet been appropriately primed to see such an effect, since in our own laser experiment the cells were at a distance ~1 m from the source and the other experiments examining purely the time difference again, did not yield the appropriate clustering of damage.

Without modelling the processes occurring throughout the acceleration process, this section assumes such collective effects to be true, and uses the conditions claimed necessary to see a high LET as the aim of this section - under what experimental conditions can a picosecond proton bunch feasibly be delivered to cells? Thus this section examines the requirements necessary to maintain temporally dense ionisations from laser-driven protons where it is assumed that by maintaining a short pulse duration and short target to cell distance, the clustering effect of the bunch is maintained to the degree necessary for an enhanced biological effect.

In trying to achieve a picosecond pulsed proton bunch from the laser, the broad energy spectrum (2-7 MeV) will contribute the major part to pulse extension. In order to account for the broad energy spectrum, a short magnet between the target and the cells is proposed, (shown in Figure 43) where various combinations of pinhole, magnetic field and drift space are tested to find a minimum pulse duration of the order of picoseconds.

The simulation is performed here so that a rigorous and analytical description of the system could easily be written and is adapted to the specific laser conditions we can expect. This is easily constructed by considering the particle's trajectory throughout the system in its different components, where most are governed by straight line equations. Therefore all that remains is to simulate the starting conditions such as angle and energy spread. This technique, however, becomes increasingly demanding since it is dependent upon step increments concerning accu-

racy when simulating all possible combinations of energy and angular distribution described by the ATLAS laser. Therefore in order to improve the validity of the simulation, a natural solution was to randomly draw protons with the typical ATLAS laser characteristics and put them through the system as for a Monte Carlo simulation. All that remains then, is to track the particles in time and space and record those that successfully reach the imagined cells. Consequently the simulation cannot account for interactions between particles or any other physical processes and uses simply particle tracing to derive a pulse length and dose. The simulation therefore serves the dual purpose of simulating the ATLAS laser since beam time was quite scarce, as well as allowing us to make the necessary preparations through testing as many variables of the setup as possible; a situation, which might not otherwise have been afforded to us. The goal here is to determine for which configuration there exists a minimum in proton pulse duration that can be used to irradiate cells and be detected by a subsequent layer of film.

It is assumed the protons will be produced under the same conditions as the cell irradiation in Part III where the ATLAS high intensity laser is focused onto a Diamond-like-Carbon target using a parabolic mirror. Under these experimental conditions, the divergence of the beam is small (2°) [17] and a broad energy spectrum peaking at 7 MeV is produced. Therefore a magnet must be placed between the target and the cells as shown in Figure 43; where a pinhole will further exclude the range of energies and angles that contribute to the pulse duration.

The magnetic field is parallel to the x-axis, assumed to be homogeneous, time invariant and as a first setup attempt, produced by a permanent dipole magnet. The protons move perpendicular to the field (positive z-axis) towards the cells placed off-axis. The angular distribution is described by the angle alpha, α, which is in the yz-plane and in the xz-plane the distribution is declared to be phi, ϕ. Everything is described with respect to the z-axis, so that the z-axis is $\alpha = \phi = 0$ and all lengths are described parallel to it.

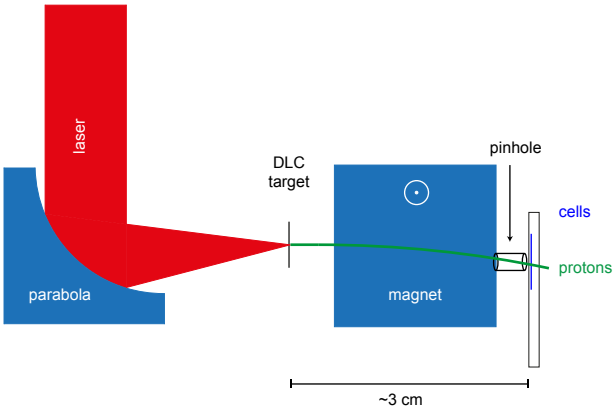

Figure 43: Proposed setup of a ps cell irradiation. The cells are brought as close to the target as possible, however due to the broad energy spectrum some energy selection is required. We try to achieve this through the use of a magnet between target and cells and the appropriate positioning of a small pinhole between the magnet and cells.

2

SYSTEM CONSTRUCTION

The system has been parametrically constructed to track the individual particles' position throughout the system, whose description can be simplified by subdividing it into four components. Therefore the system in its most basic form along the path trajectory comprises of: drift leading up to the magnet (x_1, y_1, z_1), helical motion owing to the Lorentz force through the magnet (x_2, y_2, z_2), some unavoidable drift between the magnet and collimation device (x_3, y_3, z_3) and finally drift through a pinhole defining the detection of particles at the end (x_4, y_4, z_4). At the end of each subsection the time and distance the particle has travelled is calculated and stored for pulse characterisation. Since the precision and thus success of the simulation hangs upon a complete description of the particle's motion, a rigorous treatment of the individual subsections is described below.

2.1 PARTICLE TRACKING

THE FIRST DRIFT d_1 leading up to the magnet is introduced because even if it is not intended for the final experiment it is realistic that there will be some drift prior to the magnet. Assuming the particles originate from a point source at the origin, then the equations of motion in the first drift area are for a straight line. This is the obvious case for all drift areas of the system. Since the z-axis is the reference axis, all other equations will be functions of z and their respective angular distributions in the corresponding plane.

$$\begin{aligned} z_1 &\in [0; d_1] \\ y_1 &= z_1 \tan(\alpha) \\ x_1 &= z_1 \tan(\phi) \end{aligned} \tag{34}$$

THE MAGNETIC FIELD d_B Charged particle motion in a magnetic field is governed by the Lorentz force so that the particle moves in a circle in the yz plane and in a helix along the magnetic field $\vec{B}$ when considered in 3D. Since $\vec{F}_B$ acts only on the perpendicular component of the velocity[1] , $\vec{F}$ can be simplified.

$$\begin{aligned} \vec{F} &= q(\vec{v} \times \vec{B}) \\ F_B &= qvB \sin\Theta \\ &= qv_\perp B \end{aligned} \tag{35}$$

Since the proton experiences a centripetal force, $F = m_p v^2/r$ and substituting into Equation 35, the particle moves on a helical track with radius r_p given by

$$r_p = \frac{p \cos(\phi)}{qB} \tag{36}$$

1 Θ is the angle between the $\vec{v}$ and $\vec{B}$ such that the z-axis coincides with $\Theta = \pi/2$. This is not to be confused with ϕ, which is defined for the z-axis to be zero, coinciding with the definition of α.

where $pc = \sqrt{(T + m_p c^2)^2 - m_p^2 c^4}$, q is the fundamental charge constant, m_p is the mass of a proton and T is its kinetic energy. For a magnet of length d_B along the z-axis, the particle will move on the arc of a circle in the yz plane with angular frequency $\omega = v/r = qB/m_p$. Since the particle moves with constant velocity in uniform circular motion, its angle θ is characterised at a time t by:

$$\theta = \omega t \tag{37}$$

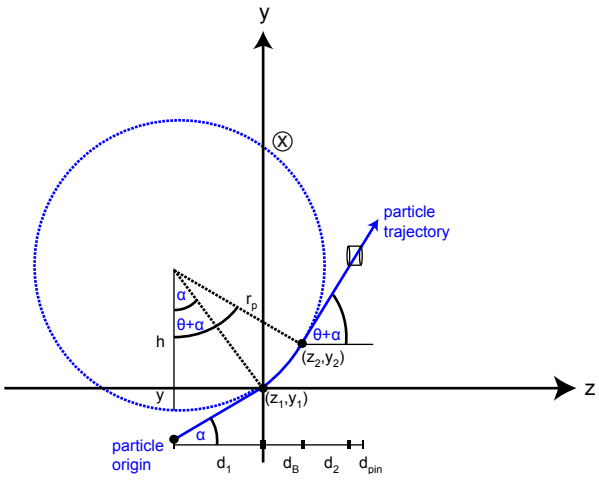

Figure 44: Schematic of system for a particle entering the magnet after a distance d_1 at an angle α drawn in the frame of reference for the circular motion beginning at the origin. The particle is deflected by the magnet through an angle of $\theta + \alpha$ and passes through the pinhole provided it has the appropriate position at the end of the pinhole.

Using Figure 44, the boundary conditions to derive the equations of motion can be inferred. These being:

- At the geometric origin, $\theta = 0$, $z = y = 0$.
- At the particle origin[2], $\theta = -\alpha$ so that

$$z = -r_p \sin\alpha \tag{38}$$
$$y = r_p \cos\alpha - r_p \tag{39}$$

The equations of motion are assumed to be of the form:

$$z = a + r_p \sin(\theta + \alpha) \tag{40}$$
$$y = -b - r_p \cos(\theta + \alpha) \tag{41}$$

which satisfies the boundary conditions when

$$a = -r_p \sin\alpha \tag{42}$$
$$b = -r_p \cos\alpha \tag{43}$$

By noting at the point (z_2, y_2), when the particle has been deflected through an angle of $(\theta + \alpha)$, that $z = d_B$ and substituting into Equation 41:

$$d_B = -r_p \sin\alpha + r_p \sin(\omega t + \alpha)$$
$$\omega t = \sin^{-1}(d_B/r + \sin\alpha) - \alpha \tag{44}$$

Up to now only the circular motion in the yz-plane has been considered. However since B only acts $v_\perp$, motion in the xz-plane is given by a straight line dependent upon the angle ϕ

2 Although the circle's coordinate system is used to derive the equations of motion, the particle's reference frame beginning at the particle origin is used for all future plots.

at which the particle lies with respect to z. The equations of motion for the particle under the influence of $\vec{B}$ are:

$$\begin{aligned} z_2 &= -r_p \sin(\alpha) + r_p \sin(\theta + \alpha) + z_{1_b} \\ y_2 &= r_p \cos(\alpha) - r_p \cos(\theta + \alpha) + y_{1_b} \\ x_2 &= z_2 \tan(\phi) + x_{1_b} \end{aligned} \tag{45}$$

where $(x_{1_b}, y_{1_b}, z_{1_b})$ refers to the *final element* in Equation 34 so that the paths meet from section to section. This notation will be kept throughout the remainder of this chapter and is applied for each segment of the system. Since $-1 < d_B/r_p + \sin\alpha < 1$, Equation 45 holds only as long as d_B is not allowed to be long enough for the particles to complete a full revolution. Aside from the initial conditions, the magnetic field component of the system will affect the detectable particles through the magnitude of the magnetic field as well as the length along the z-axis.

THE SECOND DRIFT d_2 The second drift space is assumed to be small but inevitable and lies between the magnet and the pinhole. It is a parameter which could potentially enhance the desired biological parameters to be assessed and thus is allowed to vary later in the calculation. In the yz plane it is governed by a straight line with an exit angle depending on the angular frequency in the magnetic field. Whereas in the xz plane, it remains a straight line but with a gradient according to the angle at which it lies with respect to the magnetic field.

$$\begin{aligned} z_3 &\in [z_{2_b}; d_2] \\ y_3 &= z_3 \tan(\theta + \alpha) + y_{2_b} \\ x_3 &= z_3 \tan(\phi) + x_{2_b} \end{aligned} \tag{46}$$

THE PINHOLE DRIFT d_{PIN} The pinhole is constructed to be cylindrical with a radius r and length L. r and L can be adjusted to maximise the parameters we are interested in. As a starting point, it is positioned such that its centre coincides with deflection of a particle with $T = 7$ MeV, $\alpha = 0$, $\phi = 0$ and thus lies off-axis with respect to y. This ensures that some particles will always make it through the system. Therefore the pinhole affects the detectable spectrum via its positioning, radius and length. The equations of motion are of a similar form as in Equation 46, however along the interval $z_4 \in [z_3; L]$. Therefore by tracking the particles at the final position of the pinhole, a number of particles would be excluded by the pinhole according to their positions in x and y.

$$\begin{aligned} z_4 &\in [z_{3_b}; d_{pin}] \\ y_4 &= z_4 \tan(\theta + \alpha) + y_{3_b} \\ x_4 &= z_4 \tan(\phi) + x_{3_b} \end{aligned} \tag{47}$$

The particle's motion is now completely described and tracked in time and space, by connecting all the subsections into a final system using Equations 34, 45, 46 and 47. The motion is plotted in all three planes as shown in Figure 45.

2.2 TESTED GEOMETRIES

2.2.1 *Straight pinhole*

The most intuitive setup involves placing a pinhole at the end of the magnet, which can vary according to the radius (in x and y) and length (in z). Its positioning is constructed by

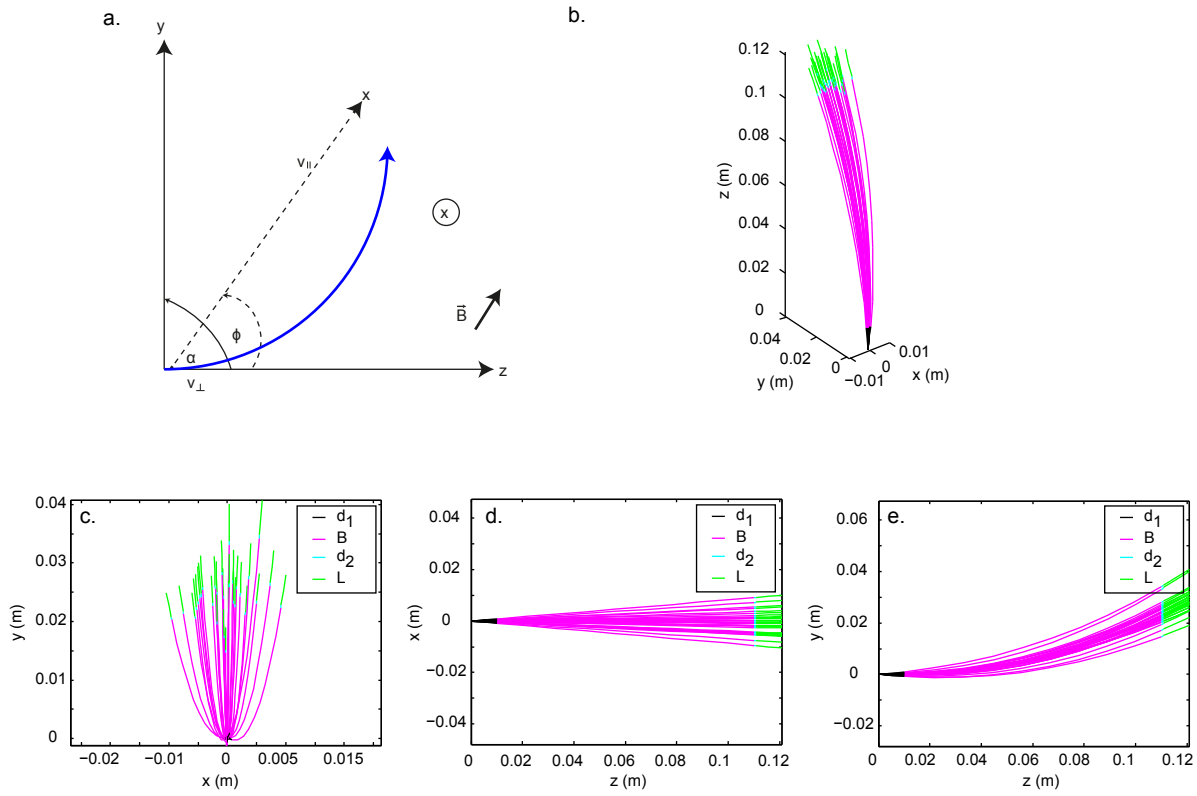

Figure 45: a. Coordinate system of simulation for particles moving in the positive z direction from a point source at the origin. $v_{\perp}$ is in the yz plane and $v_{\parallel}$ is parallel to $\vec{B}$. α is in the yz plane and ϕ is in the xz plane. **b.** 3D trajectory of 30 particles throughout the 4 different regions of the system. The particles follow a helical track limited by the magnet dimensions. Here $\vec{B} = 1$ T. **c.** Particle motion projected onto the yx plane. **d.** Particle motion projected onto the xz plane (i. e. in the $\vec{B}$ plane) showing the distribution of ϕ. **e.** Particle motion in the yz plane showing the magnetic field deflection on $v_{\perp}$ over the length of $\vec{B}$ showing the distribution of α.

taking some reference particle, $T = 7$ MeV and $\alpha = \phi = 0$ rad, and having this particle's final deviation at y_4 (i. e. *exit* position) off the central axis as coinciding with the centre of the pinhole. The name straight pinhole refers to its geometry so that its start position in y, P_1 and its end position, P_2 is $P_1 = P_2$. 7 MeV is preferable to 2 MeV since the number of particles decreases exponentially with energy (see Figure 46a), which is useful for controlling the dose as well as making it easier to separate the different energies from each other and in doing so reduce the pulse duration.

2.2.2 *Tilted pinhole*

Due to the low doses seen in the laser experiment, it was expected that this might also be a problem for the simulation given here. In order to compensate for this, the pinhole is now tilted so that the centre of its *starting* position coincides with the reference particle at y_3 and its *exit* position coincides with the reference particle at y_4 i. e. $P_1 < P_2$. Therefore depending upon the expected spectrum produced by the laser, the pinhole can be tilted to accommodate the angle at which the reference particle drifts through the pinhole. Practically this translates into a rotation of the pinhole at the point (x_3, y_3, z_3) of $\sim 15°$ using the starting conditions shown in Table 12.

2.3 MONTE CARLO CONSTRUCTION

In order to reduce the error in the variables to be tested (pulse duration and dose) as well as account for a non-uniform distribution of input parameters, a Monte Carlo method is used. To produce a typical ATLAS spectrum, the kinetic energy T is generated using the inversion method outlined in Figure 46. This is performed by measuring or assuming a distribution of the characteristic parameter to determine the probability density function. Let the probability density function of the spectrum be $p(x)$, which is related to the cumulative distribution function $P(x)$ by

$$P(x) = \int_{-\infty}^{+\infty} p(x')\, dx' \tag{48}$$

Taking a continuous random variable U uniformly distributed on $[0, 1]$ and the distribution function $P(x)$, the random variable $U = P^{-1}(U')$ will have distribution $p(x)$. This holds while $P^{-1}(P(x)) = x$ meaning that the distribution function must be invertible. If $p(x)$ is continuous, Equation 48 is often not easily calculated analytically (e. g. the normal distribution returns a gamma function cumulative distribution) here however, since the energy spectrum is discrete (Figure 46a), the individual probabilities can be summed cumulatively to obtain $P(x)$ (Figure 46b).

Thus by drawing pseudo random numbers and applying to $P^{-1}(x)$, then random numbers with the distribution $p(x)$ can be generated (Figure 46). This can be applied to the energy spectrum to generate T from experimental measurements. On the other hand, to generate the appropriate angular distribution in α and ϕ, a Gaussian distribution centred on the z-axis is assumed using the known full width half max (FWHM) of $5°$ for which the standard deviation σ can be calculated using the general form of the Gaussian equation in 1D:

$$f(x) = \frac{1}{\sigma\sqrt{2\pi}} \exp\left(-\frac{(x-\mu)^2}{2\sigma^2}\right) \tag{49}$$

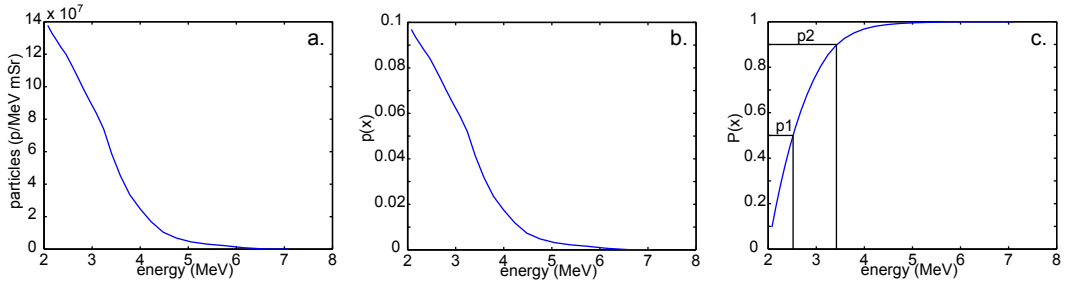

Figure 46: a. A typical energy spectrum produced from the ATLAS laser. This follows an exponential distribution according to the TNSA scaling laws. **b.** The probability density function $p(x)$ is calculated from a. **c.** The cumulative distribution function $P(x)$ is related to $p(x)$ via Equation 48 so that pseudo random numbers generated on $P^{-1}(x)$ produce random energies following the distribution of $p(x)$. The point p1 will draw a particle $T = 2.5$ MeV and the point p2 will draw a particle $T = 3.4$ MeV, thus for < 10% of the numbers drawn, the particles will have energies exceeding 3.4 MeV and that most particles will be in the low energy portion of the spectrum as can be seen from the exponential distribution $p(x)$.

Here the distribution for α and ϕ has mean $\mu = 0°$. Equation 49 is not to be confused with as being as a function of x in the current coordinate system rather it signifies either α or ϕ. σ can be calculated using:

$$\sigma = \frac{\text{FWHM}}{(2\sqrt{2\ln 2})} \tag{50}$$

A sample energy spectrum produced using the inversion method is shown in Figure 47a. And from Equation 50, the angular distribution of particles is said to be of the form shown in Figure 47b from which random α and ϕ were drawn.

To simulate the beam, $1 \cdot 10^7$ particles are generated meaning that $1 \cdot 10^7$ random α, ϕ and T were generated. Each particle is tracked throughout the system for its final position such that those whose final characteristics do not meet the cut-off criteria are discarded. The cut-off criteria are defined by the final position and angle, meaning that the test particles need to clear the first edge of the pinhole at (x_3, y_3, z_3) as well as have their final position (x_4, y_4, z_4) within the range specified by the radius of the pinhole. The characteristics of those particles that fall within the limits of the pinhole at positions (x_3, y_3, z_3) and (x_4, y_4, z_4) are binned so that information concerning the energy, angular distribution and position are kept. The energy binning is particularly relevant for the dose calculation, where the energy bins that the original energy spectrum was given in are maintained.

2.4 PULSE DURATION ΔT

The pulse duration is obtained by finding the particle with the maximum time required to pass through the system and the particle with the minimum time required to pass through the system. Therefore information concerning each particle that successfully reaches the detector at the end of the pinhole is retained. The time for each particle that follows a straight line path (i. e. for sections d_1, d_2, d_{pin} of the system) is obtained by determining the distance travelled throughout each section:

$$d = \sqrt{(x_b - x_a)^2 + (y_b - y_a)^2 + (z_b - z_a)^2}$$

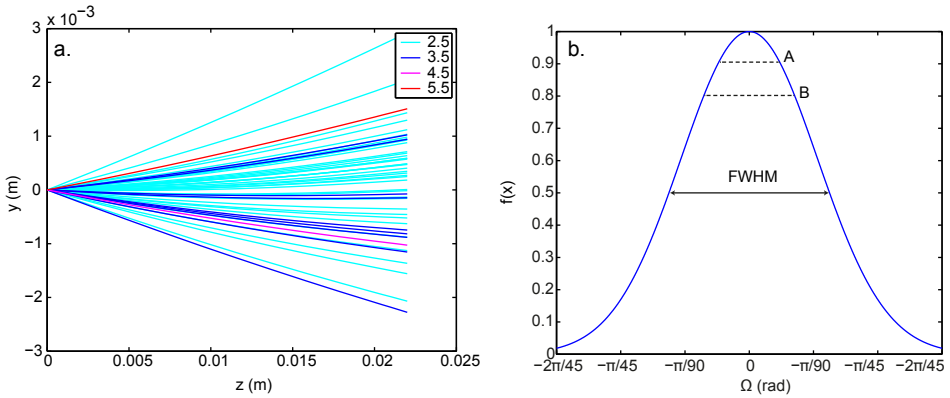

Figure 47: a. A random energy spectrum of 30 particles generated prior to eliminating those that do not meet the exception criteria imposed by the magnet and pinhole. Energies are generated according to the distribution in Figure 46b with an angular distribution according to Equation 49. Since the $P(x)$ is exponential in increasing energy, far more low energy particles are generated. **b.** The angular distribution of particles for both α and ϕ so that $\sigma \approx 2.12°$. A and B are described in detail in Section 2.5.

where (x_a, y_a, z_a) denotes the particle's position at the start of a drift section and (x_b, y_b, z_b) denotes the particle's position at the end of a drift section. And noting the velocity of each particle:

$$v = \frac{p}{m_p \gamma}$$

where $\gamma = (T + m_p c^2)/m_p c^2$, p is the momentum previously defined in Section 2.1. Thus the time for a particle to pass through a drift or pinhole section is:

$$t_{drift} = \frac{d}{v \cos(\phi)} \tag{51}$$

and for motion through the magnetic component the time is

$$\begin{aligned} \omega &= \frac{v \cos(\phi)}{r} \\ t_B &= \frac{\theta}{\omega} \end{aligned} \tag{52}$$

where θ has been previously defined in Equation 44. The simulated pulse duration delivered to the cells is thus:

$$\begin{aligned} t &= t_{d_1} + t_{d_B} + t_{d_2} + t_{d_{pin}} \\ \Delta t &= t_{max} - t_{min} \end{aligned} \tag{53}$$

2.5 DOSE CALCULATION

In order to calculate the dose, the number of particles in the spectrum that is produced in the plasma needs to be known. From the experimental measurements, an energy spectrum like the one shown in Figure 46a is obtained. The particles detected in such a measurement are

only a portion of the original number of protons that were produced at the target. This portion is marked in Figure 47b as the point A. According to the aim of this experiment, the pulse duration should be as short as possible. This can be minimised when the cells are brought very close to the target so there is less chance for the particles to drift apart from each other due to the initial angular divergence with which the beam is produced. As a result, the region of the particle distribution that is being detected increases now from A to B. Therefore a method is required that can transform the measured spectrum (experimental) to the current, short-range spectrum (simulation). This can be achieved by calculating the efficiency of the system X for all energies as well as knowledge of the original spectrum N_0.

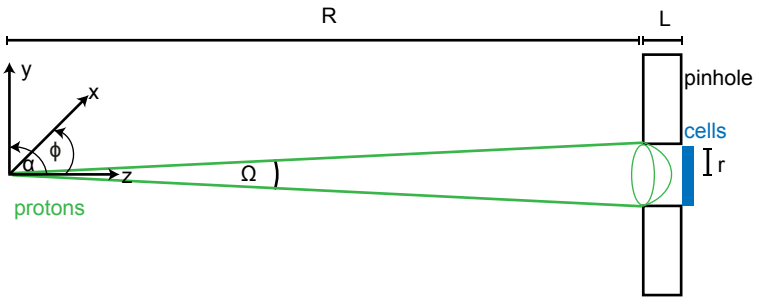

Figure 48: Schematic of the short pulsed cell irradiation setup with a straight pinhole. Protons are produced at the target with solid angle Ω. The exaggerated tip of the solid angle distribution protruding into the pinhole is approximated in the calculation of Ω as a flat surface. The detected tip is only a fraction of the original spectrum N_0.

The efficiency of the system in the simulation for each energy is determined by noting the number of particles randomly generated N_g [p/MeV mSr] as well as the number of detected particles N_d [p/MeV mSr]. The efficiency is thus

$$X = \frac{N_d(T,\Omega)}{N_g(T,\Omega)} \tag{54}$$

As mentioned in Section 2.3, the angular distribution is described by a Gaussian. To calculate N_0, the surface area of the tip of the solid angle distribution projected over a circle needs to be determined (see Figure 48). This can easily be solved by performing a double integral in polar coordinates since the limits can simply be interpreted from the circle defined by the pinhole. In order to do this however the distribution should first be transformed from units of angle into Cartesian coordinates. We begin with the equation that governs the measured spectrum N_m, which has been plotted already in Figure 46a.

$$N_m = N_0 \int\int f(\alpha,\phi)\, d\alpha d\phi \tag{55}$$

To calculate the dose we detect in the simulation, Equation 55 needs to be solved for N_0. We therefore start with a 2D description of the beam in terms of α and θ:

$$f(\alpha,\phi) = \frac{1}{2\pi\sigma^2} \exp\left(-\frac{\alpha^2+\phi^2}{2\sigma^2}\right) \tag{56}$$

Equation 56 is difficult to quantify since its coordinate system has units of radians and the system has been produced in Cartesian coordinates. From Figure 48, geometrically we have:

$$\tan\alpha = \frac{y}{R}$$
$$\tan\phi = \frac{x}{R}$$

where r is the radius of the pinhole and R is the radius of the solid angle given by the particles i. e. the distance from the target to the pinhole. Using the small angle approximation $\tan\alpha \approx \alpha$, Equation 56 can be obtained in terms of x and y.

$$\alpha = \frac{y}{R}, \quad d\alpha = \frac{dy}{R}$$
$$\phi = \frac{x}{R}, \quad d\phi = \frac{dx}{R}$$

Equation 55 now becomes

$$N_m = N_0 \int\int \frac{1}{2\pi\sigma^2} \exp\left(-\frac{x^2+y^2}{2\sigma^2 R^2}\right) \frac{dydx}{R^2} \tag{57}$$

Integrating Equation 57 in polar coordinates using $x = \rho\cos\theta$, $y = \rho\sin\theta$ and $dydx = \rho d\theta d\rho$ we have

$$\begin{aligned} N_m &= N_0 \left(\frac{1}{2\pi\sigma^2}\int_0^{2\pi}\int_0^r \exp\left(\frac{-\rho^2}{2\sigma^2R^2}\right)\frac{\rho}{R^2}\, d\rho d\theta\right) \\ &= N_0 \frac{1}{\sigma^2R^2}\int_0^r \rho \exp\left(\frac{-\rho^2}{2\sigma^2R^2}\right) d\rho \end{aligned}$$

Integrating by parts returns

$$N_m = N_0\left(1 - \exp\left(\frac{-r^2}{2\sigma^2R^2}\right)\right) \tag{58}$$

Equation 58 gives the fraction of particles from the beam that were detected in the original measurement at A under the conditions $r(A)$ and $R(A)$. The new setup however will detect more particles marked at B. The original spectrum $\bar{N}_0$ is given by

$$\bar{N}_0 = N_m \frac{\Omega}{1 - \exp\left(\frac{-r(A)^2}{2\sigma^2R(A)^2}\right)} \tag{59}$$

where the solid angle $\Omega \approx \pi r(A)^2/R(A)^2$ has been introduced to eliminate the solid angle dependency. The dose D is then summed over all energies

$$D = \sum_{i=1}^{T_{max}} \frac{\bar{N}_{0_i} X_i S_i}{\pi r(B)^2} \tag{60}$$

where $r(B)$ is a free-varying parameter in the tested simulation according to the radius over which the particles extend and not for the measured spectrum. X is the efficiency as defined previously in Equation 54 and S is the mass stopping power.

3 RESULTS

In order to make comparisons between the two setups proposed, the same initial conditions were used as input parameters, except for when it is the variable being tested in which case it is increasing. These values are shown in Table 12, and all other universal constants are given in this step as well.

Table 12: Input variables common to both setups in the simulation.

PARAMETER	QUANTITY
$\|\|\vec{B}\|\|$	1 T
$\vec{B}$ length	$3 \cdot 10^{-2}$ m
drift 1	$1 \cdot 10^{-3}$ m
drift 2	$1 \cdot 10^{-3}$ m
pinhole length	$5 \cdot 10^{-3}$ m
pinhole radius	$1 \cdot 10^{-3}$ m

The values listed in Table 12 are based on the following: 1 T is the maximum strength achievable with a permanent magnet where we already have some small magnets 3 cm in length at our disposal; drift spaces of 1 mm is a generous estimate of the air gaps between sections of the system; pinhole length needs to be of a minimum thickness so as to completely stop protons outside of this pinhole (see below); and pinhole radius needs to be as small as possible, which is limited by what the workshop can achieve, being able to accurately position the pinhole, allowing a minimum dose level and a minimum number of cells that must be detected for reasonable counting statistics.

A minimum thickness of material comprising the length of the pinhole can be determined by the range of the protons in a dense material such as lead. The proton range [g/cm^2] in a homogeneous material is defined by:

$$R(E_0) = \int_{E_0}^{E_f} \left(\frac{1}{\rho} \frac{dE}{dx} \right)^{-1} \tag{61}$$

where E_0 is the initial energy, E_f is the final energy ($\neq 0$) and $\frac{1}{\rho}\frac{dE}{dx}$ is the mass stopping power. According to the NIST stopping power tables, $R = 0.192$ (g/cm^2) for 7 MeV protons in lead so that the pinhole needs to have a minimum length of 0.02 cm [11].

3.1 SINGLE STRAIGHT PINHOLE

3.1.1 *Drift space dependence*

The second drift space is plotted in Figure 49 showing the effect of increasing the drift length in the positive z-direction. The dose and pulse duration compete with each other since the dose here should be minimised as should the pulse length.

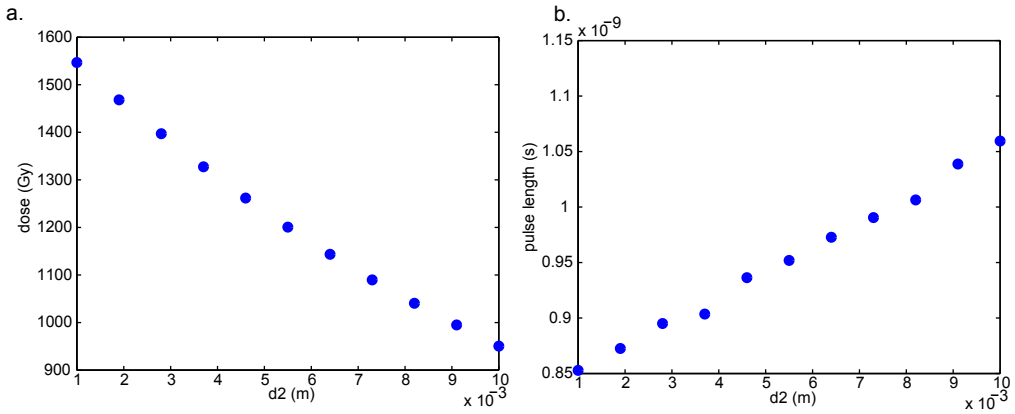

Figure 49: The endpoints dose and pulse length are tested here by increasing the drift space d_2. **a.** The dose decreases as a function of the second drift space. **b.** The pulse length counteracts the dose since it increases with increasing drift length though less dramatically than with dose.

3.1.2 *Pinhole dependence*

The pinhole can be used in several ways to affect the dose and pulse length. The most obvious ways are plotted in Figure 50 showing the dependence on increasing length of the pinhole along the z-axis in (a-b) and increasing radius of the pinhole in (c-d). The starting conditions declared in Table 12 have been replaced for changing pinhole conditions and all other variables remain as declared.

Using a fixed pinhole radius of 1 mm as outlined in Table 12, the length of the pinhole must be short enough to allow detection of particles. With regards to dose though, the pinhole length can be used to our advantage so that by increasing the length of the pinhole, more particles will be filtered out. This, however is at the cost of increased pulse duration. Evidently the transition from length being useful to critical applies over a steep gradient.

When increasing the radius on the other hand, the pulse reaches a plateau due to inclusion of all energies within the detected area. Dose increases as a function of increasing radius as can be expected though only up to a point after which all particles will be admitted through the pinhole.

Since it is difficult to find the minimum when considering both the pinhole length and radius, a 3D plot projection has been calculated to find the optimal combination between the two factors for both dose and pulse length pictured in (e-f). These figures show that there is no combination of pinhole length and radius that would yield a low enough dose and interestingly short enough pulse duration. The lowest dose of 112 Gy would have a 1 ns pulse duration and the shortest pulse shown here would be $7 \cdot 10^{-10}$s corresponding to a dose of 1200 Gy using this current setup.

3.1.3 *Magnetic field dependence*

The magnetic field is responsible for deflecting the particles where the force imparted on the particles is proportional to their kinetic energy. Using this property in combination with an appropriately positioned pinhole acts as an energy filtration system and in doing so reduces the pulse length detected at the end of the pinhole. The individual dependencies for magnetic field magnitude (a-b) and length (c-d) are shown in Figure 51. These two dependencies are shown simultaneously in (e-f) using the projection of a 3D plot.

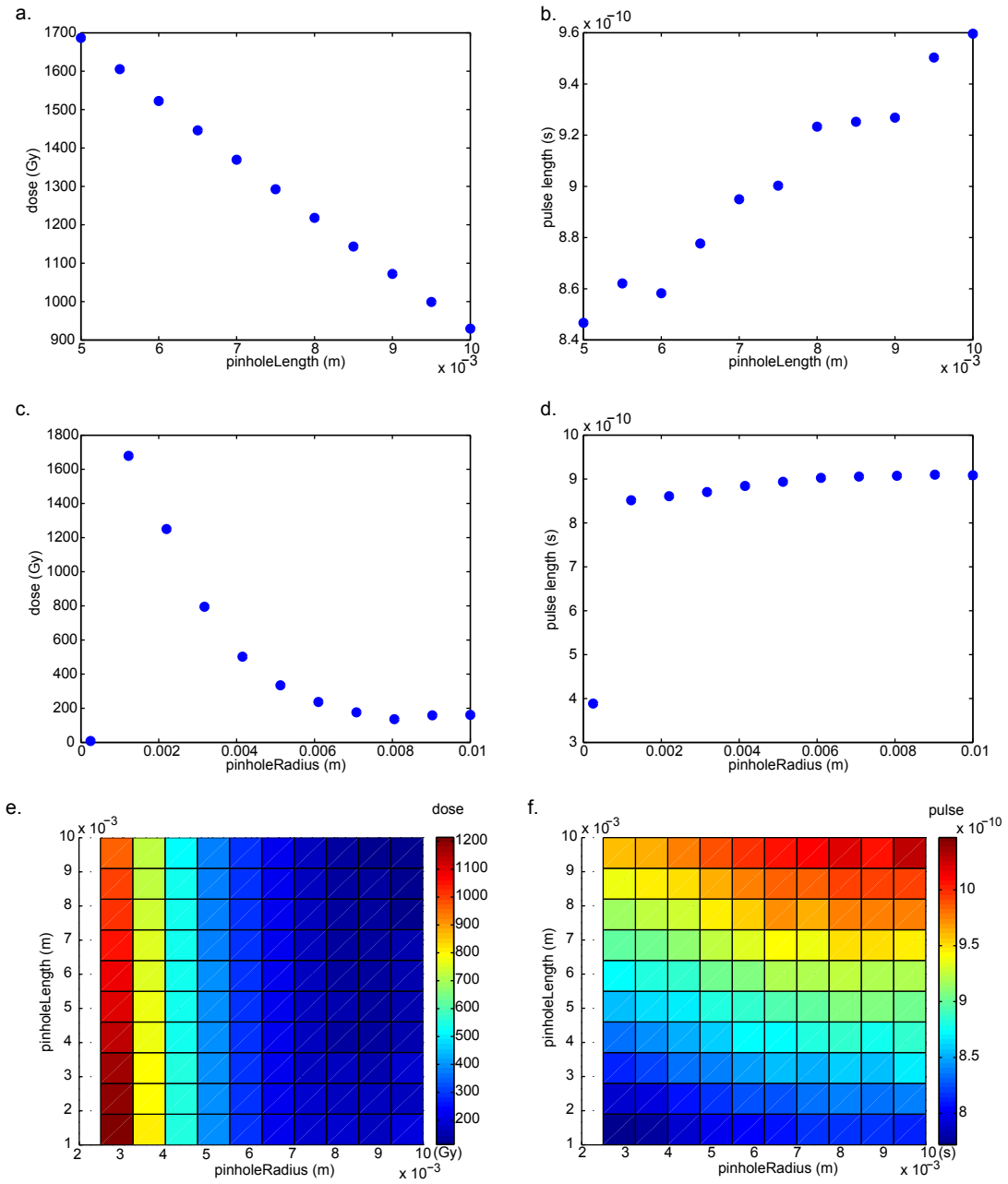

Figure 50: a. Dose decreases rapidly as a function of pinhole length. **b.** The pulse length increases as a function of pinhole length until a critical point after which no more particles reach the detector and so the pulse duration becomes zero. **c.** Dose increases as a function of pinhole radius up to ~ 1 mm since more protons are let in, after which dose decreases due to this factor being outweighed by the inverse dependence of dose on area. **d.** The pulse duration tends to plateau as a function of the pinhole radius thereby making this property easy to maximise for our interests. **e.** Dose projection varying pinhole length and radius simultaneously. **f.** Pulse length projection varying pinhole length and radius simultaneously.

As the magnitude of the magnetic field increases, the particles separate according to energy and angular distribution so that the dose drastically decreases. A similar effect on the dose is also seen when increasing the length of the magnet but necessarily increases pulse duration due to the angular spread on the particles emitted from the target. If, however, the magnet is increased, this effect occurs over a shorter magnet length, so that the particle number decreases for increasing magnet length. Under the initial conditions with a magnet 1 cm long and 5.8 T strong, a dose of 6 Gy and pulse of $1 \cdot 10^{-10}$s can be obtained.

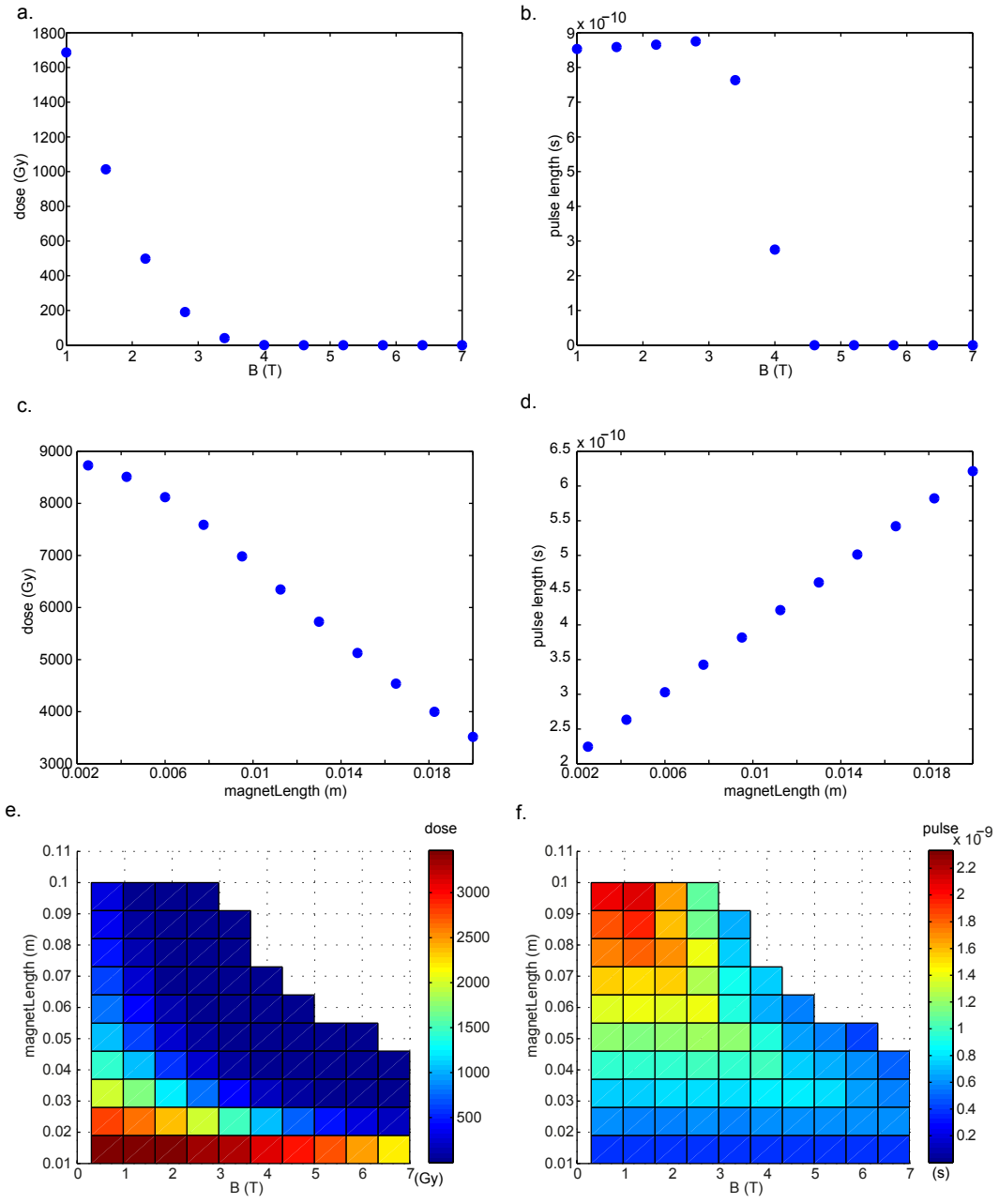

Figure 51: a. Dose decreases exponentially as a function of the magnetic field strength. **b.** With such a large pinhole, no apparent pulse dependency can be seen up to magnet strength of 3 T, after which pulse decreases rapidly by eliminating the low energy protons from detection. **c.** Dose dependency on the length of the magnet along the z-axis. **d.** Pulse length dependency on magnet length. **e.** Dose projection varying pinhole length and radius simultaneously. **f.** Pulse length projection varying pinhole length and radius simultaneously.

3.2 SINGLE TILTED PINHOLE

A titled pinhole is now tested under the same initial conditions as before though now with a smaller pinhole and much higher magnetic field. The setup parameters are shown in Table 13. The geometry of the second pinhole is placed at the same position on the z-axis i. e. is also the same length, however it starts slightly lower than it ends so as to take advantage of the angle at which the particles exit the magnet. In this way the efficiency can obviously be improved however the cost at which it is attained must be determined by examining the effects on the pulse duration.

Table 13: Input variables common to both setups in the simulation.

PARAMETER	QUANTITY
$\|\|\vec{B}\|\|$	6 T
$\vec{B}$ length	$3 \cdot 10^{-}2$ m
drift 1	$1 \cdot 10^{-}3$ m
drift 2	$1 \cdot 10^{-}3$ m
pinhole length	$5 \cdot 10^{-}3$ m
pinhole radius	$0.25 \cdot 10^{-}3$ m

3.2.1 *Drift space dependence*

Like the straight pinhole setup the effect of an increasing drift space now for a tilted pinhole is shown in Figure 52. A similar relationship is also deduced by lengthening the first drift space. The pulse length steadily increases for increasing drift space so that the order of magnitude gained by bringing the would-be cells close to the target is lost if the drift is increased too much. The argument to reduce dose by lengthening the drift space is weak as the gains made in reducing the dose are still inadequate for a cell irradiation.

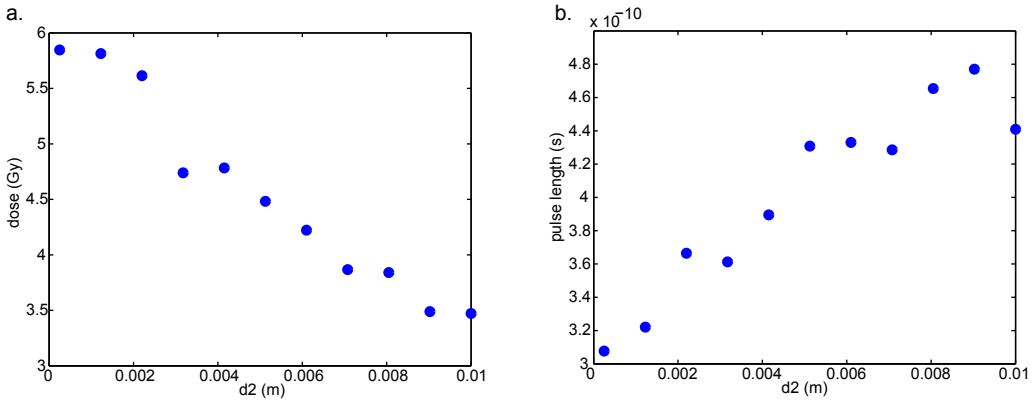

Figure 52: As for the straight pinhole setup, lengthening the pinhole will optimise the dose delivered to the cells but lengthen the pulse duration we seek to reduce. **a.** Second drift space influence on the dose. **b.** Second drift space influence on the pulse length.

3.2.2 *Pinhole dependence*

As for the straight pinhole setup, increasing the pinhole length reduces the dose as shown in (a-b). However this time it also has a positive effect on the pulse by reducing the duration by almost a magnitude in comparison to the straight pinhole. This is attributed to the magnet being 6x stronger now than for the straight pinhole setup so that the low energies are completely filtered out. The last point for a pulse length of $2.4 \cdot 10^{-10}$ s at 1 cm has particles in the 5 MeV energy bin, whereas at 5 mm, the lowest proton energy is in the 3 MeV energy bin.

By increasing the radius (Figure 53c-d), the dose and pulse length increase as expected, where a plateau is approached as the efficiency also approaches 100% for decreasing proton energies.

Pinhole length and radius are plotted together as the projection of a 3D plot in (e-f), where the smallest possible pinhole radius of 0.25 mm and length of 1.8 cm produces 0.5 Gy in dose and pulse duration $1 \cdot 10^{-10}$s.

3.2.3 *Magnetic field dependence*

The influence the magnetic field has on the detected particles can be seen from Figure 54 for an increasing magnetic field magnitude (a-b) and increasing magnet length (c-d) along the z-axis. The magnetic field affects the dose and pulse in a similar way as for the straight pinhole setup but this time the dose is not affected as drastically so that the full magnetic field strength range can be utilised. Increasing the magnetic field strength now yields a reduction in pulse duration not seen in the straight pinhole setup because the pinhole radius was still too large. Furthermore the pulse also decreases now as a function of magnet length for a high enough magnetic field as well as a small enough pinhole.

Figures (e-f) examine the relationship between the dose and pulse as a function of the magnet length and magnet strength in a surface plot. A dose of 1 Gy can be achieved at 6.5 T for a magnet length of 3-4 cm. This corresponds to a pulse duration of $3 \cdot 10^{-10}$ s, which is reduced only slightly more ($2 \cdot 10^{-10}$ s) for a magnet strength of 7 T delivering 0.5 Gy. Extending the magnet length longer than this for the same strength, starts to produces doses less than 1 Gy and the statistics of the simulation start to weaken. Alternatively a 2 T magnet with length 10 cm would also produce doses of 1 Gy, but at the expense of increasing pulse duration.

3.3 SUMMARY OF AN OPTIMISED SETUP

The best setup that could be found using these simulations involves the use of a tilted pinhole with the highest magnetic field possible (7 T) and the smallest pinhole possible (radius 0.25 mm). Under these conditions the magnetic field could only be a few centimetres (3 cm) long before no particles would reach the cells. A similar effect is also achieved by increasing the pinhole length for which a maximum length of 2 cm would allow a minimum dose and pulse. Under these conditions, the dose would be ~0.1 Gy and the pulse duration $1.2 \cdot 10^{-10}$ s. In the simulation, increasing the pinhole beyond this, no particles reached the end of the pinhole, however in an experiment, several orders of magnitude higher in particles emitted from the target can be expected and *may* produce pulses of the order of 10^{-11}s with detectable doses when the pinhole length is further increased. Since such a calculation would require weeks, this was not implemented, and so the optimised setup with the expected dose and pulse are

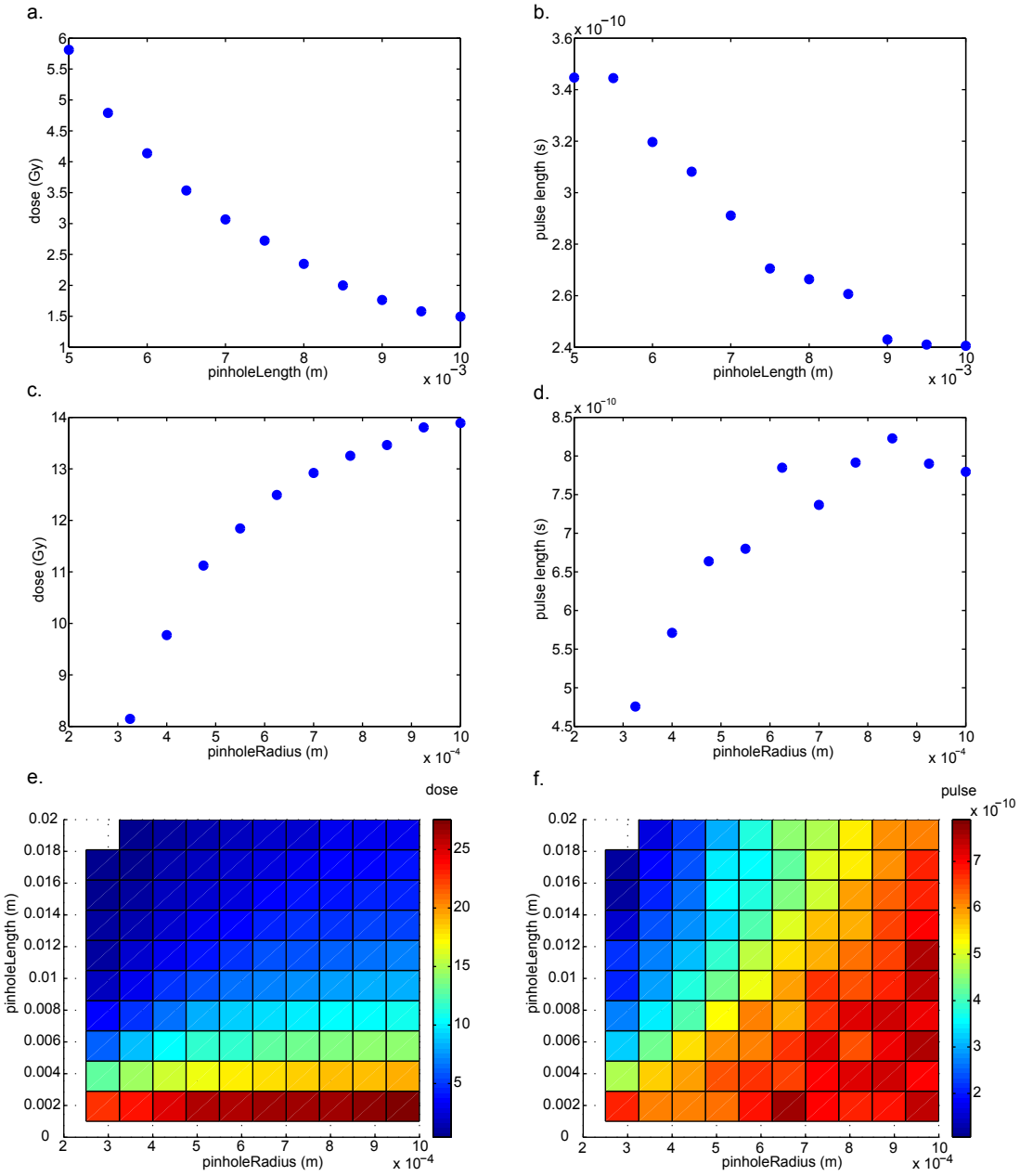

Figure 53: a. Dose decreases as a function of the pinhole length at a slower rate than that shown in Figure 50a. **b.** Extending the pinhole now reduces the pulse duration by excluding more of the lower energies. This relationship is not possible to produce at low magnetic fields for the same given length. **c.** The dose as a function of pinhole radius, is now several orders of magnitude less even with a large pinhole radius. **d.** Increasing the pinhole radius quickly includes more low energy protons so that the pulse increases. **e.** Dose projection varying pinhole length and radius simultaneously. Dose is several orders of magnitude less than the straight pinhole setup (Figure 50e) now because of the 6 T magnet. **f.** Pulse projection by varying pinhole length and radius simultaneously.

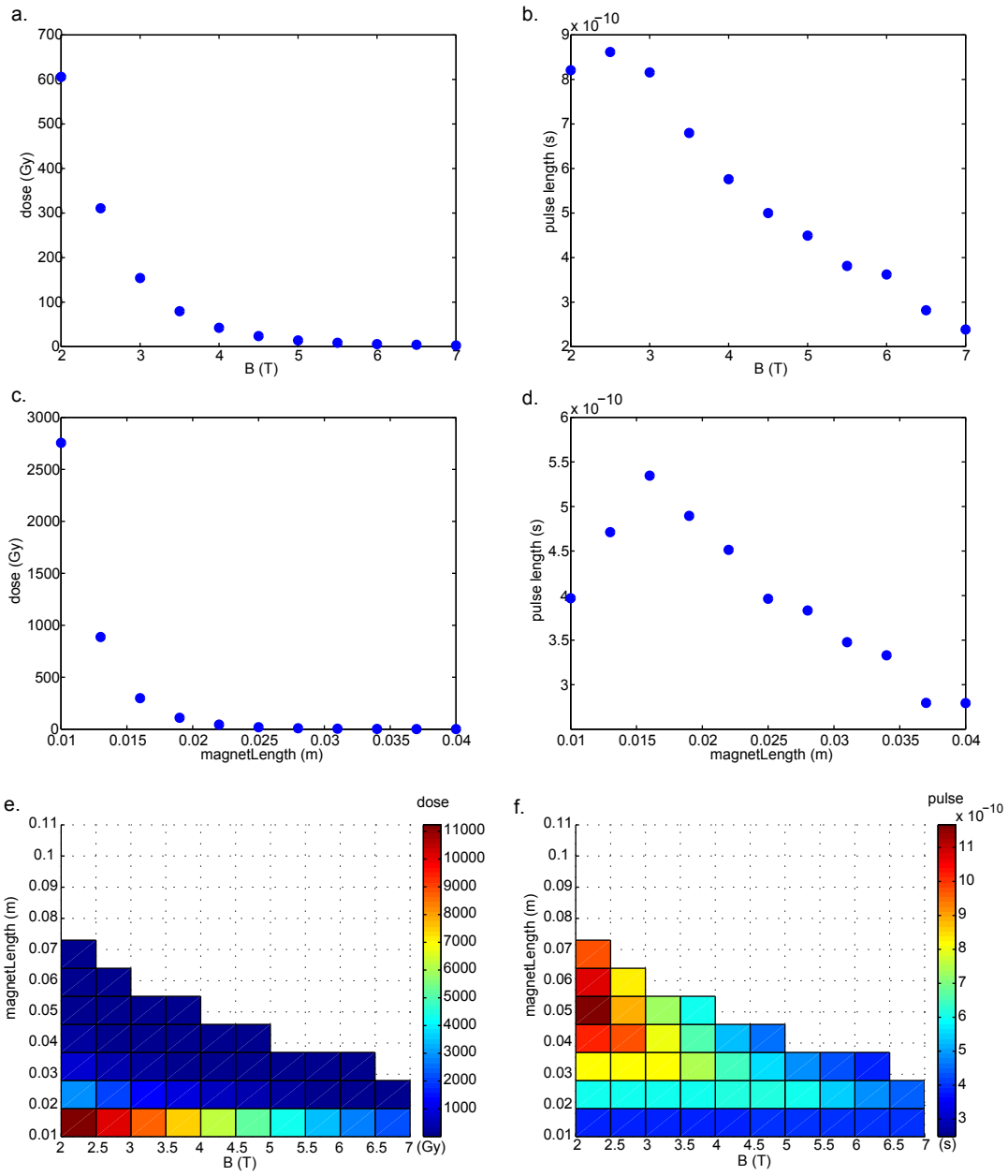

Figure 54: a. Decreasing dose as a function of increasing magnetic field magnitude. **b.** Pulse as a function of increasing magnetic field magnitude. **c.** Decreasing dose as a function of magnet length. Dose is non-zero with a minimum dose of 0.7 Gy for the longest magnet length. **d.** Pulse as a function of magnet length. **e.** Dose projection varying pinhole length and radius simultaneously. Dose ranges from 0.6-4 Gy at the maximum magnet lengths for each magnet strength before no more particles are detected in the simulation. **f.** Pulse projection varying pinhole length and radius simultaneously. Provided the magnet is stronger than 3 T, a reduced order of magnitude in pulse duration can be won.

only quoted from the results shown. Alternatively, a weaker magnet of 4 T can be introduced by using a straight pinhole setup to achieve pulse durations of the order 10^{-10}s and detectable dose levels. However permanent dipole magnets, as originally hoped are inadequate for adequate energy selection and thus pulse length reduction. Finally it is important that the magnet and cells are brought as close together as possible since any gap between these two segments will always increase the pulse length because of the angular divergence of protons emitted from the foil. This effect is not seen for increasing pinhole length provided the magnetic field is large enough because the pinhole walls will cut out those protons that arrive with large angles, whereas the drift space will simply allow the particles to drift further apart.

3.4 LASER SHOT VARIABILITY

All the results up to now have been produced with shot 1, which was the only spectrum available at the time. Later however an additional 10 spectra were given, which haven been plotted in Figure 55. The goal of this section was to determine the variation in the results calculated in the simulation due to the shot-to-shot variation of the laser. For the shots shown in Table 14, no distinct pattern can be observed between target thickness and maximum energy. The pinhole diameter is the same for all shots except the first, which affects the calculation of dose via Equation 59. In order to make a fair comparison of the endpoints (dose and pulse), the initial conditions as shown in Table 12 with a straight pinhole geometry were implemented for all 11 different shots to determine whether the results shown previously are a fair representation of what can be expected for future experiments. Comparing dose and pulse duration between shots 1-11, shots 2-11 would have an order of magnitude less in dose but comparable pulse duration. On the other hand, running the tilted pinhole setup with the parameters shown in Table 13, the dose stays relatively constant between shots (1.5-7 Gy) as does the pulse length ($3.5 - 4 \cdot 10^{-10}$s). The marked differences in dose variation can be explained by the tilted pinhole having a much higher magnet and smaller pinhole than was used in the straight pinhole setup. Because of this, more of the low-energy portion of the spectrum is admitted in the first setup whereas a high magnet strength as used in the second setup provides more energy separation so that the spectrum is mostly from the upper portion of the energy spectrum. Noting this and that the number of protons is relatively constant in this region therefore shows little shot-to-shot variability in dose and pulse when the magnet is high and a correspondingly small pinhole is used.

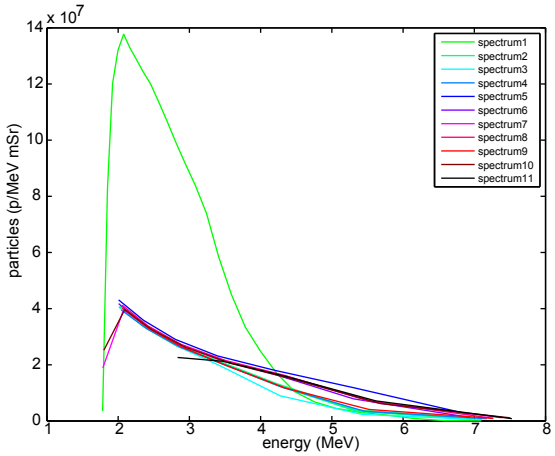

Figure 55: Spectra from the ATLAS laser where shot 1 has been used for the results up to this point. All the other shot data was acquired later and evidently has significantly less particles than the shot 1. Shots 2-11 generally differ little from each other.

Table 14: Laser shot diagnostics from ATLAS. The first shot has been used to produce all the results up to this point. Courtesy of Jianhui Bin.

SHOT NR.	TARGET THICKNESS (nm)	PINHOLE DIAMETER (mm)	MAX ENERGY (MeV)
1	40	2	7.1
2	20	8.5	7.0
3	20	8.5	7.1
4	40	8.5	7.2
5	20	8.5	6.9
6	20	8.5	6.9
7	40	8.5	7.4
8	20	8.5	7.3
9	40	8.5	7.3
10	40	8.5	7.5
11	40	8.5	7.5

4

DISCUSSION

The goal of this section was to simulate the ATLAS beam and minimise the pulse duration under feasible experimental conditions i. e. the dose should be of a reasonable level, the area large enough for adequate cell count and the magnetic field should be achievable. From the results shown here, the best way the pulse delivered to the cells can be minimised is by increasing the magnetic field and minimising the size of the pinhole. The magnetic field must be > 3 T regardless of whether a straight or tilted pinhole is used in order to bring the dose down to less than 50 Gy. Further increases in magnetic field reduce the pulse duration quickly so that a tilted pinhole is required to relax the angular requirements and thus maintain a detectable dose level. Permanent dipole magnets, as originally proposed are therefore inadequate to generate small pulses whilst maintaining a detectable dose level. The best case scenario provided by a high magnetic field produced over a short distance combined with a short length pinhole and small enough radius offers an order of magnitude smaller than what has previously been achieved in the laser-driven experiment [16] as well as those provided by the SNAKE beamline [9][115][114][146], none of which detected any biological difference between continuous and pulsed radiation.

By comparing Figures 51(e-f) and 54(e-f), increasing the magnitude of the magnetic field is much more important than the length, since although length can also add to energy separation of the broad spectrum, this effect is slower. Furthermore, it can add to the pulse length if the magnet strength is not high enough, as was tested in the straight pinhole setup with a 1 T magnet due to the angular spread of protons and all energies in the range being admitted. Provided the magnet is high enough (6-7 T), for the same magnet length, a decrease in pulse length occurs, because the low energy portion has already been cut from the spectrum and more protons are cut from the spectrum as the acceptance angle decreases. Whereas for lower magnet strengths, this effect occurs over a longer range so that the pulse continues to increase for the same length. Therefore to reduce the pulse length due to broad energy, a high magnetic field is required, and due to the angular distribution of protons emitted from the target, elongating the pinhole/magnet length will also reduce the pulse.

Although the two setups have not been compared with exactly the same conditions, the tilted pinhole is useful in maintaining a detectable dose level. If a weak magnet such as a permanent dipole magnet is used, this feature is not useful since the magnet does not provide enough energy selection. However for a very high magnet and small pinhole such a setup is preferred over the straight pinhole setup, which creates harder constraints on the acceptance angle of arriving protons.

In high dose rate experiments with laser-plasma xrays that no enhanced biological effect has been seen [59][119]. These studies however differ considerably to what has been simulated here since they are with pulsed xrays rather than charged particles, resulting in pulse durations delivered over the order of a few picoseconds. Hill et al. and Shinohara et al. differentiate though between the pulsed effect in time and space; the latter being claimed to be the more crucial to variances in biology. Furthermore Tillman et al.[124] found no biological difference existing between the pulsed radiation and conventional xrays, however as Shinohara et al. point out, this may be due to to the fact that the dose per pulse was so low (6.6 mGy/pulse) that the final dose rate was more like 4 Gy/min rather than the picoseconds used

by Shinohara et al. and Hill et al. To present two limiting cases with the conditions stated in Table 12, if a pulse over the order of picoseconds were to be delivered under the experimental conditions presented here, the beam would have to be monoenergetic, where the pulse duration would then come from the angular distribution. Conversely forcing all particles to enter at the zero axis i. e. $\alpha = \phi = 0$ rad but with an exponential energy distribution, a pulse duration of $\sim 10^{-10}$s would still ensue. As an intermediate and more likely situation, a quasi-monoenergetic beam with energy spread of 0.5 MeV as produced by Schwoere et al., would yield a pulse duration of $\sim 10^{-11}$s [117].

The simulation is limited by the equations of motion through the magnetic field given by Equations 44 and 45 that depend upon the length of the magnetic field and appropriate positioning of the pinhole. As such, particles exceeding the boundary conditions of arcsine were simply discarded and are no longer tracked. Additionally the small angle approximation has been used to obtain Equation 57. However for the geometry of the measured setup, this should be an appropriate assumption since the error in such an approximation is $5 \cdot 10^{-5}$%. Furthermore the surface area presented by the solid angle Ω is assumed to be a flat surface when it is slightly curved. This has been calculated for shot 1 and shows a difference in 0.1%, which is negligibly small. It is also assumed here that the number of particles ($1 \cdot 10^7$particles/shot) used was adequate to draw the statistical conclusions here. This claim is justified from the figures presented in the results that show clear correlations between the tested parameters and the endpoints we are interested in. Experimentally, this is likely to be several orders of magnitude more, however $1 \cdot 10^7$particles/shot was chosen for speed, which requires $\sim$ 10 minutes to produce data similar to that presented in Figure 49 thereby illustrating the usefulness of preparatory simulations like the one presented here.

The mechanisms for differences in damage induction for pulsed radiation - evident when the dose is delivered over a time scale significantly less than the time scale required for DSB repair mechanisms, which occur over an hour, can be explained by local oxygen depletion where it is assumed that due to the high dose rate, oxygen is depleted so rapidly that fixation of damage cannot occur - a mechanism responsible for *radioresistance* in hypoxic tumours Hall [53]. Alternatively it has been proposed that for high dose rates, no chance is afforded for the damage to occur due to reduced production and/or recombination of free radicals that are primarily responsible for damage of indirect forms of ionising radiation [54].

On the other side of the fence, these proposed mechanisms contrast with the hypothesis proposed by Fourkal et al. who assume that due to the clustering of particles, more energy is deposited resulting in a "collective excitation" of the irradiation target i. e. water [40] and therefore yielding *radiosensitivity*. This is also alluded to by Kreipl and Friedland who claim that although, the free radical production may indeed be reduced, increased spatial clustering will result in a higher probability of direct hit damage and greater biological effect [72].

It has been claimed that the most important effect is actually the spatial clustering of particles rather than the pulse duration [59][72][119]. This was demonstrated by Hill et al., who irradiated cells with laser-plasma ultrasoft xrays with the spatial properties of low LET radiation but the temporal properties of high LET radiation, which did not exhibit a disappearing oxygen effect typical of high LET radiation. This correlates well with the findings by Schmid et al., who found that by focusing protons down to micrometre spot sizes, a higher RBE can be seen [116].

Continuing along this line of thought, the detected particles at the end of the pinhole were also binned according to their energy so that the density of particles can be obtained by noting the efficiency of the system, the size of the pinhole and the pulse duration. According to Fourkal et al., a clustering of particles exceeding $\sim 10^{11}$ cm^{-3} is required to produce a

higher LET, which would be seen at around 10 cm from the target. For the data here, using the idealised case of a 4 T magnet and shot 1, the energy would range from $4.48 - 6.15$ MeV yielding a pulse duration of $1.9 \cdot 10^{-10}$ s. A quick calculation utilising an efficiency of 0.009%, for a pinhole radius of 1 mm, yields a particle density of $1 \cdot 10^{10}$ cm^{-3} with all other variables defined under the 'standard initial conditions' given in Table 12; this being slightly below the threshold distance of 10 cm. Therefore it is also possible that the spatial conditions required to witness an enhanced biological effect will also not be met under these conditions. However it would be interesting to test since the spatial requirements are close to those demanded despite the pulse duration not being much smaller than what has previously been achieved in pulsed particle experiments. Despite the proposed setup offering an order of magnitude less in pulse duration than studies already investigating pulsed charged particle irradiations, it is possible that it will still not be enough to provide the conditions necessary for an enhanced biological effect both on the time and spatial account. Considering that the conditions are so difficult to produce it is questionable whether this phenomenon holds any relevance in realistic experimental conditions.

If the energy distribution of laser-driven protons continues to be very broad, it is highly unlikely that an enhanced biological effect could be seen experimentally let alone in clinical practice, since doses would always be delivered over large source to patient distances (~1 m) in which case nanosecond delivery is most likely to be the case and the spatial clustering of the particles is lost. Therefore even if we see a higher biological effectiveness over shorter distances, such a situation is difficult to achieve even with high-gradient superconducting magnets and small pinholes. If the spectrum does indeed change to more monoenergetic as simulations in the RPA regime indicate, this could be a more likely situation than the current TNSA-presented situation however again, provided source to patient distances are long enough, the spatial clustering of particles would most likely vanish over a long enough distance.

Part VI

SUMMARY AND OUTLOOK

1

SUMMARY

The aim of this thesis was to investigate the biological properties of laser-driven protons in the first phase of pre-clinical development via cell irradiations. This was motivated by the fact that laser-driven protons arrive in temporally condensed and inhomogeneous bunches. Noting this and the high dose achievable within a single shot of the ATLAS laser, this thesis presents new methods adapted to such properties and investigates the hypothesis that pulsed protons produced by laser-driven technology interact via different biological mechanisms in comparison to those produced by conventional means.

This hypothesis was investigated using first two biological comparisons - experimental data from xrays and conventional protons - as well as via a simulation made at short distances to determine under what conditions the shortest pulse length can be delivered. After conducting the dosimetry with resolution equal to that of the size of the microscope FOV and biological analysis using standard approaches with xrays, it was decided that due to the inhomogeneous dose distribution presented by the laser, these approaches would no longer suffice. Therefore within the framework of this thesis, a novel method of automated assessment of biological damage was developed forming the basis upon which all conclusions are drawn from here. This has been approached on a biological level (DSBs represented by foci), via dosimetry (radiochromic EBT2 film calibration at low energies and image registration), and offers ideas for future experiments that may expand our knowledge of pulsed radiobiological damage. An initial estimation of the RBE of laser-driven protons was first deduced to be 1.3 ± 0.3. Due to the uncertainty being so large, we sought to reduce it in three different areas: mostly eliminate the subjectiveness associated with manual counting of γH2AX and 53BP1 foci; reduce the dose uncertainty due to image registration from 8% to 3%; and reduce the uncertainty in absolute dosimetry from 20% to 10%. Owing to these adjustments, a new comparison was made between the laser-driven protons and the tandem accelerator protons.

The first uncertainty is addressed in Part II; implemented on an individual cell basis due to non-negligible dose inhomogeneities on the cellular scale. The workflow is a three step process: cell contouring, parameter determination and automated foci detection. The cell contouring method presented here is semi-automated, argued to be necessary so as to thoroughly eliminate overlapping cells, cells incompletely shown in the image and mitotic cells; the latter of which no segmentation algorithm can account for. Parameter determination was a key factor missing from an automated method of foci counting since the tool in principle was there but not the necessary means to use it. Thus it is claimed here that in order to automate foci counting with FociPicker_3D, the essential requirements are only volume and range of pixel intensities that comprise a focus, where pixel intensity range was determined using the relation given in Equation 13 and the former via an inversion analysis resulting in Equation 15. Thus Part II presents a method that is fast and accurate to the extent that the results here are reproducible, unlike the gold standard of manual counting, which is completely user-dependent. Though this method was developed within the context of laser-driven technology, it is also likely to be useful in foci analysis when dose inhomogeneity across the microscope FOV in general is suspected. Although a number of methods have been developed to automatically assess γH2AX and 53BP1 foci induction, to my knowledge none are able to adequately distinguish foci in 3D. Ivashkevich et at. have a pseudo automated foci analysis in 3D based

on non-overlapping regions in the z-plane. They argue, however, that 3D counting was not performed in their analysis since it is difficult to verify visually [64]. Vandersickel et al. also mention a corrected foci analysis based on 3D image information using the Metacyte software, though no details are provided of its implementation [129]. McVean et al. also provide a method of automated foci counting however this relies on image enhancement techniques [81]

Whereas the cell irradiations with laser driven protons conducted by Yogo et al. [139] and Kraft et al. [71] created a relatively homogeneous dose by rotating the sample halfway through irradiation time, Part III on the other hand describes an approach to accept the dose inhomogeneity and exploit this using a very precise image registration. This is first performed to a precision comparable to that on the scale of a microscope FOV (dose uncertainty 8%) and later refined to that on a cellular level (dose uncertainty 3%). This method is therefore comparable to Fiorini et al. who also collected doses from differing regions in the beam to form a complete dose response however theirs was carried out using good agreement (5%) between simulated proton spectra and experimental proton spectra on film stacks [39]. To truly examine the effect of pulsed radiation, such high precision approaches are necessary so as to deliver dose in a single shot.

The final essential component to reducing error relates to the dosimetry where here an LET dependence can be seen in EBT2 film within the expected range delivered by the laser. Determining a calibration curve for 3.2 MeV protons as shown in Part IV showed an under-response in film of 26% when compared to the response of 10.6 MeV protons. This was performed using two films where the upstream film was used as a reference dosimeter at 10.6 MeV. With the calibration presented here a lower limit of 10% accuracy was achieved; being attributable to variations in fit, film batch variations and beam fluctuations, none of which here, can be reduced any further.

When considering the higher relative effect of laser-driven protons compared to tandem accelerator protons, the distribution of foci volume must be taken into account. This turns out to be critical when making comparisons in 2D since such large variances exist in the distribution of volume between experiment types as shown in Part IV. When this is accounted for as a 3D dose response does, the foci induced by laser-driven protons can be seen to vary from tandem accelerator protons to yield a relative effect of 1.5 ± 0.2 and 1.4 ± 0.2 for γH2AX and 53BP1 respectively, as well as a volume more than double the tandem accelerator proton-induced foci; features for which no satisfying answer exists yet. We can rule out the possibility of varied experimental conditions in the biological preparations such as washing, staining etc. by comparing control cells between pulsed and continuous data sets. Since a visual comparison, as well as the volume analysis presented in Section 3.3.1, yield virtually indistinguishable differences, it can be concluded that differences between foci in the irradiated cells are owing to physical properties of the protons themselves. This may be approached from two aspects: the beam is perhaps more heterogeneous in LET than we expected or the bunching does indeed have a different effect in comparison to when no bunching is delivered. As a suggestion, the energy of the beam along the line profile is simulated to vary from 3.5 - 7 MeV; corresponding to an LET of 10.4 - 6 keV/μm. It is, however, possible that the shot-to-shot fluctuation in the beam meant that the assumed energy ($3.2\pm$ 0.24 MeV) delivered to the cells was lower, in which case the LET would be higher. Alternatively according to the registration error, recording images slightly below the line focus corresponds to lower energies, which could also increase the average dose delivered to a number of cells. Thus further improvements in the laser shot-to-shot variability are likely to improve dosimetry and its respective error, though if we continue to use EBT2 film, an inherent uncertainty of 10% nevertheless exists.

To examine the biological effect with a pulse duration several orders of magnitude less than what has already been shown, Part V demonstrates that generating sub nanosecond pulses using simply a magnet and pinhole at short distances between target and cells requires careful consideration due to the energy spectrum being so broad from the laser. With such a spectrum, superconducting magnets combined with a small pinhole (of radius 0.5 mm) are necessary in order to achieve, at best, one order of magnitude less in pulse duration than what has been tested with the setup shown here. The pulse length arises firstly and primarily due to the broad energy spectrum, but also due to the angular distribution with which the protons are accelerated out of the target. Further refinements in the setup are likely to improve on these estimates; however I see the major advances coming from developments in laser technology rather than what is achievable at the end portion of the beamline. Whether these pulsed conditions in time are able to replicate the effects of other high LET experiments with protons remains to be seen [116].

2 OUTLOOK

The outlook for laser-driven technology for therapeutic use can be viewed by tracing its brief history: its beginnings started out with electron cell irradiation experiments [13], followed by proton cell irradiations as shown here and elsewhere [35] [71] [139], and most recently mouse experiments with electrons [88]; the limiting factor being an increase in energy. Given the rapid advances made thus far, it is likely that mouse irradiations with laser-driven protons are not far away. Clinical implementation though will require considerably more time. Concerning the original question as to whether laser-driven protons can be implemented without altering our current understanding of biology, all experiments to date show little to no biological difference of laser-driven protons. Furthermore it is questionable whether this has any clinical relevance since dose will likely be delivered over multiple shots over a large target to patient distance (~1 m). However, that is not to say that the experiments here have not opened up doors to future investigation - the limits of pulsed proton irradiation are yet to be experimentally demonstrated and the mechanisms as to why laser-driven foci are bigger than other radiation types, or even why they should induce a slightly greater biological effect compared to conventional protons, is yet to be explained. Understanding the biological properties of laser-driven protons is not yet exhausted and this thesis shows a technology very much in an early phase, setting the stage for an interesting future.

Part VII

APPENDIX

A

TRIM CALCULATION OF ENERGY DEGRADATION

The TRIM calculation of energy loss throughout successive layers in the continuous proton irradiation was performed using the settings shown in Table A1.a. Each layer can either be taken from a table of common compounds such as Mylar, however as stated in the program, the densities are not very accurate, thus for this current simulation some modifications were made to the densities. For more obscure data such as the active layer of the film, these need to manually composed, which can be done by adding successive elements. The stoichiometry values were calculated from the atomic composition of the corresponding layer given in the product description. The simulation was performed using 5000 particles with an initial energy of 11.1 MeV.

Table A1.a: Respective layer thicknesses and corresponding densities of proton energy degradation. Simulations were carried out with SRIM using the above settings.

	MATERIAL	THICKNESS (μm)	DENSITY (g/cm^3)	ATOMIC STOICHIOMETRY
WINDOW	Kapton	7.5	1.42	
	air	3000	1.2E-03	
EBT2 FILM	Mylar	50	1.35	
	adhesive	25	1.2	H=11, C=6.4, O=1.8
	top coat	5	1.2	H=7, C=3.2, O=7
	active layer	30	1.2	H=10.5, C=5.3, O=1.9
	Mylar	175	1.35	
DEGRADER	Aluminium	400	2.7	
CELL WINDOW	Mylar	6	1.35	
	air	3000	1.2E-03	

B

IMAGE REGISTRATION ERROR CALIBRATION

To calibrate the pixel uncertainty of the process outlined in the experimental methods section, the film image was used as both input and base image with the control point selection tool in MATLAB. This way it was possible to precisely select the amount by which the lengths l_{12} and l_{23} across the images. The percentage difference between input and base image over l_{12} and l_{23} was calculated as a function of pixel numbers according to Equation 18.

Table A2.b: Point 3 pixel error as a function of difference in relative length.

PIXEL SHIFT	ΔWEST (%)	ΔEAST(%)	ΔNORTH (%)	ΔSOUTH(%)	AVERAGE (%)
Δ0	0.099	0.083	0.040	0.058	0.070
Δ1	0.235	0.095	0.236	0.106	0.168
Δ2	0.464	0.303	0.383	0.265	0.354
Δ3	0.588	0.451	0.589	0.417	0.511

Table A2.c: Point 2 pixel error as a function of difference in relative length.

PIXEL SHIFT	ΔWEST (%)	ΔEAST (%)	ΔNORTH (%)	ΔSOUTH(%)	AVERAGE (%)
Δ0	0.007	0.009	0.024	0.007	0.012
Δ1	0.348	0.347	0.012	0.023	0.183
Δ2	0.643	0.620	0.017	0.010	0.322
Δ3	0.988	0.938	0.012	0.009	0.487

Table A2.d: Point 1 pixel error as a function of difference in relative length.

PIXEL SHIFT	ΔWEST (%)	ΔEAST (%)	ΔNORTH (%)	ΔSOUTH (%)	AVERAGE (%)
Δ0	0.031	0.017	0.024	0.040	0.028
Δ1	0.185	0.104	0.140	0.211	0.160
Δ2	0.314	0.227	0.288	0.383	0.303
Δ3	0.465	0.404	0.454	0.523	0.461

Table A2.e: Pixel error as a function of relative length difference averaged out over all three points comprising Figure 29.

PIXEL SHIFT	POINT 1 (%)	POINT 2 (%)	POINT 3 (%)	AVERAGE (%)
$\Delta 0$	0.07	0.01	0.03	0.04
$\Delta 1$	0.17	0.18	0.16	0.17
$\Delta 2$	0.35	0.32	0.30	0.33
$\Delta 3$	0.51	0.49	0.46	0.49

BIBLIOGRAPHY

[1] *The Molecular Probes Handbook - A Guide to Fluorescent Probes and Labeling Technologies*, Invitrogen - Life Technologies, 2011. www.invitrogen.com.

[2] *Cyanine dyes: Cy3, cy5 and others*, tech. report, ATDBio Ltd., accessed July 2013. http://www.atdbio.com/content/32/Cyanine-dyes-Cy3-Cy5-and-others.

[3] M. Abramowitz, B. Herman, D. B. Murphy, and M. W. Davidson, *Anatomy of the fluorescence microscope*, 06 2013. http://micro.magnet.fsu.edu/primer/.

[4] M. Abramowitz, K. R. Spring, H. E. Keller, and M. W. Davidson, *Basic principles of microscope objectives*, BioTechniques, 33 (2002), pp. 772–81.

[5] D. A. Agard, *Optical sectioning microscopy: Cellular architecture in three dimensions*, Annual Review of Biophysics and Bioengineering, 13 (1984), pp. 191–219.

[6] G. Angellier, M. Gautier, and J. Herault, *Radiochromic EBT2 film dosimetry for low-energy proton therapy*, Medical Physics, 38 (2011), pp. 6171–77.

[7] B. Arjomandy, R. Tailor, A. Anand, N. Sahoo, M. Gillin, K. Prado, and M. Vicic, *Energy dependence and dose response of gafchromic EBT2 film over a wide range of photon, electron, and proton beam energies*, Medical Physics, 37 (2010), pp. 1942–47.

[8] F. H. Attix, *Introduction to Radiological Physics and Radiation Dosimetry*, Wiley-VCH, 2004.

[9] S. Auer, V. Hable, C. Greubel, G. Drexler, T. Schmid, C. Belka, G. Dollinger, and A. A. Friedl, *Survival of tumor cells after proton irradiation with ultra-high dose rates*, Radiation Oncology, 6 (2011), pp. 139–47.

[10] P. Barber, R. J. Locke, G. P. Pierce, K. Rothkamm, and B. Vojnovic, *Gamma-H2AX Foci Counting: Image processing and control software for high-content screening*, Proceedings of SPIE, 6441 (2007), pp. 6441M1–10.

[11] M. J. Berger, J. S. Coursey, M. A. Zucker, and J. Chang, *Stopping-Power and Range Tables for Electrons, Protons, and Helium Ions*. http://www.nist.gov/pml/data/star/index.cfm.

[12] R. J. Berry, *Effects Of Radiation Dose-Rate From Protracted, Continuous Irradiation to Ultra-High Dose-Rates from Pulsed Accelerators*, British Medical Bulletin, (1978).

[13] E. Beyreuther, W. Enghardt, M. Kaluza, L. Karsch, L. Laschinsky, E. Lessmann, M. Nicolai, J. Pawelke, C. Richter, R. Sauerbrey, H. P. Schlenvoigt, and M. Baumann, *Establishment of technical prerequisites for cell irradiation experiments with laser-accelerated electrons*, Medical Physics, 37 (2010), pp. 1392–1400.

[14] E. Beyreuther, E. Lessmann, J. Pawelke, and S. Piek, *DNA double-strand break signalling: X-ray energy dependence of residual co-localised foci of γ-H2AX and 53BP1*, International Journal of Radiation Biology, 85 (2009), pp. 1042–50.

[15] A. Bieniek, A.and Moga, *An efficient watershed algorithm based on connected components*, Pattern Recognition, 33 (2000), pp. 907–16.

[16] J. Bin, K. Allinger, W. Assmann, G. Dollinger, G. A. Drexler, A. A. Friedl, D. Habs, P. Hilz, R. Hoerlein, N. Humble, S. Karsch, K. Khrennikov, D. Kiefer, F. Krausz, W. Ma, W. Michalski, M. Molls, S. Raith, S. Reinhardt, B. Röper, T. E. Schmid, T. Tajima, J. Wenz, O. Zlobinskaya, J. Schreiber, and J. J. Wilkens, *A laser-driven nanosecond proton source for radiobiological studies*, Applied Physics Letters, 101, 243701 (2012).

[17] J. H. Bin, W. J. Ma, K. Allinger, H. Y. Wang, D. Kiefer, S. Reinhardt, P. Hilz, K. Khrennikov, S. Karsch, X. Q. Yan, F. Krausz, T. Tajima, D. Habs, and J. Schreiber, *On the small divergence of laser-driven ion beams from nanometer thick foils*, Physics of Plasmas, 20, 073113 (2013).

[18] W. Böcker and G. Iliakis, *Computational Methods for Analysis of Foci: Validation for Radiation-Induced γH2AX Foci in Human and Cells*, Radiation Research, 165 (2006), pp. 113–24.

[19] R. H. Boggs, *The comparative value of radium and roentgen radiation*, Minnesota Medicine, 2 (1910), pp. 77–78. cited in https://en.wikipedia.org/wiki/History_of_radiation_therapy.

[20] S. Bolte and F. P. Cordelières, *A guided tour into subcellular colocalization analysis in light microscopy*, Journal of Microscopy, 224 (2006), pp. 213–32.

[21] W. M. Bonner, C. E. Redon, J. S. Dickey, A. J. Nakamura, O. A. Sedelnikova, S. Solier, and Y. Pommier, *γ-H2AX and cancer*, Nature Reviews Cancer, 8 (2008), pp. 957–67.

[22] M. Borghesi, S. Kar, and D. Margarone, *Laser-ion accelerators: State-of-the-art and scaling laws*, AIP Conference Proceedings, 1546 (2013), pp. 3–8.

[23] S. S. Bulanov, S. V. Bulanov, G. Turchetti, J. Limpouch, O. Klimo, J. Psikal, P. Antici, D. Margarone, and G. Korn, *Advanced geometries and regimes*, AIP Conference Proceedings, 1546 (2013), pp. 9–25.

[24] S. V. Bulanov, E. Y. Echkina, T. Z. Esirkepov, I. N. Inovenkov, M. Kando, F. Pegoraro, and G. Korn, *Unlimited ion acceleration by radiation pressure*, Physical Review Letters, 104 (2010), p. 135003.

[25] M. J. Butson, T. Cheung, and P. K. Yu, *Weak energy dependence of EBT gafchromic film dose response in the 50kVp-MVp X-ray range*, Applied Radiation and Isotopes, 64 (2006), pp. 60–2.

[26] Z. Cai, K. A. Vallis, and R. M. Reilly, *Computational analysis of the number, area and density of γ − H2AX foci in breast cancer cells exposed to 111In-DTPA-hEGF or γ—rays using Image-J software*, International Journal of Radiation Biology, 85 (2009), pp. 262–71.

[27] A. E. Carpenter, T. R. Jones, M. R. Lamprecht, C. Clarke, K. I. H., O. Friman, D. A. Guertin, J. H. Chang, R. A. Lindquist, J. Moffat, P. Golland, and D. M. Sabatini, *Cellprofiler: image analysis software for identifying and quantifying cell phenotypes.*, Genome Biology, 7 (2006), p. R100.

[28] S. T. Chiu-Tsao, Y. Ho, R. Shankar, L. Wang, and L. B. Harrison, *Energy dependence of response of new high sensitivity radiochromic films for megavoltage and kilovoltage radiation energies*, Medical Physics, 32 (2005), pp. 3350–54.

[29] M. E. Cooper, *Fluorescent probes for biological applications: Cyanine dyes revisited.* web. http://www.gelifesciences.com/.

[30] O. Dann, G. Bergen, E. Demant, and G. Volz, *Trypanocide Diamidine des 2-Phenyl-benzofurans, 2-Phenyl-indens und 2-Phenyl-indols*, Justus Liebigs Annalen der Chemie, 749 (1971), pp. 68–89.

[31] G. Datzmann, G. Dollinger, G. Hinderer, and H.-J. Körner, *A superconducting multipole lens for focusing high energy ions*, Nuclear Instruments and Methods in Physics Research Section B: Beam Interactions with Materials and Atoms, 158 (1999), pp. 74–80.

[32] G. Delaney, S. Jacob, C. Featherstone, and M. Barton, *The role of Radiotherapy in Cancer Treatment*, Cancer, 104 (2005), pp. 1129–37.

[33] T. F. DeLaney, *Proton therapy in the clinic*, Frontiers of Radiation Therapy and Oncology, 42 (2011), pp. 465–85.

[34] G. Dollinger, A. Bergmaier, V. Hable, R. Hertenberger, C. Greubel, A. Hauptner, and P. Reichart, *Nanosecond pulsed proton microbeam*, Nuclear Instruments and Methods in Physics Research Section B: Beam Interactions with Materials and Atoms, 267 (2009), pp. 2008–12.

[35] D. Doria, K. F. Kakolee, S. Kar, S. K. Litt, F. Fiorini, H. Ahmed, S. Green, J. C. G. Jeynes, J. Kavanagh, D. Kirby, K. J. Kirkby, C. L. Lewis, M. J. Merchant, G. Nersisyan, R. Prasad, K. M. Prise, G. Schettino, M. Zepf, and M. Borghesi, *Biological effectiveness on live cells of laser driven protons at dose rates exceeding 10^9 Gy/s*, AIP Advances, 2, 011209 (2012).

[36] G. Du, *FociPicker3D: 3D and 2D particle counter*. http://rsbweb.nih.gov/ij/plugins/focipicker3d/, April 2010.

[37] G. Du, G. A. Drexler, W. Friedland, C. Greubel, V. Hable, R. Kruecken, A. Kugler, L. Tonelli, A. A. Friedl, and G. Dollinger, *Spatial Dynamics of DNA Damage Response Protein Foci along the Ion Trajectory of High-LET Particles*, Radiation Research, 176 (2011), pp. 706–15.

[38] T. Esirkepov, M. Borghesi, S. V. Bulanov, G. Mourou, and T. Tajima, *Highly efficient relativistic-ion generation in the laser-piston regime*, Physical Review Letters, 92, 175003 (2004).

[39] F. Fiorini, D. Kirby, M. Borghesi, D. Doria, J. C. G. Jeynes, K. F. Kakolee, S. Kar, S. Kaur, K. J. Kirby, M. J. Merchant, and S. Green, *Dosimetry and spectral analysis of a radiobiological experiment using laser-driven proton beams*, Physics in Medicine and Biology, 56 (2011), pp. 6969–82.

[40] E. Fourkal, I. Velchev, C. Ma, and J. Fan, *Linear energy transfer of proton clusters*, Physics in Medicine and Biology, 56 (2011), pp. 3123–36.

[41] J. Fuchs, P. Antici, E. D'Humieres, E. Lefebvre, M. Borghesi, E. Brambrink, C. A. Cecchetti, M. Kaluza, V. Malka, M. Manclossi, S. Meyroneinc, P. Mora, J. Schreiber, T. Toncian, H. Pepin, and P. Audebert, *Laser-driven proton scaling laws and new paths towards energy increase*, Nature Physics, 2 (2006), pp. 48–54.

[42] S. A. Gaillard, T. Kluge, K. A. Flippo, M. Bussmann, B. Gall, T. Lockard, M. Geissel, D. T. Offermann, M. Schollmeier, Y. Sentoku, and T. E. Cowan, *Increased laser-accelerated proton energies via direct laser-light-pressure acceleration of electrons in microcone targets*, Physics of Plasmas, 18, 056710 (2011).

[43] B. I. Gerashchenko and J. R. Dynlacht, *A Tool For Enhancement and Scoring of DNA Repair Foci*, Cytometry Part A, 75A (2008), pp. 245–52.

[44] P. Gibbon, *Short Pulse Laser Interactions with Matter: An Introduction*, World Scientific Publishing Company, 2005.

[45] M. Goitein, *Trials and tribulations in charged particle radiotherapy*, Radiotherapy and Oncology, 95 (2010), pp. 23–31.

[46] M. Goitein and M. Jermann, *The relative costs of proton and x-ray radiation therapy*, Clinical Oncology, 15 (2003), pp. S37–50.

[47] R. Gonzalez and R. Woods, *Digital Image Processing*, Pearson International Edition, 2008.

[48] B. Gottschalk, *Physics of proton interactions in matter*, in Proton Therapy Physics, H. Paganetti, ed., Taylor & Francis, 2012.

[49] C. Greubel, W. Assmann, C. Burgdorf, G. Dollinger, G. Du, V. Hable, A. Hapfelmeier, R. Hertenberger, P. Kneschaurek, D. Michalski, M. Molls, S. Reinhardt, B. Röper, S. Schell, T. E. Schmid, C. Siebenwirth, T. Wenzl, O. Zlobinskaya, and J. J. Wilkens, *Scanning irradiation device for mice in vivo with pulsed and continuous proton beams*, Radiation and Environmental Biophysics, (2011), pp. 1–6.

[50] H. Gustavsson, S. A. J. Bäck, J. Medin, E. Grusell, and L. E. Olsson, *Linear energy transfer dependence of a normoxic polymer gel dosimeter investigated using proton beam absorbed dose measurements*, Physics in Medicine and Biology, 49 (2004), pp. 3847–55.

[51] T. Haberer, J. Debus, H. Eickhoff, O. Jäkel, D. Schulz-Ertner, and U. Weber, *The Heidelberg Ion Therapy Center*, Radiotherapy and Oncology, 73 (2004), pp. S186–90.

[52] V. Hable, *Echtzeitbeobachtung schneller Reaktionskinetiken in lebeden Zellen nach lonenmikrobestrahlung*, PhD thesis, Universität der Bundeswehr München, 2010.

[53] E. J. Hall, *Radiation Dose-Rate: A Factor of Importance in Radiobiology and Radiotherapy*, British Journal of Radiology, 45 (1972), pp. 81–97.

[54] E. J. Hall and A. M. Giaccia, *Radiobiology For The Radiologist*, Lippincott Williams & Wilkins, 2006.

[55] A. Henig, *Advanced Approaches to High Intensity Laser-Driven Ion Acceleration*, PhD thesis, Ludwig-Maximilians-Universität München, 2010.

[56] A. Henig, D. Kiefer, K. Markey, D. C. Gautier, K. A. Flippo, S. Letzring, R. P. Johnson, T. Shimada, L. Yin, B. J. Albright, K. J. Bowers, J. C. Fernández, S. G. Rykovanov, H.-C. Wu, M. Zepf, D. Jung, V. K. Liechtenstein, J. Schreiber, D. Habs, and B. M. Hegelich, *Enhanced Laser-Driven Ion Acceleration in the Relativistic Transparency Regime*, Physical Review Letters, 103, 045002 (2009).

[57] L. Hernández, M. Terradas, M. Martín, L. Tusell, and A. Genescá, *Highly Sensitive Automated Method for DNA Damage Assessment: Gamma-H2AX Foci Counting and Cell Cycle Sorting*, International Journal of Molecular Sciences, 14 (2013), pp. 15810–26.

[58] R. Hiemann, N. Hilger, J. Michel, J. Nitschke, A. Böhm, U. Anderer, M. Weigert, and U. Sack, *Automatic Analysis of Immunofluorescence Patterns of HEp-2 Cells*, Annals of the New York Academy of Sciences, 1109 (2007), pp. 358–71.

[59] M. Hill, D. L. Stevens, S. J. Marsden, R. Allott, I. C. E. Turcu, and D. T. Goodhead, *Is the increased relative biological effectiveness of high LET particles due to spatial or temporal effects? characterization and OER in v79-4 cells*, Physics in Medicine and Biology, 47 (2002), pp. 3543–55.

[60] G. Hinderer, G. Dollinger, G. Datzmann, and H. Körner, *Design of the new superconducting microprobe system in Munich*, Nuclear Instruments and Methods in Physics Research Section B: Beam Interactions with Materials and Atoms, 130 (1997), pp. 51–56.

[61] K. M. Hofmann, S. Schell, and J. J. Wilkens, *Laser-driven beam lines for delivering intensity modulated radiation therapy with particle beams*, Journal of Biophotonics, 5 (2012), pp. 903–11.

[62] Y. N. Hou, A. Lavaf, H. D., S. Peters, R. Huq, V. Friedrich, B. S. Rosenstein, and J. Kao, *Development of an Automated γ-H2AX Immunocytochemistry Assay*, Radiation Research, 171 (2009), pp. 360–67.

[63] P. V. C. Hough, *Method and means for recognizing complex patterns*, December 1962.

[64] A. N. Ivashkevich, O. A. Martin, A. J. Smith, C. E. Redon, W. M. Bonner, R. F. Martin, and P. N. Lobachevsky, *gamma H2AX foci as a measure of DNA damage: A computational approach to automatic analysis*, Mutation Research: Fundamental and Molecular Mechanisms of Mutagenesis, 711 (2011), pp. 49–60.

[65] N. Ji, J. C. Magee, and E. Betzig, *High-speed, low-photodamage nonlinear imaging using passive pulse splitters*, Nature Methods, 5 (2008), pp. 197–202.

[66] A. Jucha, A. Wegierek-Ciuk, Z. Koza, H. Lisowska, A. Wojcik, M. Wojewodzka, and A. Lankoff, *FociCounter: A freely available PC programme for quantitative and qualitative analysis of gamma-H2AX foci*, Mutation Research-Genetic Toxicology and Environmental Mutatgenesis, 696 (2010), pp. 16–20.

[67] J. Kapuscinski, *DAPI: a DNA-Specific Fluorescent Probe*, Biotechnic & Histochemistry, 70 (1995), pp. 220–33.

[68] S. Kar, K. F. Kakolee, B. Qiao, A. Macchi, M. Cerchez, D. Doria, M. Geissler, P. McKenna, D. Neely, J. Osterholz, R. Prasad, K. Quinn, B. Ramakrisna, G. Sarri, O. Willi, X. Y. Yuan, M. Zepf, and M. Borghesi, *Ion acceleration in multispecies targets driven by intense laser radiation pressure*, arXiv:1207.4288 [physics.plasm-ph], (2012).

[69] D. Kirby, S. Green, H. Palmans, R. Hugtenburg, C. Wojnecki, and D. Parker, *LET dependence of GafChromic films and an ion chamber in low-energy proton dosimetry*, Physics in Medicine and Biology, 55 (2010), pp. 417–33.

[70] T. Kluge, S. A. Gaillard, K. A. Flippo, T. Burris-Mog, W. Enghardt, B. Gall, M. Geissel, A. Helm, S. D. Kraft, T. Lockard, J. Metzkes, D. T. Offermann, M. Schollmeier, U. Schramm, K. Zeil, M. Bussmann, and T. E. Cowan, *High proton energies from cone targets: electron acceleration mechanisms*, New Journal of Physics, 14 (2012), p. 023038.

[71] S. Kraft, C. Richter, K. Zeil, M. Baumann, E. Beyreuther, S. Bock, M. Bussmann, T. E. Cowan, Y. Dammene, W. Enghardt, U. Helbig, L. Karsch, T. Kluge, L. Laschinsky, E. Lessmann, J. Metzkes, D. Naumburger, R. Sauerbrey, M. Schärer, M. Sobiella, J. Woithe, U. Schramm, and J. Pawelke, *Dose-dependent biological damage of tumour cells by laser-accelerated proton beams*, New Journal of Physics, 12, 085003 (2010).

[72] M. S. Kreipl, W. Friedland, and H. G. Paretzke, *Interaction of ion tracks in spatial and temporal proximity*, Radiation and Environmental Biophysics, 48 (2009), pp. 349–59.

[73] E. L. Leatherbarrow, J. V. Harper, F. A. Cucinotta, and P. O'Neill, *Induction and quantification of γ -H2AX foci following low and high LET-irradiation*, International Journal of Radiation Biology, 82 (2006), pp. 111–18.

[74] J. W. Lichtman and J.-A. Conchello, *Fluorescence microscopy*, Nature Methods, 2 (2005), pp. 910–19.

[75] P. Lindsay, A. Rink, M. Ruschin, and D. Jaffray, *Investigation of energy dependence of EBT and EBT-2 Gafchromic film*, Medical Physics, 37 (2010), pp. 571–76.

[76] W. Luo, E. Fourkal, J. Li, and C. M. Ma, *Particle selection and beam collimation system for laser-accelerated proton beam therapy*, Medical Physics, 32 (2005), pp. 794–806.

[77] W. Ma, V. Liechtenstein, J. Szerypo, D. Jung, P. Hilz, B. Hegelich, H. Maier, J. Schreiber, and D. Habs, *Preparation of self-supporting diamond-like carbon nanofoils with thickness less than 5 nm for laser-driven ion acceleration*, Nuclear Instruments and Methods in Physics Research Section A: Accelerators, Spectrometers, Detectors and Associated Equipment, 655 (2011), pp. 53–56.

[78] E. Marková, N. Schultz, and I. Y. Belyaev, *Kinetics and dose-response of residual 53BP1/γ-h2ax foci: Co-localization, relationship with DSB repair and clonogenic survival*, International Journal of Radiation Biology, 83 (2007), pp. 319–29.

[79] M. Martišíková and O. Jäkel, *Dosimetric properties of Gafchromic EBT films in monoenergetic medical ion beams*, Physics in Medicine and Biology, 55 (2010), pp. 3741–51.

[80] World Health Organisation, *Are the number of cancer cases increasing or decreasing in the world?* http://www.who.int/features/qa/15/en/index.html, 2008.

[81] A. McVean, S. Kent, A. Bakanov, T. Hobbs, and R. Anderson, *Development and validation of 'AutoRIF': software for the automated analysis of radiation-induced foci*, Genome Integrity, 3 (2012), pp. 1–13.

[82] M. Mistrik, L. Oplustilova, J. Lukas, and J. Bartek, *Low-dose DNA damage and replication stress responses quantified by optimized automated single-cell image analysis.*, Cell Cycle, 15 (2009), pp. 2592–99.

[83] M. Molls, C. Nieder, C. Belka, and J. Norum, *Quantitative Cell Kill of Radio- and Chemotherapy*, in The Impact of Tumor Biology on Cancer Treatment and Multidisciplinary Strategies, M. Molls, P. Vaupel, C. Nieder, and M. Anscher, eds., Medical Radiology: Diagnostic Imaging and Radiation Oncology, Springer, 2009, ch. 10, pp. 169–91.

[84] G. A. Mourou, T. Tajima, and S. V. Bulanov, *Optics in the relativistic regime*, Reviews of Modern Physics, 78 (2006), pp. 309–71.

[85] S. Mukherjee, *The Emporer of All Maladies: A Biography of Cancer*, Scribner, 2011. p. 170.

[86] D. Murphy, *Fundamentals of Light Microscopy and Electronic Imaging*, John Wiley & Sons, 2001.

[87] A. Nakamura, V. Rao, Y. Pommier, and W. Bonner, *The complexity of phosphorylated H2AX foci formation and DNA repair assembly at DNA double-strand breaks*, Cell Cycle, 9 (2010), pp. 389–97.

[88] M. Oppelt, M. Baumann, R. Bergmann, E. Beyreuther, K. Brüchner, J. Hartman, M. Kaluza, L. Karsch, M. Krause, L. Laschinsky, E. Lessmann, M. Nicolai, M. Reuter, A. Sävart, M. Schnell, M. Schürer, and J. Pawelke, *In vivo dose response studies at laser driven particle beams*, Experimentelle Strahlentherapie und Klinische Strahlenbiologie, 22 (2013), pp. 152–56.

[89] N. Otsu, *A Threshold Selection Method from Gray-level Histograms*, IEEE Transactions on Systems, Man and Cybernetics, 9 (1979), pp. 62–6.

[90] H. Paganetti, *Protons: Clinical considerations and applications*, in Monte Carlo Techniques in Radiation Therapy, J. Seco and F. Verhaegen, eds., Imaging in Medical Diagnosis and Therapy, Taylor & Francis, 2013, p. 203.

[91] N. Panchuk-Voloshina, R. P. Haugland, J. Bishop-Stewart, M. K. Bhalgat, P. J. Millard, F. Mao, W.-Y. Leung, and R. P. Haugland, *Alexa Dyes, a Series of New Fluorescent Dyes that Yield Exceptionally Bright, Photostable Conjugates*, Journal of Histochemistry & Cytochemistry, 47 (1999), pp. 1179–88.

[92] T. Pawlik and K. Keyomarsi, *Role of cell cycle in mediating sensitivity to radiotherapy*, International Journal of Radiation Oncology* Biology* Physics, 59 (2004), pp. 928–42.

[93] E. Pedroni, R. Bacher, H. Blattmann, T. Bohringer, A. Coray, A. Lomax, S. Linm, G. Munkel, S. Scheib, S. U., and A. Tourovsky, *The 200-MeV proton therapy project at the Paul Scherrer Institute: Conceptual design and practical realization*, Medical Physics, 22 (1995), pp. 37–53.

[94] F. Pfeiffer, T. Weitkamp, O. Bunk, and C. David, *Phase retrieval and differential phase-contrast imaging with low-brilliance X-ray sources*, Nature Physics, 2 (2006), pp. 258–61.

[95] A. Piermattei, R. Miceli, L. Azario, A. Fidanzio, S. delle Canne, C. De Angelis, S. Onori, M. Pacilio, E. Petetti, L. Raffaele, and M. G. Sabini, *Radiochromic film dosimetry of a low energy proton beam*, Medical Physics, 27 (2000), pp. 1655–60.

[96] E. Podgorsak, ed., *Radiation Oncology Physics: A Handbook for Teachers and Students*, IAEA, 2005.

[97] T. Puck, P. Sanders, and D. Petersen, *Life Cycle Analysis of Mammalian Cells: II. Cells from the Chinese Hamster Ovary Grown in Suspension Culture*, Biophysical Journal, 4 (1964), pp. 441–50.

[98] W. Rasband, *ImageJ, U. S. National Institutes of Health, Bethesda, Maryland, USA*, (1997-2012).

[99] S. Reinhardt, *Detection of laser-accelerated protons*, PhD thesis, Ludwig-Maximilians-Universität München, 2012.

[100] S. Reinhardt, C. Greubel, N. Humble, K. Parodi, J. J. Wilkens, and W. Assmann, *EBT2 and EBT3 film calibration for dosimetry of laser-accelerated protons in the 4 - 20 MeV energy range*, Radiation and Environmental Biophysics, (submitted).

[101] S. Reinhardt, M. Hillbrand, J. J. Wilkens, and W. Assmann, *Comparison of Gafchromic EBT2 and EBT3 films for clinical photon and proton beams*, Medical Physics, 39 (2012), pp. 5257–62.

[102] C. Richter, J. Pawelke, L. Karsch, and J. Woithe, *Energy dependence of EBT-1 radiochromic film response for photon (10 kVp–15 MVp) and electron beams (6–18 MeV) readout by a flatbed scanner*, Medical Physics, 36 (2009), pp. 5506–14.

[103] J. P. Robinson, J. Sturgis, and G. L. Kumar, *Immunohistochemical Staining Methods*, Dako, 5th ed., 2009.

[104] L. Robson, P. T. Simpson, R. J. Clarke, K. W. D. Ledingham, F. Lindau, O. Lundh, T. McCanny, P. Mora, D. Neely, C.-G. Wahlstrom, M. Zepf, and P. McKenna, *Scaling of proton acceleration driven by petawatt-laser-plasma interactions*, Nature Physics, 3 (2007), pp. 58–62.

[105] S. Roch-Lefévre, T. Mandina, P. Voisin, G. Gaëtan, J. E. González Mesa, M. Valente, P. Bonnesoeur, O. Garcia, P. Voisin, and L. Roy, *Quantification of gamma-H2AX Foci in Human Lymphocytes: A Method for Biological Dosimetry after Ionizing Radiation Exposure*, Radiation Research, 174 (2010), pp. 185–94.

[106] E. Rogakou, D. Pilch, A. Orr, V. Ivanova, and W. Bonner, *DNA double-stranded breaks induce histone H2AX phosphorylation on serine 139*, Journal of Biological Chemistry, 273 (1998), pp. 5858–68.

[107] R. Rottenfusser, E. E. Wilson, and M. W. Davidson, *Introduction to fluorescence microscopy*. Web, May 2013. http://zeiss-campus.magnet.fsu.edu/articles/basics/fluorescence.html.

[108] R. Runge, H. R., W. M., U. Kasten-Pisula, S. K., Z. K., F. C., R. D., W. G., C. K., and K. J., *Fully automated interpretation of ionizing radiation-induced γH2AX foci by the novel pattern recognition system AKLIDES*, International Journal of Radiation Biology, 88 (2012), pp. 439–47.

[109] P. Sarder and A. Nehorai, *Deconvolution methods for 3-D fluorescence microscopy images*, Signal Processing Magazine, IEEE, 23 (2006), pp. 32–45.

[110] S. Schell, *Dose delivery and treatment planning methods for efficient radiation therapy with laser-driven particle beams*, PhD thesis, Technische Universität München, 2011.

[111] S. Schell and J. J. Wilkens, *Advanced treatment planning methods for efficient radiation therapy with laser accelerated proton and ion beams*, Medical Physics, 37 (2010), pp. 5330–40.

[112] J. M. Schippers and A. J. Lomax, *Emerging technologies in proton therapy*, Acta Oncologica, 50 (2011), pp. 838–50.

[113] T. E. Schmid, G. Dollinger, W. Beisker, V. Hable, C. Greubel, S. Auer, A. Mittag, A. Tarnok, A. A. Friedl, M. Molls, and R. B., *Differences in the kinetics of γ-H2AX fluorescence decay after exposure to low and high LET radiation*, International Journal of Radiation Biology, (2010), pp. 682–91.

[114] T. E. Schmid, G. Dollinger, V. Hable, C. Greubel, O. Zlobinskaya, D. Michalski, S. Auer, A. A. Friedl, E. Schmid, M. Molls, and B. Röper, *The Effectiveness of 20 MeV Protons at Nanosecond Pulse Lengths in Producing Chromosome Aberrations in Human-Hamster Hybrid Cells*, Radiation Research, 175 (2011), pp. 719–27.

[115] T. E. Schmid, G. Dollinger, A. Hauptner, V. Hable, C. Greubel, S. Auer, A. A. Friedl, M. Molls, and B. Röper, *No Evidence for a Different RBE between Pulsed and Continuous 20 MeV Protons*, Radiation Research, 172 (2009), pp. 567–74.

[116] T. E. Schmid, C. Greubel, V. Hable, O. Zlobinskaya, D. Michalski, S. Girst, C. Siebenwirth, E. Schmid, M. Molls, G. Multhoff, and G. Dollinger, *Low LET protons focused to submicrometer shows enhanced radiobiological effectiveness*, Physics in Medicine and Biology, 57 (2012), pp. 5889–907.

[117] H. Schwoerer, S. Pfotenhauer, O. Jackel, K.-U. Amthor, B. Liesfeld, W. Ziegler, R. Sauerbrey, K. W. D. Ledingham, and T. Esirkepov, *Laser-plasma acceleration of quasi-monoenergetic protons from microstructured targets*, Nature, 439 (2006), pp. 445–48.

[118] Y. Sentoku, T. E. Cowan, A. Kemp, and H. Ruhl, *High energy proton acceleration in interaction of short laser pulse with dense plasma target*, Physics of Plasmas, 10 (2003), pp. 2009–15.

[119] K. Shinohora, H. Nakano, N. Miyazaki, M. Tago, and R. Kodama, *Effects of Single-pulse (< 1 ps) X-rays from Laser-produced Plasmas on Mammalian Cells*, Journal of Radiation Research, 45 (2004), pp. 509–14.

[120] D. Strickland and G. Mourou, *Compression of amplified chirped optical pulses*, Optics Communications, 56 (1985), pp. 219–21.

[121] H. Suit, H. Kooy, A. Trofimov, J. Farr, J. Munzenrider, T. DeLaney, J. Loeffler, B. Clasie, S. Safai, and H. Paganetti, *Should positive phase III clinical trial data be required before proton beam therapy is more widely adopted? No*, Radiotherapy and Oncology, 86 (2008), pp. 148–53.

[122] Z. Taheri-Kadkhoda, T. Bjork-Eriksson, S. Nill, J. J. Wilkens, U. Oelfke, K. A. Johansson, P. Huber, and M. Munter, *Intensity-modulated radiotherapy of nasopharyngeal carcinoma: a comparative treatment planning study of photons and protons*, Radiation Oncology, 3 (2008), p. 4.

[123] T. Tajima and J. Dawson, *Laser electron accelerator*, Physical Review Letters, 43 (1979), pp. 267–70.

[124] C. Tillman, G. Grafström, A. C. Jonsson, B. A. Jönsson, I. Mercer, S. Mattsson, S. E. Strand, and S. Svanberg, *Survival of mammalian cells exposed to ultrahigh dose rates from a laser-produced plasma x-ray source1*, Radiology, 213 (1999), pp. 860–65.

[125] H. C. Turner, D. J. Brenner, Y. Chen, A. Bertucci, J. Zhang, H. Wang, O. V. Lyulko, Y. Xu, I. Shuryak, J. Schaefer, N. Simaan, G. Randers-Pehrson, Y. L. Yao, S. A. Amundson, and G. Garty, *Adapting the gamma-H2AX Assay for Automated Processing in Human Lymphocytes. 1. Technological Aspects*, Radiation Research, 175 (2011), pp. 282–90.

[126] A. R. Urbach, *DNA complexes: Durable binders*, Nature Chemistry, 3 (2011), pp. 836–7.

[127] M. Valente, P. Voisin, P. Laloi, L. Roy, and S. Roch-Lefévre, *Automated gamma-H2AX focus scoring method for human lymphocytes after ionizing radiation exposure*, Radiation Measurements, 46 (2011), pp. 871–76.

[128] B. Valeur and M. N. Berberan-Santos, *Molecular Fluorescence: Principles and Applications*, Wiley-VCH, 2012.

[129] V. Vandersickel, J. Depuydt, B. Van Bockstaele, G. Perletti, J. Philippe, H. Thierens, and A. Vral, *Early increase of radiation-induced γH2AX foci in a human ku70/80 knockdown cell line characterized by an enhanced radiosensitivity*, Journal of Radiation Research, 51 (2010), pp. 633–41.

[130] S. M. Vatnitsky, R. W. M. Schulte, R. Galindo, H. J. Meinass, and D. W. Miller, *Radiochromic film dosimetry for verification of dose distributions delivered with proton-beam radiosurgery*, Physics in Medicine and Biology, 42 (1997), pp. 1887–98.

[131] W. Wallace, L. H. Schaefer, and J. R. Swedlow, *A working person's guide to deconvolution in light microscopy.*, BioTechniques, 31 (2001), pp. 1076–97.

[132] J. Widengren, A. Chmyrov, C. Eggeling, P.-Å. Löfdahl, and C. A. M. Seidel, *Strategies to Improve Photostabilities in Ultrasensitive Fluorescence Spectroscopy*, The Journal of Physical Chemistry A, 111 (2007), pp. 429–40.

[133] J. J. Wilkens and U. Oelfke, *Analytical linear energy transfer calculations for proton therapy*, Medical Physics, 30 (2003), pp. 806–15.

[134] S. C. Wilks, A. B. Langdon, T. E. Cowan, M. Roth, M. Singh, S. Hatchett, M. H. Key, D. Pennington, A. MacKinnon, and R. A. Snavely, *Energetic proton generation in ultra-intense laser–solid interactions*, Physics of Plasmas, 8 (2001), pp. 542–49.

[135] P. Wilson, B. Jones, T. Yokoi, M. Hill, and B. Vojnovic, *Revisiting the ultra-high dose rate effect: implications for charged particle radiotherapy using protons and light ions*, British Journal of Radiology, 85 (2012), pp. e933–39.

[136] R. R. Wilson, *Radiological use of fast protons*, Radiology, 47 (1946), pp. 487–91.

[137] V. P. Yanovsky, M. D. Perry, C. G. Brown, M. D. Feit, and A. Rubenchik, *Plasma Mirrors for Short Pulse Lasers*. http://www.osti.gov/bridge/, 1997.

[138] A. Yogo, T. Maeda, T. Hori, H. Sakaki, K. Ogura, M. Nishiuchi, A. Sagisaka, H. Kiriyama, H. Okada, S. Kanazawa, T. Shimomura, Y. Nakai, M. Tanoue, F. Sasao,

P. R. Bolton, M. Murakami, T. Nomura, S. Kawanishi, and K. Kondo, *Measurement of relative biological effectiveness of protons in human cancer cells using a laser-driven quasimonoenergetic proton beamline*, Applied Physics Letters, 98, 053701 (2011).

[139] A. Yogo, K. Sato, M. Nishikino, M. Mori, T. Teshima, H. Numasaki, M. Murakami, Y. Demizu, S. Akagi, S. Nagayama, K. Ogura, A. Sagisaka, S. Orimo, M. Nishiuchi, A. S. Pirozhkov, M. Ikegami, M. Tampo, H. Sakaki, M. Suzuki, I. Daito, Y. Oishi, H. Sugiyama, H. Kiriyama, H. Okada, S. Kanazawa, S. Kondo, T. Shimomura, Y. Nakai, M. Tanoue, H. Sasao, D. Wakai, P. R. Bolton, and H. Daido, *Application of laser-accelerated protons to the demonstration of DNA double-strand breaks in human cancer cells*, Applied Physics Letters, 94, 181502 (2009).

[140] R. Yuste, *Fluorescence microscopy today*, Nature Methods, 2 (2005), pp. 902–4.

[141] K. Zeil, M. Baumann, E. Beyreuther, T. Burris-Mog, T. Cowan, W. Enghardt, L. Karsch, S. Kraft, L. Laschinsky, J. Metzkes, D. Naumburger, M. Oppelt, C. Richter, R. Sauerbrey, M. Schürer, U. Schramm, and J. Pawelke, *Dose-controlled irradiation of cancer cells with laser-accelerated proton pulses*, Applied Physics B, 110 (2013), pp. 437–44.

[142] K. Zeil, S. D. Kraft, S. Bock, M. Bussmann, T. E. Cowan, T. Kluge, J. Metzkes, T. Richter, R. Sauerbrey, and U. Schramm, *The scaling of proton energies in ultrashort pulse laser plasma acceleration*, New Journal of Physics, 12, 045015 (2010).

[143] L. Zhao and I. J. Das, *Gafchromic EBT film dosimetry in proton beams*, Physics in Medicine and Biology, 55 (2010), pp. N291–301.

[144] J. F. Ziegler, J. P. Biersack, and M. D. Ziegler, *SRIM, the stopping and range of ions in matter*, 2008. http://www.srim.org/.

[145] O. Zlobinskaya. personal communication, July 2012. used at Helmholtz Zentrum München.

[146] O. Zlobinskaya, G. Dollinger, D. Michalski, V. Hable, C. Greubel, G. Du, G. Multhoff, B. Röper, M. Molls, and T. E. Schmid, *Induction and repair of DNA double-strand breaks assessed by gamma-H2AX foci after irradiation with pulsed or continuous proton beams*, Radiation and Environmental Biophysics, 51 (2012), pp. 23–32.

[147] O. Zlobinskaya, C. Siebenwirth, C. Greubel, V. Hable, R. Hertenberger, N. Humble, S. Reinhardt, D. Michalski, B. Röper, G. Multhoff, G. Dollinger, J. Wilkens, and T. Schmid, *The effects of ultra-high dose rate proton irradiation on growth delay in the treatment of human tumor xenografts in nude mice*, Radiation Research, (under revision).

PUBLICATIONS

PAPERS IN JOURNALS

first author

- *Biological comparison between laser-driven protons and tandem accelerator protons* (in preparation)

coauthor

- O. Zlobinskaya, C. Siebenwirth, C. Greubel, V. Hable, R. Hertenberger, N. Humble, S. Reinhardt, D. Michalski, B. Röper, G. Multhoff, G. Dollinger, J. J. Wilkens, T. E. Schmid: *The effects of ultra-high dose rate proton irradiation on growth delay in the treatment of human tumor xenografts in nude mice*, Radiation Research, (under review)
- S. Reinhardt, C. Greubel, N. Humble, K. Parodi, J. J. Wilkens and W. Assmann: *EBT2 and EBT3 film calibration for dosimetry of laser-accelerated protons in the 4 - 20 MeV energy range* Radiation and Environmental Biophysics, (submitted)
- D. Bartkowiak, N. Humble, P. Suhr, J. Hagg, K. Mair, B. Polivka, U. Schneider, D. Bottke and T. Wiegel: *Second cancer after radiotherapy, 1981-2007*, Radiotherapy Oncology 105(1):122-126 (2012)
- J. Bin, K. Allinger, W. Assmann, G. Dollinger, G. A. Drexler, A. A. Friedl, D. Habs, P. Hilz, R. Hoerlein, N. Humble, S. Karsch, K. Khrennikov, D. Kiefer, F. Krausz, W. Ma, D. Michalski, M. Molls, S. Raith, S. Reinhardt, B. Röper, T. E. Schmid, T. Tajima, J. Wenz, O. Zlobinskaya, J. Schreiber and J.J Wilkens: *A laser-driven nanosecond proton source for radiobiological studies*, Applied Physics Letters 101, 243701 (2012)
- R. Orecchia, B. A. Jereczek-Fossa, E. Rondi, I. Bossi Zanetti, I. Meaglia, R. Luraschi, M. C. Leonardi , N. Rotmensz, E. Botteri, C. Fodor, A. Cecconi, A. Morra, R. Lazzari, A Ferrari, F. Cattani, V. Galimberti, A. Luini, P. Veronesi, S. Zurrida, W. Doerr, N. Humble, K. R. Trott, A. Ottolenghi, V. Smyth and U. Veronesi: *Second malignancies following breast cancer treatment: a case-control study based on the Peridose methodology. ALLEGRO project (task 5.4)*, Tumori, 98:715-721 (2012)

PAPERS IN BOOKS AND CONFERENCE ABSTRACTS

first author

- N. Humble, K. Allinger, W. Assmann, J. Bin, G. Dollinger, G. Drexler, A. Friedl, P. Hilz, D. Kiefer, W. Ma, D. Michalski, M. Molls, S. Reinhardt, T. Schmid, O. Zlobinskaya, J. Schreiber and J. J. Wilkens: *Single shot cell irradiations with laser-driven protons*, AIP Conference Proceedings, 1546:84-86 (2013)

- N. Humble, K. Allinger, J. Bin, G. A. Drexler, A. A. Friedl, P. Hilz, D. Kiefer, W. Ma, S. Reinhardt, T. E. Schmid, O. Zlobinskaya, J. Schreiber and J. J. Wilkens: *Single shot cell irradiations with laser-driven protons* Abstracts of Deutsche Gesellschaft für DNA-Reparaturforschung, Sep 17-20 (2012)

- N. Humble, K. Allinger, W. Assmann, J. Bin, G. Dollinger, G. Drexler, A. A. Friedl, P. Hilz, D. Kiefer, W. Ma, D. Michalski, M. Molls, S. Reinhardt, T. E. Schmid, O. Zlobinskaya, J. Schreiber and J. J. Wilkens: *Single shot cell irradiations with laser-driven protons*, Radiotherapy and Oncology, 105(3)S31 (2012)

- N. Humble, K. Allinger, J. Bin, P. Hilz, D. Kiefer, W. Ma, S. Reinhardt, T. E. Schmid, O. Zlobinskaya, J. Schreiber and J. J. Wilkens: *Single shot cell irradiations with laser-driven protons* Abstracts of the 51st Meeting of the Particle Therapy Co-Operative Group, May 13-19 (2012)

- N. Humble, K. Allinger, J. Bin, P. Hilz, D. Kiefer, W. Ma, S. Reinhardt, T. E. Schmid, O. Zlobinskaya, J. Schreiber and J. J. Wilkens: *Optimizing the experimental components required in a laser-accelerated particle cell irradiation*, Abstracts of the 14th International Congress of Radiation Research, Aug 28 - Sept 1 (2011)

- N. Humble, K. Allinger, J. Bin, P. Hilz, D. Kiefer, W. Ma, S. Reinhardt, T. E. Schmid, O. Zlobinskaya, J. Schreiber, J. J. Wilkens: Abstracts of Deutsche Gesellschaft Medizinische Physik, Sept 28 - Oct 1 (2011)

- N. Humble and L. Holloway: *The role of positron emission tomography in radiation therapy treatment planning*, Australasian Physical & Engineering Sciences in Medicine, 31(1):61 (2007)

coauthor

- J. Bin, W. Ma, K. Allinger, D. Kiefer, P. Hilz, S. Reinhardt, W. Assman, D. Habs J. Schreiber, G. A. Drexler, A. A. Friedl, N. Humble, D. Michalski, M. Molls, T. E. Schmid, O. Zlobinskaya and J. J. Wilkens: *Laser driven ion source from ultrathin foils and its biomedical application*, 2012 IEEE 39th International Conference on Plasma Sciences 5C-6 (2012)

- G. A. Drexler, S. Auer, O. Zloblinskaya, T. E. Schmid, D. Michalski, V. Hable, N. Humble, W. Assmann , S. Reinhardt, C. Greubel, J. Bin, K. Allinger, W. Ma, J. Schreiber, G. Dollinger, J. J. Wilkens and A. A. Friedl: *No increased RBE of ultra-short pulsed Proton irradiation and first Cell irradiations with laser-accelerated Protons in Munich*, Stahlentherapie und Onkologie, 188(S1):138 (2012)

- T. E. Schmid, K. Allinger, J. Bin, G. Dollinger, G. A. Drexler, N. Humble, S. Reinhardt, O. Zlobinskaya, J. Schreiber and J. J. Wilkens: *Relative Biological Effectiveness of Single-Shot Irradiation With Laser-Driven Nanosecond Proton Bunches*, International Journal of Radiation Oncology, Biology, Physics, 8 S684-85 (2012)

- T. E. Schmid, K. Allinger, W. Assman, J. Bin, G. A. Drexler, A. A. Friedl, P. Hilz, N. Humble, D. Kiefer, W. Ma, D. Michalski, M. Molls, S. Reinhardt, B. Röper, O. Zlobinskaya, J. Schreiber and J. J. Wilkens: *DNA double strand breaks assessed by gamma-H2AX foci after irradiation with single-shot laser-driven nanosecond protons*, Strahlentherapie und Onkologie, 188(S1):137-138 (2012)

- D. Bartkowiak, N. Humble, U. Schneider and T. Wiegel: *Second Tumors after Radiation Therapy - Data from a single Institution*, Stahlentherapie und Onkologie, 187(S1):12 (2011)
- D. Bartkowiak, N. Humble, K. Mair, B. Polivka, U. Schneider, D.Bottke and T. Wiegel: *Second cancer after radiotherapy - a single institution study 1981-2007*, Radiotherapy and Oncology (96)S1:126 (2010)

Appreciation is a wonderful thing.
It makes what is excellent in others belong to us as well.

— Voltaire

ACKNOWLEDGMENTS

I am very much indebted to my supervisor Prof. Dr. Jan J. Wilkens for giving me the opportunity and supportive environment to learn so much. I consider myself very lucky to have been able to discuss many ideas with you; thank you so much for always managing to find time for me and for your endless patience! I am also grateful to Prof. Dr. Franz Pfeiffer for taking on the hefty task of reading my thesis as well as for being my second examiner.

FROM THE KLINIK FÜR STRAHLENTHERAPIE I thank Prof. Dr. Michael Molls for allowing me to be a part of the clinic environment, which complemented the pre-clinical research I conducted.

FROM THE BIOLOGISTS I would like to thank Prof. Dr. Anna Friedl, Dr. Thomas E. Schmid, Dr. Olga Zlobinskaya, and Dr. Guido Drexler for showing and discussing with me many interesting biological phenomena. I am especially indebted to Olga for taking pains with me to get to know the joys and frustrations of fluorescent microscopy and foci analysis.

FROM THE PHYSICISTS I am grateful to have collaborated with Prof. Dr. Jörg Schreiber and his working group Jianhui Bin, Klaus Allinger, Dr. Wenjun Ma and Peter Hilz. Thank you for letting me occasionally hang around your lab at strange hours and taking time to explain in relatively simple ways your work that directly contributed something towards mine. Especially Jianhui for providing me with the spectral information. Thank you very much to Prof. Dr. Günther Dollinger for the constructive comments concerning my work as well as Dr. Volker Hable, Christoph Greubel, Christian Siebenwirth and Dr. Sabine Reinhardt for being so helpful during and in-between beam time; especially Christoph for being the deconvolution king.

FROM THE IMPRS I would firstly like to thank Prof. Dr. Peter Hommelhof, Dr. Vlad Yakovlev and Dr. Nick Karpowicz for coordinating such an interesting array of events during my time in IMPRS. And secondly I would like to express my sincere gratitude to Mrs Wild for showing me the true meaning of organisation skills - I am lucky to have learned from one of the best! I would also like to acknowledge the financial support provided to me by the IMPRS-APS.

Finally I thank the dynamic working group at Klinikum rechts der Isar for providing a friendly atmosphere. Birgit Mueller, Kerstin Hofmann, Florian Kamp, Sarah Brueningk, Frauke Alexander, Sebastian Faby and Dr. Tanja Wenzl; thank you so much for the laughs and abundance of cake. Here I would like to particularly thank Birgit, Michal Devecka and Cara Nash for carefully proof reading my thesis as well as Sarah for the individual cell dosimetry. I would also like to thank my parents who have supported me getting to this point; the yearly visits meant a lot to me during my time here. Lastly, I am most fortunate to have Stefan (Scheldon) Schell in my life; thank you for the discussions/'disagreements', comments/criticisms and being the optimiser of my life.